The Optical Properties of Bismuth Nanowires

by

Marcie R. Black

B. S., MIT (1994)
M. S., MIT (1995)

Submitted to the Department of Electrical Engineering
and Computer Science
in partial fulfillment of the requirements for the degree of

Doctor of Philosophy

at the

MASSACHUSETTS INSTITUTE OF TECHNOLOGY

May 2003

Author .....
Department of Electrical Engineering and Computer Science
May 2, 2003

Certified by .....
Mildred S. Dresselhaus
Institute Professor
Thesis Supervisor

Accepted by .....
Arthur C. Smith
Chairman, Departmental Committee on Graduate Students

The Optical Properties of Bismuth Nanowires

by

Marcie R. Black

Submitted to the Department of Electrical Engineering and Computer Science
on May 2, 2003, in partial fulfillment of the
requirements for the degree of
Doctor of Philosophy

Abstract

The optical absorption of bismuth nanowires in the energy (wavenumber) range of $600 - 4000cm^{-1}$ is studied. Optical reflection and transmission spectra reveal that bismuth nanowires have a large and intense absorption peak as well as several smaller absorption peaks which are not measured in bulk bismuth. The smaller absorption peaks fit reasonably well to theoretical models for intersubband absorption in bismuth nanowires. The wire diameter, polarization, and doping dependencies as well as the spectral shape of the dominant peak agree with simulations of the optical absorption resulting from an L-point valence to T-point valence band electronic transition. The large absorption peak is present even for nanowires too large to exhibit quantum confinement, thus showing that the absorption results from a surface-induced effect and not from quantum confinement. The enhanced optical absorption in nanowires over bulk bismuth is attributed to a surface term in the matrix element which results from the spacial gradient of the dielectric function and the large dielectric mismatch between bismuth and the surrounding alumina or air. A comparison of the measured spectra with simulations of optical absorption resulting from direct L-point electronic transitions demonstrated that this absorption mechanism is not dominant in our materials.

In order to explore the optical properties of bismuth nanowires, two methods were developed. First, effective medium theory applied in reverse was used to deduce the dielectric function of materials smaller than the wavelength of light. Second, a technique to fabricate nanowires with diameters above $200nm$ was transfered into our laboratory.

The enhanced coupling between the L-T point valence bands in nanowires may lead to a very accurate measurement of the band gap and band overlap in bismuth as a function of doping and temperature. In addition, the discovery of the enhanced interband coupling resulting from the surface contribution to the matrix element has many implications, especially if this result is applicable to other systems.

Thesis Supervisor: Mildred S. Dresselhaus
Title: Institute Professor

Acknowledgments

Professionally MIT has been a very good place for me. I am very fortunate to have Millie Dresselhaus as my adviser. Millie gave me the freedom to explore my own research ideas, while at the same time she was always available when I needed help. I'll never forget her special 8am (ug) sessions just to catch me up on the physics that I needed for my research. The combination of academic freedom and support is really the ideal situation for someone like me who comes to graduate school to develop her skills at independent research. Millie's gentle directing, combine well with Gene's more direct approach and Laura's caring attitude to make Millie's group a very efficient learning and growing environment.

I couldn't have asked for a better thesis committee. Peter Hagelstein and Qing Hu have both been extremely supportive of my research. Both are extremely bright and also very willing to help, thus making them perfect advisers. In addition to the technical advice they have given me, I really appreciate their career advise as well.

I have always been fortunate to have mentors in my life. Those who have helped guide me down a path that is best for me include James Chung, Anu Agarwal, Faris Modowar, Yoel Fink, and Valdimir Bulovich.

Naturally, Millie attracts very interesting, smart, and nice people to her research group and her circle of collaborators. I have had the pleasure of working with many wonderful people during my five and a half years in her research group. Marcos helped teach me about carbon nanotubes. I had the pleasure of learning from Wei-Ming while we were office-mates. Peter Eckland came up with the idea of using effective medium theory. Zhibo Zhang developed the liquid pressure technique to fill the alumina templates. (He has almost as much energy as Millie.) Tim McClure help me with the FTIR especially with the cold stage and in implementing all my crazy ideas. Karlene Rosera Maskala co-developed the high voltage anodization process and also has been great to bounce off ideas about alumina fabrication. Steve Cronin came up with the idea of measuring free-standing wires. (He is much more talented than he gives himself credit for.) Kornelious Nielsh anodized the 20V alumina sample for us

and has been great to discuss the anodization process with. Yuming Lin filled most of the alumina templates in this thesis with bismuth, wrote the program to solve for the energies of the subbands, and he continued to keep our computers running; Oded Rabin filled the 20V sample electrochemically. Oded, Yuming, and Steve all have been great to bounce ideas off; I had the pleasure to supervise extremely talented Megha Padi. Megha took some of the doping data and helped develop some of the earlier code. She also is the only one who knows all the little details of my (earlier) work and has checked some of the calculations for me. I also enjoyed the company of many in the group with whom I didn't work closely with. These include: Joe Habib, Ibo Matta, Ado Jorio, X. Sun, Alesandra Marucci, Antonio Souza Filho, Paula Corio, Victor Brarr. In addition, I want to acknowledge Sandra Brown for all the useful advice she continues to give me on surviving graduate school - most of which worked, Adelina who is both wise and smart, and Grace who helped keep me calm my last year at MIT.

The time I spent working towards my PhD was by far the most difficult period of my life. I have been so fortunate to have so many close friends that carried me when I couldn't walk, and forced me to stand on my own when I could. Those in Boston and those that have stayed in regular contact with me were especially helpful through this time: Tracy, Aarti, Liz, Sita, Missy, Ann, and Karrie. In addition, Millie has been extremely patient with me through hard times. Even after only the first month of joining her group she proved that she is the most supportive adviser I know of. I am also thankful to my parents with whom I have grown much closer to in the last five years.

My deepest thanks goes to my wonderful husband, Kevin, who among other important lessons has taught me that sometimes when you can't solve a problem, playing a couple games of Smash can give you some insight into it. In addition, he spent countless hours listen to me babble about bismuth nanowires, asking very insightful questions, and proof-reading my boring technical papers. Thank you Kevin. I love you very much.

In memory of Steven Nathan Black

who encouraged me to pursue my PhD

10/10/1969 - 3/15/1999

Contents

1 INTRODUCTION **28**

2 BACKGROUND **30**

2.1 BISMUTH BACKGROUND 30

2.1.1 BISMUTH BAND PARAMETERS 30

2.1.2 QUANTUM CONFINEMENT IN BISMUTH NANOWIRES . 39

2.2 OPTICS BACKGROUND 41

2.2.1 OPTICAL CONSTANTS 41

2.2.2 EFFECTIVE MEDIUM THEORY 41

2.3 APPLICATIONS OF NANOWIRES 43

2.3.1 MAGNETIC APPLICATIONS 44

2.3.2 THERMOELECTRIC APPLICATIONS 44

2.3.3 OPTICAL APPLICATIONS 48

3 SAMPLE FABRICATION **52**

3.1 Al_2O_3 TEMPLATE PREPARATION 52

3.2 ULTRA COOL METHOD OF ANODIZATION TO FORM LARGE PORE ALUMINA 59

3.3 FILLING 63

3.4 MAKING FREE-STANDING WIRES 66

3.5 CHARACTERIZING THE BISMUTH NANOWIRES 68

3.5.1 XRD 68

3.5.2 TEM 69

4 FINDING THE DIELECTRIC FUNCTION OF BISMUTH NANOWIRES 71

4.1 FTIR SETUP 71

4.2 NANOWIRES INSIDE ANODIC ALUMINA 75

4.2.1 REFLECTION AND TRANSMISSION MEASUREMENTS . 75

4.2.2 FINDING ϵ_1 AND ϵ_2 FROM R AND T 75

4.2.3 REVERSE EFFECTIVE MEDIUM THEORY (REMT) . . . 79

4.3 FREE STANDING WIRES 80

5 IDENTIFYING THE ABSORPTION MECHANISMS 86

5.1 OVERVIEW 86

5.2 EXPERIMENTAL MEASUREMENTS 92

5.2.1 POLARIZATION 92

5.2.2 WIRE DIAMETER 94

5.2.3 TELLURIUM DOPING 99

5.2.4 SLOPE OF THE ABSORPTION SPECTRA OF FREE-STANDING WIRES 103

5.2.5 LOW T MEASUREMENTS 105

5.3 SIMULATIONS OF OPTICAL ABSORPTION RESULTING FROM ELECTRONIC TRANSITIONS IN BISMUTH NANOWIRES 109

5.3.1 INTRABAND TRANSITIONS - FREE CARRIER ABSORPTION 109

5.3.2 INTERSUBBAND 112

5.3.3 INTERBAND THEORY 127

5.3.4 INDIRECT INTERBAND L-T TRANSITION 129

5.4 CONCLUSIONS FOR IDENTIFYING THE ABSORPTION MECHANISMS 155

6 CONCLUSION AND FUTURE WORK 158

6.1 CONCLUSION 158

6.2 FUTURE WORK 159

6.2.1 SECONDARY ION MASS SPECTROMETRY (SIMS) 160

6.2.2 FURTHER DOPING STUDIES 161
6.2.3 BISMUTH-ANTIMONY NANOWIRES 162
6.2.4 PHOTOLUMINESCENCE 163
6.2.5 ONE-DIMENSIONAL DIODE 164

A EMT LITERATURE REVIEW **165**

List of Figures

2-1 (a) Brillouin zone of bismuth. Three electron pockets are at the L-points, labeled "A" and "B", and one hole pocket is at the T-point. (b) The dispersion relations of the L-point and T-point bands shown schematically. At room temperature, the L-point bandgap is 36 meV [1], the L-point electron Fermi energy is 56 meV [2] and the T-point hole Fermi energy is 42 meV [2]. 31

2-2 The effective mass of the L-point carriers in the $< 012 >$ direction expressed in free electron mass units as a function of energy in eV. Of the three carrier pockets at the L-point, two are degenerate and their effective mass values are labeled "m_{eb}" in the figure. The effective mass of the third pocket is labeled "m_{ea}" and is non-degenerate. The effective mass of the T-point hole pocket in the $< 012 >$ direction, labeled m_b, which follows a parabolic dispersion relation is shown for comparison. 35

2-3 The L-point and T-point electronic subband structure in bismuth in the presences of quantum confinement. E_g is the L-point bandgap, and Δ_0 is the band overlap. 39

2-4 The phase diagram of the semimetal to semiconductor transition in bismuth nanowires is shown as a function of temperature and wire diameter. Depending on the wire diameter, a nanowire is either a semimetal (III), a semiconductor(I), or it switches from a semimetal to semiconductor as the temperature is decreased(II) from 300K to 0K. 40

2-5 The increase in the dimensionless figure of merit within the quantum-confined systems of bismuth as a function of wire diameter or quantum well thickness. The thermoelectric properties are expected to improve greatly when the wires are small enough to become one dimensional. (Figure compliments of Yu Ming Lin.) 45

2-6 The effect of temperature on the Fermi energy and the Fermi distribution in the presence of a singularity in the density of states. A. At high temperature the Fermi energy must move away from the singularity to prevent having too high a carrier concentration. B. At low temperatures, the Fermi energy must move closer to the singularity to ensure a sufficiently high carrier density. 47

3-1 The electro-chemical and anodization setup. In the case of high voltage anodizations used to fabricate large pore alumina templates, the ice bath is filled above the acid level, and the stirring of the electrolyte is aggressive. 54

3-2 The pores in alumina during anodization. (a) The pore diameter is larger and the barrier layer thinner than for the preferred pore diameter. The thinner barrier layer favors electric field enhanced diffusion over etching, thus increasing the barrier layer and decreasing the wire diameter. (b) The pore diameter is such that the etch rate and anodization rate are equal. (c) The pore diameter is smaller and the barrier layer larger than for the preferred pore diameter. Thus, etching is favored over electric field enhanced diffusion and the barrier layer is decreased and the pore widened [3]. 56

3-3 Top view SEM pictures of anodic alumina anodized at 45V in 4wt%$H_2C_2O_4$ after the first (a) and second (b) anodizations. (Figures are compliments of YuMing Lin.) 58

3-4 A Fourier transform of an SEM image of a very well-ordered alumina template. (Figure is compliments of Karlene Maskaly.) 59

3-5 A cross section of a porous alumina template on top of Si. The pores go completely through the alumina. (Figure is compliments of Oded Rabin.) 60
3-6 Scanning electron microscope images of two samples. The sample shown in (a) was anodized near the optimal voltage for a 4% oxalic acid electrolyte, while sample (b) was anodized above this voltage. Hence, sample (a) has a narrow distribution of wire diameters around 35 nm, while sample (b) has a wide distribution of wire diameters around ~70 nm. 61
3-7 The anodization setup for high voltage anodization. The automatic cooling system, the high cooling liquid level, and the insulated conductor, all prevent breakdown during the anodization process. 62
3-8 Scanning electron micrograph of anodic alumina template anodized at 160 V with pore diameters around 200 nm. 62
3-9 Schematic diagram of the pressure-injection method used in this research to fill the pores in the anodic alumina template with bismuth. The figure is from Dr. Zhibo Zhang. 64
3-10 Scanning electron microscope picture of an unfilled (a) and filled (b) alumina template. The dark holes in the filled template (b) are pores that remain unfilled after pressure injection. The SEM image of the unfilled alumina (a) is taken of the top side of the alumina (furthest from the aluminum film), while the filled alumina (b) is taken from the bottom side of the alumina (nearest to the aluminum film). 66
3-11 XRD patterns of bismuth filled alumina with average wire diameters of (a) 40 nm, (b) 52 nm, and (c) 95 nm. Marked above the individual peaks are Miller indices corresponding to the lattice planes of bulk Bi. The XRD peaks positions are the same as those of the polycrystalline Bi standard. Figure from YuMing Lin. 68
3-12 High resolution TEM of a bismuth nanowire. Figure from Dr. Steve Cronin. 70

4-1 a) A Nicolet FTIR setup with a Nic-Plan microscope and a computer attached. b) CMSE shared facility's microscope FTIR. 72

4-2 A comparison of the reflection and transmission data taken from two different experimental systems. The data on the Nicolet instrument were taken at MIT's CMSE and was obtained using the microscope accessory. The data taken with the Bomem instrument were taken at Prof. Eklund's laboratory in the University of Kentucky. The spectra are similar but some differences are observed that may be accounted for by differences in temperature, humidity, and pressure. 73

4-3 Photon energy (wavenumber) dependence of the reflection and transmission of porous alumina and porous alumina filled with Bi nanowires: Both the transmission and reflection data show a large interference pattern in the range 2000 - 4000 cm^{-1} only for the unfilled sample. The absence of interference patterns in the Bi filled templates indicates an increase in absorption with the addition of Bi. Also indicating an increase in absorption, the transmission through the sample is decreased with the addition of Bi. The larger reflection in the filled samples is the result of an increase in the index of refraction with the addition of Bi. 74

4-4 A comparison of the dielectric function obtained from two methods: the first from frequency dependent reflection data using the Kramers-Kronig relations, and the other method which involves solving Maxwell's equations and then optimizing the fit between the frequency dependent reflection and transmission data. 78

4-5 Transmission data for: (a) free-standing Bi nanowires, (b) an unfilled alumina template, and (c) a Bi filled alumina template. 81

4-6 A schematic diagram of a free-standing bismuth nanowire array mounted on a glass slide. 81

4-7 The wavenumber (ν) dependence of the absorption coefficient found by taking the negative log of the transmission of free-standing bismuth nanowires (a), as well as the absorption of a thin piece of bismuth (points) and the fit to this absorption (line curve) (c). The insert compares the absorption of the free-standing wires (a), with the absorption [Im $(\epsilon_1 + i\epsilon_2)^{1/2}$] of bismuth nanowires inside an alumina template (b) as obtained by reverse EMT. The main absorption peaks of the two samples occur at about the same ν value. 82

4-8 A) The transmission as a function of wavenumber of free-standing bismuth nanowires. B) The derivative of the transmission ($dT/d\nu$) as a function of wavenumber. 84

4-9 Fit of Gaussian peaks to the absorption spectrum in the free-standing Bi nanowire sample. Five broad peaks are observed at 616, 667, 798, 986, and 1090 cm^{-1}. The absorption from the thin bismuth sample is used as the baseline and the absorption due to all 5 peaks is shown as the "total fit" to the data points. This spectrum is discussed further in section 5.3.2. 85

5-1 The L and T point bands and subbands in bismuth nanowires, and the possible types of band-to-band electronic transitions. 87

5-2 A sample mounted on the edge of a lid in preparation for polarization studies. The $\theta = 0$ mark is the direction in which the polarizer internal to the FTIR is set at 0. 92

5-3 Reflection [$R(\nu)$] of a Bi anodic alumina sample with several polarization angles θ: (a) 90°, (b) 117°, (c) 63°, (d) 27°, (e) -27°, (f) 0°. Curve f ($\theta = 0°$) shows features around 1000 cm^{-1}, while curve a ($\theta = 90°$) does not exhibit clear features in this spectral region. The insert shows a schematic of the sample and the definition of θ. 93

5-4 The deduced wavenumber dependent imaginary part of the dielectric function (ϵ_2) of alumina for light with the electric field parallel (o) and perpendicular (.) to the pore axis of the alumina template. 94

5-5 Reflection $[R(\nu)]$ of a polished piece of bulk bismuth and of free-standing Bi nanowires for comparison. The large feature near $\sim$ 1000 cm^{-1} in the reflection spectra of the free-standing wires is not present in the reflection spectra of bulk bismuth. The broad features in the bulk bismuth are likely a result of a non-perfect polish or of a misalignment with the sample stage. 95

5-6 The wavenumber dependence of the imaginary part of the index of refraction of 200 nm and absorption coefficient of $\sim$ 45 nm diameter bismuth nanowires fabricated inside an alumina template but with this template then removed. The absorption peak of the 200 and $\sim$ 45 nm wire diameter samples are at 965 and 1090 cm^{-1}, respectively. The imaginary part of the index of refraction of the 200 nm diameter wires was obtained by Kramers-Kronig relations and measurements of the optical reflectivity of the sample. The absorption of the $\sim$ 45 nm diameter wire was obtained from the negative log of the transmission of the sample. The absorption values are not corrected for surface roughness or sample thickness, and so the y-axis scales for the two graphs are different and arbitrary. 96

5-7 A) The dependence of the absorption coefficient on wavenumber, found by taking the negative log of the transmission of free-standing bismuth nanowires with diameters around 45 and 30 nm as well as the absorption on a thin piece of bismuth. An expanded view of the data for the 30 nm and 45 nm wires in the wavenumber range $600 < \nu < 1300$ cm^{-1} is shown in B). 97

5-8 The wire diameter dependence of the dielectric function ($\epsilon_1 + i\epsilon_2$) of bismuth nanowires vs. wavenumber obtained from analysis of reflectivity measurements for 35, 55, 70, and 65-80 nm diameter wires. The dielectric function of the bismuth nanowires are deduced by the method described in section 4.2. The deduced dielectric function from two different reflectivity measurements, taken from different locations, for both the 70 and 55 nm diameter samples are shown in the inserted figures for $\epsilon_1(\nu)$ and $\epsilon_2(\nu)$, in order to demonstrate the reproducibility of the results. The inserts show an expanded view of the real and imaginary parts of the dielectric function for the wavenumber range of $960 - 1090$ cm^{-1}. 98

5-9 (a) The measured optical reflection as a function of wavenumber for: (i) non-doped, (ii) lightly n-type doped, (iii) medium n-type doped, and (iv) heavily n-type doped arrays of bismuth nanowire 40nm in diameter inside an alumina template. The insert shows the deduced imaginary part of the index of refraction, K, for a (iii) doped and (i) undoped sample [4]. 100

5-10 The effect of tellurium doping on the imaginary part of the dielectric function $\epsilon_2(\nu)$ as a function of wavenumber of bismuth nanowires ($\sim 55nm$ in diameter) obtained from analysis of reflectivity measurements. 102

5-11 The normalized (a) and non-normalized absorption spectra for four free-standing nanowire samples. The absorption was found by taking the negative log of the transmission spectra. The spectra in (a) are normalized to the absorption peak intensity, with the exception of sample b, which was normalized to the extrapolated absorption peak intensity. Samples b, c, and d are were anodized at 45V, while sample a was anodized at 60V. Sample b is tellurium doped, while sample c is antimony doped. Samples a and d are undoped. 104

5-12 A schematic of the Linkum Hot/Cold stage. 105

5-13 A cross-sectional schematic of the Linkum Hot/Cold stage. The sample is placed on top of a KBr window, which is then placed on top of the sample holder. The sample holder allows the sample to be moved relative to the beam path. The sample holder is in contact with the metal stage which is cooled by liquid nitrogen. The temperature reading of the cold-stage is measured from a thermocouple in contact with the metal stage. ZnSe windows are placed above and below the sample to isolate the chilled sample space and to allow for optical measurements. 106

5-14 (a) Reflection of a bismuth-filled alumina template anodized at 20V at a temperature of 0°C, −75°C, −150°C, and −190°C. (b) Reflection of a same sample in (a), but with the alumina removed. The reflection is normalized to the reflection at 4000 cm^{-1}. The bismuth nanowires are on top of a gold film. The reflection measurements were taken at 20°C, −50°C, −100°C, −150°C, and −189°C. The insert shows an expanded plot of the normalized reflection for a wavenumber range of 800 − 1200 cm^{-1} 108

5-15 Calculated reflection spectra resulting from free carrier absorption where the plasmon frequency is 333 cm^{-1}, $\epsilon_{core} = 100$, and $\omega\tau >> 1$. 110

5-16 a) The calculated free carrier plasmon frequency as a function of wire diameter at room temperature for undoped, $8x10^{18}$ cm^{-3} doped, and $2x10^{19}$ cm^{-3} doped bismuth nanowires. b) The calculated free carrier plasmon frequency as a function of wire diameter at 77K for undoped bismuth nanowires. . . 111

5-17 The coupling strength, $F_{n.m}$ from the $m = 0$ state to the $n = 0$ to 49 states for carrier pocket A (see insert of Fig. 5-18). The wavefunctions of some states are shown ($n = 0$, 1, 2, 3, 13, 14, 30, and 32). States that are radially anti-symmetric have a larger coupling to the symmetric lowest energy $m = 0$ state. Also, the figure shows that even higher order states can have significant coupling to the $m = 0$ state. 116

5-18 The calculated optical absorption at 293 K resulting from inter-subband transitions for 41.5 nm Bi nanowires oriented along the ⟨012⟩ crystalline direction. The separate contributions from the two types of electron carrier pockets, A and B, as well as the total optical absorption are presented. The energies and relative intensities of the experimental absorption peaks are shown by the heavy dashed lines. In the insert, the Brillouin zone of bismuth is shown and the ⟨012⟩ crystalline direction is indicated by the arrow from the Γ point. 117

5-19 The measured absorption spectra of $\sim 45nm$ diameter wires and the fit of the spectra to a sum of Gaussian curves after background subtraction, the simulated absorption spectra resulting from intersubband absorption from $41.5nm$ diameter wires, and the energy derivative of the measured data from $\sim 45nm$ diameter wires. 120

5-20 The measured absorption spectrum of $\sim 30nm$ diameter wires and its fit to a sum of Gaussian components, after background subtraction, the simulated absorption spectra resulting from intersubband absorption from $21nm$ diameter wires, and the energy derivative of the measured transmission data from $\sim 30nm$ diameter wires. 121

5-21 Two subbands (labeled E_n and E_m) and the energy difference between them $(E_m - E_n)$ shown as a function of momentum along the wire axis. The corresponding joint density of states (JDOS) is shown in the insert. The non-parabolic effects cause the minimum energy difference between two subbands to be away from the subband edges. Thus, the joint density of states, as shown in the insert, has two singularities: the higher energy singularity resulting from transitions at the subband edge, and the lower energy singularity resulting from transitions at the location of the minimum energy difference between the subbands. 122

5-22 Simulated wavenumber dependence of the inter-subband absorption at 293 K for 45, 42.5, 40, and 35 nm diameter wires. As the wire diameter decreases, the number of absorption peaks increases and the absorption peak intensities decrease. 124

5-23 Simulated wavenumber dependence of the inter-subband absorption at 293 K for 45 diameter wires with Fermi energies, E_f, of $0.04eV$ and $0.08eV$ relative to the energy of the center of the L-point, the midpoint between the L-point valence and conduction bands. As the Fermi energy, E_f, increases, the absorption intensity increases, since the occupation of the initial subband states increases. 125

5-24 The calculated optical absorption at 293 K resulting from a direct interband transition for 41.5 and 45 nm Bi nanowires oriented along the $\langle 012 \rangle$ crystalline direction. The energies and relative intensities of the experimental absorption peaks are shown by the dashed lines. 128

5-25 The sum of the matrix elements, $M_e(n,m)$, for the first 100 initial states, n, to the first 100 final states, m. 135

5-26 The calculated $\epsilon_2(\nu)$ resulting from electronic transitions from pocket A at the L-point to the T-point, assuming a phonon absorption process. The matrix elements, $M_e(n,m)$ are scaled by Eq. 5.12 with s set to 1, 0.5, 0.25, and 0.1 for graphs a, b, c, and d respectively. The curves b, c, and d are offset with respect to the dotted lines and are multiplied by 75, 10, and 3, respectively. 137

5-27 The calculated $\epsilon_2(\nu)$ resulting from electronic transitions from pocket A at the L-point to the T-point, assuming a phonon absorption process. The matrix elements, $M_e(n,m)$ are scaled by Eq. 5.12 with s set to 1, 0.5, 0.25, 0.1, and 0. The curves are normalized to their absorption peak intensity. . 137

5-28 (a) The simulated optical absorption from transitions from the first 15 T-point subbands to their corresponding L-point subbands for one pocket of an undoped, $35\,nm$ diameter bismuth nanowire at $293K$. As the T-point subband index is increased, the absorption intensity decreases, since the higher subbands at the T-point have fewer empty states to which an electron from the L-point can be excited. The energy of the absorption peak increases rapidly with increasing subband number until about the 10^{th} state, at which point it levels off and eventually slowly decreases. (b) The energy difference between the band edges of the L and T point valence bands as a function of state number, the Fermi energy, and the energy of the T-point band edge as a function of state number. 139

5-29 The calculated absorption spectra from the non-degenerate hole pocket A and the doubly degenerate hole pocket B at the L-point, see Fig. 2-1, to the T point valence band of a 45 nm diameter $\langle 012 \rangle$ aligned bismuth nanowire at room temperature. The absorption is plotted in terms of the wavenumber dependence of the dielectric function $\epsilon_2(\nu)$, and the wavenumber on the x-axis is expressed in terms of the reciprocal wavelength. Each pocket has two absorption peaks, one when a phonon is emitted (at higher ν) and one when a phonon is absorbed (at lower ν). The total absorption (solid arrows) as well as the absorption assuming just phonon emission or just phonon absorption (dotted line arrows) are shown. 141

5-30 The simulated absorption spectra including all three pockets of the indirect L-T-point transition in 30 nm diameter bismuth nanowires at room temperature shown for three values of the band overlap energies for bulk bismuth, at 300K. Curves I, II, and III are for L-T band overlap energies of 172 (1387), 98 (790), and 24(194) $meV(\mathrm{cm}^{-1})$, respectively. The reported band overlap energy in bismuth at room temperature is $98meV$ (790 cm^{-1}) [2]. 142

5-31 (a) The measured optical transmission as a function of wavenumber of free-standing bismuth nanowires. (b) The simulated optical transmission as a function of wavenumber resulting from an indirect L-T transition in bismuth nanowires with a diameter of $45nm$. Note that the minimum transmission in the experimental spectra is at ~ 1100 cm^{-1}, and in the simulated spectra is at ~ 1500 cm^{-1}. The differences in the magnitude of the transmission likely result from the fact that only optical absorption from an indirect transition is simulated in (b), while in the experimental measurements, (a), many absorption and scattering mechanisms are likely to be present. . . . 144

5-32 (a) The simulated wavenumber dependence of $\epsilon_2(\nu)$ resulting from an indirect L-T transition in bismuth nanowires with a diameter of 70 and 35nm for the wavenumber range of $600 - 4000cm^{-1}$. The absorption peak in (a) moves from 1420 for the 70 nm wires to $1520cm^{-1}$ for the 35 nm wires. This shift of $\sim 100\,cm^{-1}$ is to be compared with the experimentally observed shift of $65cm^{-1}$. (b) The calculated energy difference between the first, second, third, and fourth subbands at the L-point valence band to the first, second, third, and fourth subbands at the T-point valence band. 146

5-33 (a) The measured wavenumber dependence of the reflection of (i) non-doped, (ii) lightly n-type doped, (iii) medium n-type doped, and (iv) heavily n-type doped bismuth nanowires. The insert shows the calculated wavenumber dependent absorption spectra of the (iii) medium and (i) undoped samples. (b) The simulated wavenumber dependence of $\epsilon_2(\nu)$ resulting from an indirect L-T transition in 40nm diameter bismuth nanowires with (i) no doping, (ii) low n-type doping, (iii) medium n-type doping, and (iv) heavy n-type doping. Arbitrary units are used. In experimental spectra, the reflection is decreased with the addition of n-type dopants, resulting from a decrease in the absorption coefficient. The simulated spectra also show a decrease in the $\epsilon_2(\nu)$ with increasing n-type dopant concentration. 148

5-34 A schematic of the energy bands in bismuth nanowires. The energy of a give L-point valence subband to T-point valence subband transition is equal to the bulk band overlap (E_{over}) of the T-point valence band with the L-point conduction band plus the band gap (E_g) of the L-point plus the confinement energy of the L-point (Econ L-pt) subband minus the confinement energy of the T-point subband (Econ T-pt). 150

List of Tables

2.1 Band Overlap Energy vs. Temperature 38

3.1 Anodization Conditions of Voltage, Temperature, and Electrolyte . . 54

5.1 Sample processing conditions 99

5.2 Processing conditions of Te-doped wires 102

5.3 Temperature of Sample vs. Metal Plate 107

Chapter 1

INTRODUCTION

Scientists and engineers now use the effects of low dimensions as another means of tailoring a material to a desired application [5–8]. In the last decade, engineers have made great advances in the fabrication of nanoscale devices. Some of these techniques have enabled the fabrication of devices so small that quantum mechanics dominates the material's free electron properties. Quantum dots (0 dimensions), wires (1 dimensions), and wells (2 dimensions) are being investigated for use in optical, electronic, and magnetic applications. However, in order for the design of a material to be optimized, the key parameters of the low dimensionality need to be measured and compared to theoretical calculations, and those results need to be used to improve these models. Once the effects of low dimensions on a particular system are well understood, the size of the quantum confined dimension(s) can be selected to achieve the desired degree of quantum and surface effects for a specific application.

Bismuth nanowires provide a promising material for use as a modeling system for studying the optical properties of both one-dimensional systems and materials where the material's dimensions are much less than the wavelength of light. Since our wires are crystallographically ordered, aligned, small enough to exhibit carrier quantum confinement, and the wire diameter can be controlled, they make an excellent system for studying quantum effects. This work experimentally measures the effects of quantum confinement and surface effects in bismuth nanowires and compares this result to theoretical models based on previously reported values of the band parameters

[1, 2, 9]. Bismuth nanowire arrays are a new development, so they likely have many unforeseen applications. This thesis seeks to improve the understanding of bismuth nanowires and to possibly help open the way for some of these new applications.

Chapter 2 reviews some of the background relevant for this thesis. This chapter includes the bismuth band properties used in the modeling section and the effects of quantum confinement on the band structure within this model. Chapter 2 also includes some of the optics background required to understand the interpretation of the optical measurements and an explanation of potential applications for nanowires.

Chapter 3 reviews our method for the fabrication of bismuth nanowires. Although the sample fabrication is not the central part of this thesis, it is a necessary part. All of the fabrication, except the high voltage anodization, is reproduced from the work of Z. Zhang and others [10, 11].

Chapter 4 explains how the dielectric function of bismuth nanowires is obtained, including a description of the optical setup. This chapter describes several different methods to deduce the dielectric function of bismuth nanowires from optical data including a method that applies Kramers–Kronig analysis and a method that applies Maxwell's equations. The situations in which each method can be used are also discussed.

Chapter 5 applies the methods to obtain the dielectric function of bismuth nanowires outlined in chapter 4 and compares these results to theoretical calculations in order to identify the absorption mechanisms in the measured energy range.

Lastly, Chapter 6 summarizes the findings of this research and presents suggestions for future research.

Chapter 2

BACKGROUND

This chapter reviews some of the fundamental background needed for subsequent chapters. Section 2.1 describes the bulk bismuth band parameters and how they are modified in bismuth nanowires. Section 2.2 summarizes the optics background required for this thesis. Lastly, section 2.3 presents some of the applications for nanowires concentrating on thermoelectric and optical applications.

2.1 BISMUTH BACKGROUND

2.1.1 BISMUTH BAND PARAMETERS

For a given sample size, quantum confinement effects increase as the carriers' effective mass decreases. Since bismuth has very small electron and hole effective mass tensor components (particularly at the L-point in the Brillouin zone where the mass components $\mathbf{m}^*$ vary from $0.001\,m_0$ to $0.26\,m_0$, depending on the crystalline direction[12]), the energy separation between subbands is significant even at sample dimensions as large as $\sim$40 nm. Bismuth also has a large mean free path, $\sim$ 250 nm at 300 K[13], which, in addition to the small effective mass, is required for the observation of quantum confinement effects. As a result of the small effective mass and the large carrier mean free path, bismuth nanowires exhibit significant quantum confinement at manufacturable dimensions. Furthermore, bismuth has a low melting

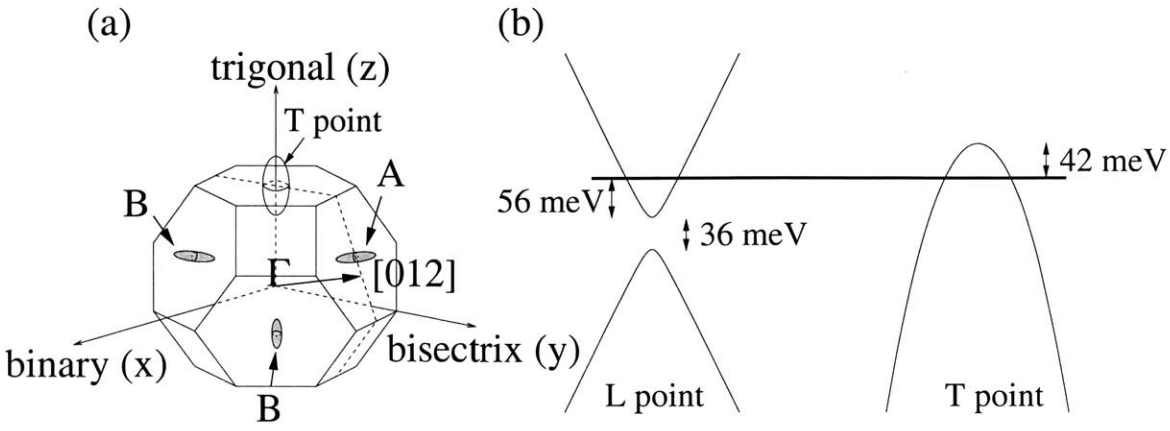

Figure 2-1: (a) Brillouin zone of bismuth. Three electron pockets are at the L-points, labeled "A" and "B", and one hole pocket is at the T-point. (b) The dispersion relations of the L-point and T-point bands shown schematically. At room temperature, the L-point bandgap is 36 meV [1], the L-point electron Fermi energy is 56 meV [2] and the T-point hole Fermi energy is 42 meV [2].

point (~271°C), which enables the fabrication of nanowires using a liquid pressure injection technique. Bismuth nanowires are grown with large crystalline regions, thus keeping grain boundary scattering to a minimum. Lastly, bismuth nanowires are especially interesting because they exhibit a transition from a semimetal with a small band overlap (38 meV at 0 K for large bulk-like wires) to a narrow gap semiconductor as the wire diameter decreases and the characteristic quantum confinement energy increases [14], as discussed further in section 2.1.2. This semimetal to semiconductor transition occurs in Bi nanowires at relatively large wire diameters because of its small band overlap and small effective mass components. The transition from a semimetal to a semiconductor as well as quantum effects in general have significant effects on the electronic, thermoelectric, and optical properties of bismuth, particularly at low temperatures.

This thesis discusses the properties of bulk (not quantum-confined) bismuth before discussing bismuth nanowires, since the crystal structure of bismuth nanowires is essentially the same as for bulk bismuth. In bulk bismuth, carrier pockets are located at both the L- and the T-points of the Brillouin zone used to describe the rhombohedral structure of crystalline bismuth, see Fig. 2-1. Near the Fermi level, the

three equivalent L-points have both conduction and valence bands, which are mirror images of each other and are separated by a small energy gap of 36 meV [1] at room temperature. The dispersion relation of the T-point valence band is parabolic with effective mass tensor components ranging from $0.059\,m_0$ to $0.634\,m_0$ at 1.7K [12]. I was unable to locate studies on the T-point hole mass tensor for temperatures above 77K.

The L-point bands are highly non-parabolic and are approximated by the Lax 2-band model [15, 16], which applies $\vec{k}\cdot\vec{p}$ perturbation theory to two strongly coupled bands. This approximation is valid when, like at the L-point in bismuth, two bands are strongly coupled to each other and other bands are weakly coupled to that pair. Under this assumption,

$$[H_0 + H']u_{n,k}(r) = E(k)u_{n,k}(r) \tag{2.1}$$

where $u_{n,k}(r)$ is the envelope function, n is the bulk band index, and $\vec{k}$, H_0, and H' are defined as follows:

$$H_0 = \frac{\vec{p}^2}{2m_0} + V(r) + \frac{\hbar\vec{k_0}\cdot\vec{p}}{m_0} \tag{2.2}$$

$$H' = \frac{\hbar\vec{k}\cdot\vec{p}}{m_0} \tag{2.3}$$

$$\vec{k} = \vec{K_{tot}} - \vec{k_0} \tag{2.4}$$

where $\vec{k_0}$ is the momentum at the band edge, and H_0 is the L-point Hamiltonian before the perturbation, while H' is the perturbation arising from the coupling between the two bands.

The Hamiltonian in equation 2.1 can thus be solved by the secular equation

$$\begin{array}{c} \\ c \\ v \end{array} \begin{vmatrix} \begin{array}{c} c \\ \langle i|\mathcal{H}_0+\mathcal{H}'|i\rangle - E \\ \langle j|\mathcal{H}_0+\mathcal{H}'|i\rangle \end{array} & \begin{array}{c} v \\ \langle i|\mathcal{H}_0+\mathcal{H}'|j\rangle \\ \langle j|\mathcal{H}_0+\mathcal{H}'|j\rangle - E \end{array} \end{vmatrix} = 0 \tag{2.5}$$

where v and c denote the two bands that are nearly degenerate. In addition, we know that $\langle v|H_0|v\rangle = -E_g/2$ and $\langle c|H_0|c\rangle = E_g/2$, where E_g is the L-point bandgap. Furthermore, due to the symmetry of the bismuth electronic structure, $\langle v|H'|v\rangle = \langle c|H'|c\rangle = 0$. Thus, equation 2.5 can be simplified to

$$\begin{array}{c} \\ c \\ v \end{array} \begin{vmatrix} \begin{array}{c} c \\ -E_g/2 - E \\ \frac{\hbar k}{m_0}\langle v|\vec{p}|c\rangle \end{array} & \begin{array}{c} v \\ \frac{\hbar k}{m_0}\langle c|\vec{p}|v\rangle \\ E_g/2 - E \end{array} \end{vmatrix} = 0 \tag{2.6}$$

By solving equation 2.6 and setting $\overleftrightarrow{P^2} = \langle v|\vec{p}|c\rangle\langle c|\vec{p}|v\rangle$, the following dispersion relationship is obtained

$$E(\vec{k}) = \pm\frac{1}{2}\sqrt{E_g^2 + 4\hbar^2\vec{k}\cdot\overleftrightarrow{P^2}\cdot\vec{k}/m_0^2}. \tag{2.7}$$

The Lax model presented in equation 2.7 is also known as the "ellipsoidal non-parabolic model" since it assumes ellipsoidal carrier pockets. Cohen et. al. modified this model by allowing for non-ellipsoidal carrier pockets [17]. Throughout this work the Lax 2-band model is used for all calculations because of its relative simplicity. For more information on the 2-band model, I recommend reference [18].

Since the dispersion relations of the L-point electronic bands are non-parabolic, the value of the effective mass depends on the definition used. Even though, for energies much larger than the bandgap, the dispersion relation is close to a linear relation, for energies near the band edge, the Lax model reduces to the familiar parabolic dispersion relations. Therefore, one common way to define the effective mass of the L-point bands is by taking a Taylor expansion about $k = 0$. The Taylor expansion is taken to second order, since the zeroth order term simply gives the bandgap and the first order term is zero. Taking the second-order Taylor expansion of equation 2.7

about $k = 0$ yields the following parabolic relation:

$$E(\vec{\kappa}) = \frac{1}{2}E_g + \frac{\hbar^2}{2m_0}. \tag{2.8}$$

Using this definition, the dimensionless inverse-effective mass tensor, $\overleftrightarrow{\alpha}$, is defined in terms of the dimensionless effective mass tensor $\vec{m^*}$ and the momentum matrix elements[16] :

$$\overleftrightarrow{\alpha} = (\overleftrightarrow{m^*})^{-1} = 2\frac{\overleftrightarrow{P^2}}{E_g m_0}. \tag{2.9}$$

Substituting equation 2.9 into equation 2.7 gives

$$E(\vec{k}) = \pm\frac{1}{2}\sqrt{E_g^2 + 2\hbar^2 E_g \vec{k}\cdot \overleftrightarrow{\alpha} \cdot\vec{k}/m_0}. \tag{2.10}$$

The effective mass can also be defined as a function of energy by rearranging equation 2.10 to fit the common parabolic dispersion relations and allowing the effective carrier mass to vary with energy as shown below:

$$\frac{\hbar^2\vec{k^2}}{2m_1^* m_0} = \frac{(2E)^2 - E_g^2}{4E_g} \tag{2.11}$$

$$\frac{\hbar^2\vec{k^2}}{2m_1^* m_0} = \frac{(2E - E_g)(2E + E_g)}{4E_g} \tag{2.12}$$

$$\frac{\hbar^2\vec{k^2}}{2m_1^* m_0} = (E - \frac{E_g}{2})(\frac{E}{E_g} + 1/2) \tag{2.13}$$

$$\frac{\hbar^2\vec{k^2}}{2m_1^* m_0} = \varepsilon(1 + \frac{\varepsilon}{E_g}) \tag{2.14}$$

$$m_1^*(\varepsilon) = m_1^*[1 + \varepsilon/E_g] \tag{2.15}$$

where ε is defined relative to the conduction band-edge, $E - E_g/2$. In equations 2.11-2.15, m_1^* is defined as

$$\frac{1}{m_1^*} = \vec{k}\cdot \overleftrightarrow{\alpha} \cdot\vec{k}. \tag{2.16}$$

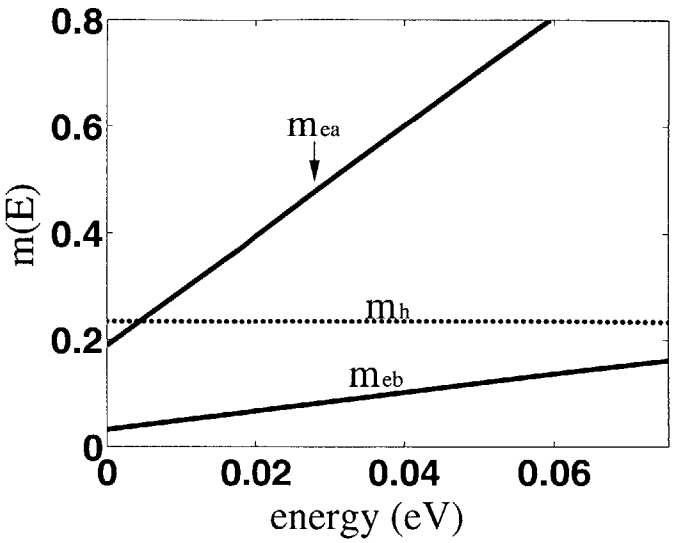

Figure 2-2: The effective mass of the L-point carriers in the < 012 > direction expressed in free electron mass units as a function of energy in eV. Of the three carrier pockets at the L-point, two are degenerate and their effective mass values are labeled "m_{eb}" in the figure. The effective mass of the third pocket is labeled "m_{ea}" and is non-degenerate. The effective mass of the T-point hole pocket in the < 012 > direction, labeled m_b, which follows a parabolic dispersion relation is shown for comparison.

From equation 2.15, we see that the L-point carrier effective mass increases with increasing energy.

Figure 2-2 shows the L-point effective mass in the < 012 > crystalline direction, as a function of energy at room temperature defined by equation 2.15. In this crystallographic direction, two of the three pockets are degenerate and these pockets are labeled "m_{eb}" in the figure. The third pocket is labeled "m_{ea}". The T-point effective mass in the < 012 > direction, labeled m_b, is shown for comparison. As can be seen by Fig. 2-2, even though the L-point carriers at low temperatures and at the band edge have effective mass components much smaller than the T-point carriers, away from the band edge and at room temperature, the T point and L-point effective mass values are comparable. Eventually, when the energy band approaches the next nearest band (> 1eV at 10K [9]), the 2-band model breaks down and coupling to higher order bands needs to be considered. Figure 2-2 shows the L-point effective mass component the along the wire axis for < 012 > crystallographically aligned wires. The effective mass components perpendicular to the wire axis, in the confined directions,

also increase with increasing energy.

It is important to note that the mass defined in equation 2.15 (and plotted in Figure 2-2) is defined as the effective mass needed, assuming a parabolic dispersion relation, to have a state of energy E and momentum k. This is not the same mass as a mass defined by the curvature (second derivative) of the dispersion relation at energy E. This mass would be much larger than the mass defined in equation 2.15 for a given energy.

The inverse effective mass which is relevant for transport equations is defined as $\alpha(\varepsilon) = (m_0/(\hbar^2 k))\nabla_k E$ [19]. From equation 2.14, y can be defined as

$$y = \frac{\hbar^2 \vec{k^2}}{2m_1^* m_0} = \varepsilon(1 + \frac{\varepsilon}{E_g}). \tag{2.17}$$

Using this definition of y, $\frac{dy}{dk}$ and $\frac{dy}{dE}$ are found to be the following:

$$\frac{dy}{dk} = \frac{\hbar^2 k}{2m_1^* m_0} \tag{2.18}$$

$$\frac{dy}{dE} = 1 + 2\frac{\varepsilon}{E_g} \tag{2.19}$$

so that,

$$\alpha_1(\varepsilon) = \frac{m_0}{\hbar^2 k}\nabla_k E = \frac{m_0}{\hbar^2 k}\frac{dE}{dy}\frac{dy}{dk} = \frac{m_0}{\hbar^2 k}\frac{1}{1 + 2\frac{\varepsilon}{E_g}}\frac{\hbar^2 k}{2m_1^* m_0} = \frac{1}{m_1^*(1 + 2\frac{\varepsilon}{E_g})} \tag{2.20}$$

where similar to m_1^* defined in equation 2.16, α_1 is defined as

$$\alpha_1 = \vec{k} \cdot \overleftrightarrow{\alpha} \cdot \vec{k}. \tag{2.21}$$

As in equation 2.15, equation 2.20 can be used to solve for the effective mass as a function of energy.

$$m_1^*(\varepsilon) = m_1^*(0)(1 + 2\frac{\varepsilon}{E_g}) \tag{2.22}$$

The effective mass tensors at the band edge of the T and L-points are very anisotropic [1]. The hole carrier pocket at the T-point can be characterized by an effective mass tensor

$$\mathbf{m}_h = \begin{pmatrix} m_{h1} & 0 & 0 \\ 0 & m_{h1} & 0 \\ 0 & 0 & m_{h3} \end{pmatrix}. \tag{2.23}$$

The hole mass components in the binary (x) and bisectrix (y) directions are equal, but the component in the trigonal direction is heavier. The T-point hole mass parameters are $m_{h1} = 0.059$ and $m_{h3} = 0.634$ [12]. The L-point electron and hole effective mass tensors are more complicated and can be expressed as

$$\mathbf{m}_e = \begin{pmatrix} m_{e1} & 0 & 0 \\ 0 & m_{e2} & m_{e4} \\ 0 & m_{e4} & m_{e3} \end{pmatrix}, \tag{2.24}$$

for the electron carrier pocket lying close to the bisectrix axis (labeled "A" in Fig. 2-1). The off-diagonal element m_{e4}, which has a positive value [20], resulting from a positive tilt angle $\theta \approx 6°$ of the longest principal axis of the ellipsoid away from the bisectrix axis. At low temperatures, $m_{e1} = .00113$, $m_{e2} = 0.26$, $m_{e3} = 0.00443$, and $m_{e4} = 0.0195$ [21]. The other two electron ellipsoids (labeled with B in Fig. 2-1) are obtained by rotation of ellipsoid A by $\pm 120°$ about the trigonal axis. Therefore, the effective mass tensor of the two B pockets are calculated by the following equations:

$$\mathbf{m}_{B1} = R\, m_A\, R' \tag{2.25}$$

$$\mathbf{m}_{B2} = R\, R\, m_A\, R'\, R' \tag{2.26}$$

Table 2.1: Band Overlap Energy vs. Temperature

T (K)	Efe (eV)	Efh (eV)	E_{over} (eV)
80	0.017	0.016	0.033
100	0.018	0.016	0.034
120	0.019	0.0165	0.0355
150	0.020	0.016	0.036
200	0.024	0.02	0.044
250	0.033	0.033	0.066
300	0.059	0.056	0.115

$$R = \begin{pmatrix} cos(120) & -sin(120) & 0 \\ sin(120) & cos(120) & 0 \\ 0 & 0 & 1 \end{pmatrix}, \tag{2.27}$$

where R is the unitary $2\pi/3$ rotation matrix for the coordinates and R' is its inverse.

Furthermore, the direct L-point bandgap (E_g), the band overlap (E_{over}), and the L-point effective masses (m_e^*) all increase with increasing temperature. For our calculations we used the variation of the band overlap with temperature, as deduced by Gallo and et al. from transport measurements [2]. The results from Gallo's study for the band overlap, the Fermi energy of the electrons (E_{fe}), and the Fermi energy of the holes (E_{fh}) are listed in Table 2.1.

The L-point bandgap, E_g, depends on temperature by the empirical relation

$$E_g = 13.6 + (2.1X10^{-3})T + (2.5X10^{-4})T^2 \tag{2.28}$$

where E_g is in meV and T is the temperature in Kelvin, as deduced by magneto-reflection studies [1]. The effective mass of the L-point carriers varies with temperature approximately according to the relation [1]

$$m^*(T) = m^*(0)(1 - 2.94X10^{-3}T + 5.56X10^{-7}T^2)^{-1} \tag{2.29}$$

also as deduced by magneto-reflection studies. The room temperature band parame-

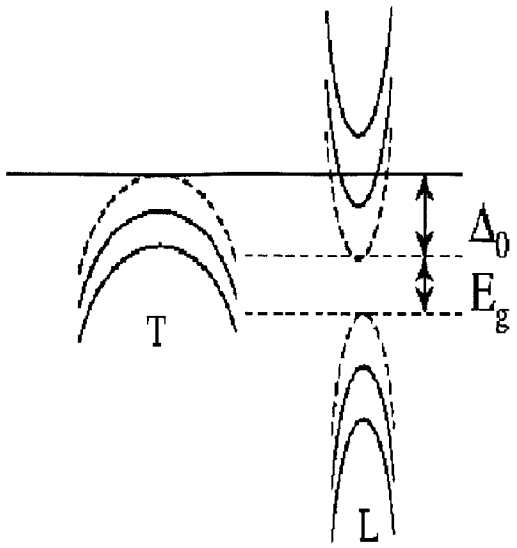

Figure 2-3: The L-point and T-point electronic subband structure in bismuth in the presences of quantum confinement. E_g is the L-point bandgap, and Δ_0 is the band overlap.

ters are discussed in relation to our experimental findings in Subsection 5.3.4.

2.1.2 QUANTUM CONFINEMENT IN BISMUTH NANOWIRES

When a material's size is smaller than both the de Broglie wavelength and the mean free path of the free carriers, then these carriers become quantum-confined. The electron and hole energy bands then split into subbands, characteristic of a low dimensional material.

Figure 2-3 shows an example of the effects of quantum confinement on the bismuth band structure. In this figure, the dotted lines represent the bulk dispersion relations for free carriers, while the solid lines show the subbands that are formed because of quantum confinement effects. Since, in the example shown, the wire diameter is smaller than the de Broglie wavelength of the L and T point carriers, the electronic structure has subbands at both the L and T points. When the diameter is decreased further, the energy separation between these subbands, as well as the bandgaps increase. In addition, because the dispersion relations of the free carriers at the L-point are highly non-parabolic, as the diameter decreases, the effective mass

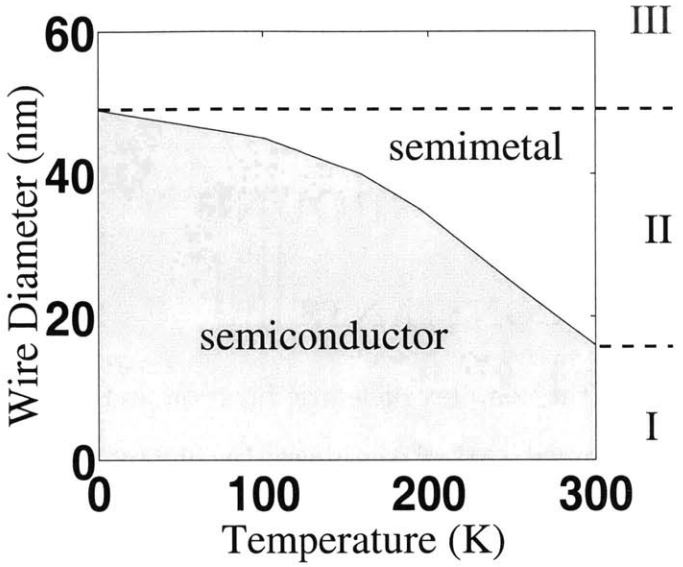

Figure 2-4: The phase diagram of the semimetal to semiconductor transition in bismuth nanowires is shown as a function of temperature and wire diameter. Depending on the wire diameter, a nanowire is either a semimetal (III), a semiconductor(I), or it switches from a semimetal to semiconductor as the temperature is decreased(II) from 300K to 0K.

components of the L-point carriers increase. Similarly, the non-parabolic bands result in each subband having a slightly different effective mass, increasing with increasing band edge energy.

Eventually, as the wire diameter decreases, the highest energy valence subband at the T-point becomes lower than the lowest conduction subband at the L-point. At this diameter, the bismuth nanowire becomes a new type of material, semiconducting bismuth. The calculated diameter of the semimetal to semiconductor (SM-SC) transition as a function of temperature for wires aligned in the $< 012 >$ direction (the growth direction of our nanowires) is shown in Fig. 2-4. Since the electron effective mass components at the L-point and the band overlap change with temperature, the SM-SC transition is strongly dependent on temperature. For example, at room temperature, the SM-SC transition is predicted to occur at a wire diameter of 16 nm, while at 77K, it occurs at 47 nm, see Fig. 2-4. The transition between a semimetal to an indirect gap semiconductor has significant effects on the electronic and optical properties of bismuth, since at this point, the number of free carriers drops rapidly.

When the diameter is decreased past the transition point, the indirect L-point to T-point bandgap increases as the wire diameter d_w decreases further.

2.2 OPTICS BACKGROUND

2.2.1 OPTICAL CONSTANTS

Throughout this work, the complex dielectric function and the complex index of refraction are used. The real part of the dielectric function, $\epsilon_1(cm^{-1})$, is related to the capacitance of the material, while the imaginary part of the dielectric function, $\epsilon_2(cm^{-1})$, is related to the conductivity in the sample. The real part of the index of refraction, $n(cm^{-1})$, denotes the speed of light inside the material, while the imaginary part of the index of refraction, $K(cm^{-1})$, is related to the optical absorption coefficient.

The complex dielectric function $(\epsilon_1 + i\epsilon_2)$ is the square of the complex index of refraction. So that

$$\epsilon_1 + i\epsilon_2 = (n + iK)^2, \tag{2.30}$$

or equivalently,

$$\epsilon_1 = n^2 - K^2 \; and \; \epsilon_2 = 2nK \tag{2.31}$$

2.2.2 EFFECTIVE MEDIUM THEORY

Much research has been done on predicting the dielectric properties of heterogeneous mixes of materials. Applications for this work span many areas of research, such as work on sedimentary rocks [22], interactions between microscopic gold particles [23], and studies of silver nanowires [24]. Interest in this area began as early 1904 [25, 26] and continues today with research to improve the models, find their limits, and apply them to different situations. In all of these research projects, the idea remains the same. In a heterogeneous sample that is homogeneous on the length scale of the

probing light, the observed dielectric function of the composite can be related to the dielectric functions of the pure materials.

In the limit where all the interfaces are either all parallel or all perpendicular to the applied electric field, the dielectric function can be solved very simply and exactly. When the electric field never crosses an interface but is parallel to the boundaries, the situation is analogous to two capacitors in parallel and the dielectric functions are weighted by their volume percentages and then added together. In the other limit where the electric field crosses every boundary between the two materials, the situation is similar to capacitors in series and the inverse of the dielectric functions are weighted by their volume fractions and then added. When the material is not in one of these two limits, but instead is described by a distribution of shapes and sizes, approximations are used to estimate the dielectric function of the composite.

Many approximations and modified versions of these approximations have been derived and then tested for different limiting conditions. By far the most popular, and one of the first developed theories (1904) is the Maxwell - Garnett Effective Medium Theory (MGEMT) [25, 26].

MGEMT can be derived from the Lorentz-Lorenz effective medium expression:

$$\frac{\epsilon_{\text{composite}} - \epsilon_{\text{host}}}{\epsilon_{\text{composite}} + K * \epsilon_{\text{host}}} = f_a \frac{\epsilon_{\text{a}} - \epsilon_{\text{host}}}{\epsilon_{\text{a}} + K * \epsilon_{\text{host}}} + f_b \frac{\epsilon_{\text{b}} - \epsilon_{\text{host}}}{\epsilon_{\text{b}} + K * \epsilon_{\text{host}}} \tag{2.32}$$

where ϵ_{a}, ϵ_{b}, ϵ_{host}, and $\epsilon_{\text{composite}}$ are the dielectric functions of material a, material b, the host, and the composite, respectively, K is the screening parameter, f_a and f_b are the volume fractions of materials a and b in the composite, $f_b = 1 - f_a$. For infinitesimally small nanowires, K = 1.

MGEMT is obtained by setting ϵ_{host} equal to ϵ_{b}, thus assuming that the volume fraction of material b is much greater than for material a. For bismuth nanowires in alumina, we assume that material a is bismuth, while material b is alumina. Making these substitutions, we obtain the MGEMT:

$$\frac{\epsilon_{\text{composite}} - \epsilon_{\text{alumina}}}{\epsilon_{\text{composite}} + K * \epsilon_{\text{alumina}}} = f \frac{\epsilon_{\text{bismuth}} - \epsilon_{\text{alumina}}}{\epsilon_{\text{bismuth}} + K * \epsilon_{\text{alumina}}} \tag{2.33}$$

Other EMTs are similar. For example, the Bruggeman effective medium theory uses a self consistent approach by setting ϵ_{host} equal to $\epsilon_{composite}$. Much research has been done to determine which EMT is best for specific different cases. No EMT clearly is the best for all situations. For a review of some effective medium theories, I recommend reference [27].

The exact solution for cylindrical pores was solved by Cherkas [28]. When this solution is modified to account for the pores filled with bismuth, the MGEMT equation with the screening parameter, K, equal to 1 is reached. For more information on EMTs see Appendix A.

2.3 APPLICATIONS OF NANOWIRES

Quantum confinement of the free carriers in a metal fundamentally changes the way these free carriers respond to the world around them. The magnetic, optical, and electrical properties of a material can change significantly under quantum confinement. The increased surface area, singularities in the density and joint density of states, enhanced exciton binding energies, increased bandgap, and increased surface scattering with decreasing wire diameter are just some of the ways in which one-dimensional materials differ from their corresponding bulk materials. Nanowires, compared to other low dimensional systems, have the maximum amount of confined directions while still leaving one not confined direction for electrical conduction, thus allowing nanowires to be used for applications where an electrical contact is needed and tunneling transport would be difficult. Of particular interest to the application of low dimensional materials is the ability to independently control critical parameters which in a 3D crystalline materials are interdependent, or the ability to benefit from some property which can be enhanced non-linearly because of its dependence on the electronic density of states or on some other property.

Although bismuth nanowires are not useful for all the applications discussed below, what is learned by studying bismuth nanowires might be applied to other nanowires, and therefore this section summarizes applications for nanowires in general.

2.3.1 MAGNETIC APPLICATIONS

Nanowires are currently being investigated for magnetic applications [29, 30]. For example, appropriate magnetic nanowires could be used for magnetic memory applications [30]. To store information in a magnetic memory, the magnetic energy required to switch a magnetic domain must be larger than the thermal energy, k_BT. This magnetic energy can be increased by either increasing the volume or the geometrical anisotropy constant of the material. If the volume is increased, the particle size is increased, and hence the resolution is decreased. In nanowires, the anisotropy is very large, so that the magneto-static switching energy is above the thermal energy, while the diameter is small, so that the spatial resolution can be large. Thus nanowires can, in principle, form stable and highly dense magnetic memory arrays with packing densities as large as 10^{11} wires/cm^2 or tera-bits/inch^2. This research direction is currently being pursued.

2.3.2 THERMOELECTRIC APPLICATIONS

Another possible application for nanowire arrays is thermoelectric energy conversion [31], the conversion between thermal and electrical energy. In a thermoelectric material, a temperature change along the sample creates a corresponding voltage drop, which is proportional to the thermopower. Likewise, an applied voltage creates a temperature gradient across the sample. Thermoelectric cooling makes use of this effect by using electrical current to cool the thermoelectric material and hence to cool surrounding objects, such as integrated circuits, superconductors, or beer in a commercial cooling unit. Thermoelectric cooling can, in principle, be used instead of conventional air conditioning. However, at present levels of efficiencies, this is not a cost effective application.

The conversion of a temperature difference into electricity has many interesting applications. One of the more appealing applications is heat recovery in power generation. In a steam turbine plant, considerable heat energy is wasted in the discharged effluents, even with the most efficient of heat recovery processes. Sometimes this

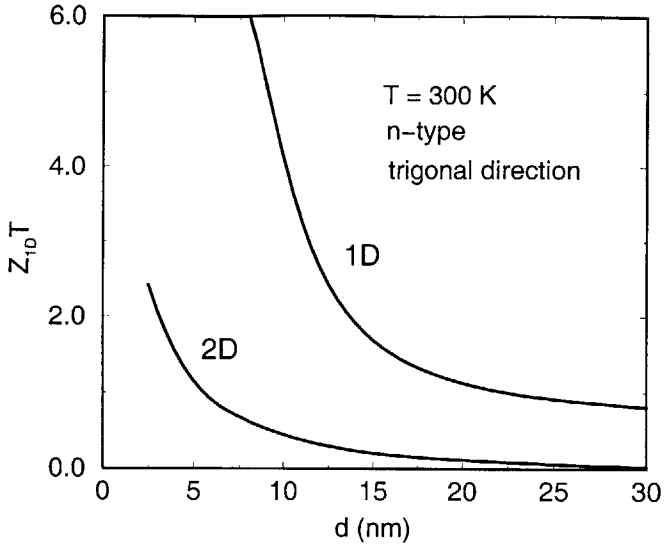

Figure 2-5: The increase in the dimensionless figure of merit within the quantum-confined systems of bismuth as a function of wire diameter or quantum well thickness. The thermoelectric properties are expected to improve greatly when the wires are small enough to become one dimensional. (Figure compliments of Yu Ming Lin.)

energy is used for hot water heating purposes, like in MIT's co-generation plant. However, more often than not, this energy is drained into cooling lakes and streams, and causes a host of environmental problems because of local heating effects. A cost effective, efficient thermoelectric device could help increase power plant efficiency and decrease thermal pollution. In addition, thermoelectric power generation can be used to recover energy lost to heat in automobiles. The gas internal combustion engine in a typical car is only 20-25% efficient. The engine therefore heats up to 440° C. The temperature difference between the engine and the cool air can allow a thermoelectric device to recover some of the lost energy and to increase gas mileage.

The efficiency of a thermoelectric device is measured in terms of a dimensionless figure of merit ZT, where Z is defined as

$$Z = \frac{\sigma S^2}{\kappa}, \tag{2.34}$$

in which σ is the electrical conductivity, S is the Seebeck coefficient (the temperature difference across the sample at a given voltage), κ is the thermal conductivity, and

T is the temperature. In order to achieve a high ZT and therefore a highly efficient thermoelectric, a high electrical conductivity, low thermal conductivity, and a high Seebeck coefficient are simultaneously required. In the best thermoelectric devices, the electrical carriers dominate the thermal conductance, and an increase in the carrier density improves the electrical conductance, but also increases the thermal conductance and decreases the Seebeck coefficient. Since there are more carriers to carry both charge and heat, the electrical and thermal conductances are increased simultaneously. This effect is known as the Wiedemann-Franz law. The Seebeck coefficient is decreased when the electrical conductivity is increased, because the temperature difference from one side of the sample to the other decreases with enhanced thermal conduction. Hence an increase in conductivity both decreases the Seebeck coefficient and increases the thermal conductivity. These two trade-offs set the limit for ZT in bulk materials, so far limiting the maximum achieved ZT to ~ 1 at room temperature for commercial applications.

The high electronic density of states in a quantum-confined structure is proposed as a way to bypass the Seebeck/electrical conductivity trade-off and allow for an increased electrical conductivity, a relatively low thermal conductivity, and a large Seebeck coefficient all at once [8]. Figure 2-5 shows theoretical values for ZT vs. sample size for both 2-D and 1-D n-type bismuth systems along the trigonal axis where ZT is considered only for the quantum-confined region. As the quantum confinement becomes stronger, the figure of merit is predicted to far exceed the limits of current technology [8]. Already, the validity of simple models have been confirmed. With low dimensional systems, ZT values as high as ~ 2 have been demonstrated [32, 33].

Qualitatively one can understand the simultaneously large S and σ in low dimensional materials by a simple explanation. The difference in Fermi energies at the sample ends is the voltage across the sample. In order to increase the figure of merit, the difference in the Fermi energies at the two sample ends needs to be maximized, while maintaining their temperature difference. If quasi-neutrality is assumed, then the carrier concentration across the sample is constant. (This isn't completely true, but for this simple explanation it is a fair approximation.) If the electronic density of

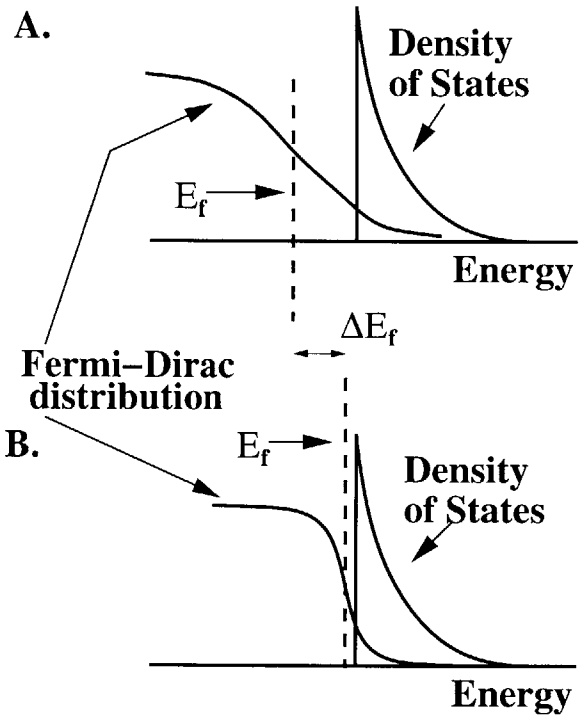

Figure 2-6: The effect of temperature on the Fermi energy and the Fermi distribution in the presence of a singularity in the density of states. A. At high temperature the Fermi energy must move away from the singularity to prevent having too high a carrier concentration. B. At low temperatures, the Fermi energy must move closer to the singularity to ensure a sufficiently high carrier density.

states has a sharp peak slightly above the Fermi energy, then at high temperatures, electrons can be excited into these states, while at low temperatures, carrier excitation is unlikely. In other words, the high density of states is "seen" at high temperatures and is less "seen" at low temperatures. In order to keep the total number of carriers constant (quasi-neutrality), the Fermi energy of the hot side must shift downwards to compensate for the large number of carriers excited into the density of states peak. At the low temperature side, the Fermi energy must remain close to the peak in the electronic density of states to allow for the optimization of the free carrier density, shown in Fig. 2-6. The large difference in Fermi energies makes for a large Seebeck coefficient, while the high density of states allows for a large electrical conductivity. Hence low dimensional materials can simultaneously have a large Seebeck coefficient and a large electrical conductivity.

Nanowires also have the added advantage for thermoelectric applications of a decreased phonon contribution to the thermal conductivity due to increased phonon scattering at the wire boundary. The decrease in the thermal conductivity also enhances ZT by Equ. 2.34. Although the application of nanowires to thermoelectric applications is very promising, these materials are still in the research phase of development, and quite far from being incorporated into a useful product.

2.3.3 OPTICAL APPLICATIONS

Nanowires also hold promise for optical applications. 1-D systems exhibit a singularity in their joint density of states, allowing quantum effects in nanowires to be readily observable, sometimes, even at room temperature. Since the electronic density of states of a nanowire in the quantum limit (small wire diameter) is highly localized in energy, the available states quickly fill up with electrons as the intensity of the incident light is increased. This filling up of the subbands, as well as other effects that are unique to low-dimensional materials, lead to strong optical non-linearities in quantum wires. Quantum wells and quantum wires, thus may yield optical switches with a lower switching energy and increased switching speed compared to currently available optical switches.

Quantum wires have been studied for laser applications. Since quantum wires utilize exciton lasing action, quantum wires form lasers with lower excitation thresholds and a decreased temperature sensitivity in their performance [34] compared to their bulk counterparts. Furthermore, the emission wavelength can be tuned for a given material composition by only altering the geometry of the wire.

Lasing action has been reported in ZnO nanowires with wire diameters ($40 - 150nm$) smaller that the wavelength of the light emitted ($\lambda = 385\,\text{nm}$) [35]. Since the edge and lateral surface of ZnO nanowires are faceted, they form optical cavities that sustain desired cavity modes. The ZnO nanowires exhibit a lower lasing threshold ($\sim 40\,\text{kW/cm}^2$) than their 3D counterparts ($\sim 300\,\text{kW/cm}^2$). In order to utilize exciton confinement effects in the lasing action, the exciton binding energy ($\sim 60\,\text{meV}$ in ZnO) must be greater than the thermal energy ($\sim 26\,\text{meV}$ at $300\,\text{K}$). Decreasing the wire diameter increases the excitation binding energy and lowers the threshold for lasing.

Laser action has been also observed in GaN nanowires [36]. Unlike ZnO, semiconducting GaN has a small exciton binding energy of only $\sim 25\,\text{meV}$. Furthermore, since the wire radii used in this study (15–75 nm) are larger than the Bohr radius of excitons in GaN (11 nm), the exciton binding energy is not expected to increase with decreasing wire diameter and quantum confinement are not expected for this diameter range. However, some tunability of the center of the spectral intensity was achieved by increasing the intensity of the pump power, causing a red-shift in the laser emission, which is explained as a bandgap re-normalization as a result of the formation of an electron-hole plasma. Heating effects were excluded as the source of the spectral shift.

Nanowires have been proposed for optical switching [37–39]. Light with its electric field normal to the wire axis excites a transverse free carrier resonance inside the wire, while light with its electric field parallel to the wire axis excites a longitudinal free carrier resonance inside the wire. Since wires are highly anisotropic, these two resonances occur at two different wavelengths and thus result in absorption peaks at two different energies. In one study, gold nanowires dispersed in an aqueous solution align along the electric field when a DC voltage is applied. The energy of the absorption

peak can be toggled between the transverse and longitudinal resonance energies by using an electric field to change the alignment of the nanowires under polarized light illumination [38, 39]. Thus, this method provides one way to achieve electro-optical modulation.

Nanowires may also be used as barcode tags for optical read out. Nanowires containing gold, silver, nickel, palladium, and platinum were fabricated [40] by electrochemical filling of porous anodic alumina, so that each nanowire consisted of segments of various metal constituents. Thus many types of nanowires can be made from the five metals used in this study, and each type of nanowire can be identified by its unique order of the metal segments along wire axis and the length of each segment. Barcode read out is possible by reflectance optical microscopy. The segment length is limited by the Rayleigh diffraction limit, and not by synthesis limitations, and thus the segment length can be made as small as 143 nm.

Both the large surface area and high conductivity along the length of nanowires are utilized in semiconductor-organic solar cells. In a semiconductor-organic solar cell, the incident light forms bound electron-hole pairs (excitons) in both the inorganic nanocrystal and in the surrounding organic medium. These excitons diffuse to the semiconductor-organic interface and disassociate to form an electron and a hole. Since conjugated polymers usually have poor electron mobilities, the inorganic phase is chosen to have a higher electron affinity. The separated electrons and holes drift to the external electrodes through the semiconductor and organic materials, respectively. However, only those excitons formed within an exciton diffusion length from an interface can disassociate before recombining, and therefore the distance between the dissociation sites limits the efficiency of a solar cell. Furthermore, once the carriers are separated, they need to be transported to the anode/cathode of the device. However, usually if a large surface area is used, the electrical transport is limited to carrier hopping, and thus electrical transport also limits the efficiency of the cell. Nanowires provide both a large surface area for efficient exciton disassociation as well as a continuous conduction path along the length of the wires. Thus, these semiconductor nanowire - organic solar cells yield high electrical conversion efficiencies [41]. A

solar cell prepared from a composite of CdSe nanorods inside poly (3-ethylthiophene) yielded 6.9% monochromatic power efficiencies and 1.7% power conversion efficiencies under A.M. 1.5 illumination (equal to solar irradiance through 1.5 times the air mass of the earth at direct normal incidence). In addition, the enhanced absorption coefficient of nanowires and their tunable bandgap are also characteristics that can be used to enhance the energy conversion efficiency of solar cells [41].

Bismuth nanowires have their own unique properties. For example, quantum wells, quantum dots, and quantum wires usually have to be doped in order to populate the lowest subband and allow for optical excitation of the electrons to higher subbands. However, since the direct bandgaps for our wires are smaller than $3k_BT$ at room temperature, the lower subbands are partially filled with electrons even in undoped samples, and intersubband transitions thus should be observable. In addition, the selection rules for arrays of aligned quantum wires, such as for our bismuth nanowires, allow optical absorption to occur for light incident perpendicular to the wire axis (in-plane absorption). In-plane optical absorption greatly simplifies device testing, improves the ease of measurements, and may make nanowires in alumina useful for optical applications. For all of these and many other reasons, nanowires and in particular bismuth nanowires, hold potential for optical applications.

Chapter 3

SAMPLE FABRICATION

Bismuth nanowires in anodic alumina were first fabricated by the Dresselhaus-Ying group in 1997 [42, 43], and subsequently have been fabricated by the Huber and Foss team [44, 45]. The fabrication of alumina is described in both sections 3.1 and 3.2. Section 3.1 describes the general alumina fabrication, while section 3.2 extends this method to the fabrication of templates with larger pore diameters. Section 3.3 describes how our group fills the alumina pores with bismuth. Section 3.4 explains how free-standing wires are obtained from the bismuth in alumina samples. Lastly, section 3.5 presents XRD and TEM data used to characterize our bismuth nanowires.

3.1 Al_2O_3 TEMPLATE PREPARATION

In this study, anodic alumina was chosen as the host material, since it forms cylindrical pores with a structural arrangement that allows ordered arrays of metallic nanowires to be prepared in the form of a dense self-assembled hexagonal array. In addition, the pore size (the wire diameter) and the alumina thickness (the wire length) can be controlled by varying the anodization voltage and the etch time, respectively. The wide bandgap of anodic alumina electrically isolates each wire by containing the free carriers inside the bismuth, and therefore provides is a good host material for nanowires.

To fabricate the template, $1.5X0.5mm^2$ sheets of aluminum foil are cut from a

large $100X100\,mm$, $0.5\,mm$ thick, 99.99% pure, aluminum foil purchased from Alfa Aesar. The sheet is placed between two glass sheets and mechanically pressed. Before the aluminum is anodized, the aluminum surface must be smooth. Therefore, the samples must first undergo a five step mechanical polish and an electro-chemical polish. Before the electro-chemical polish, the sample is annealed at 350°C for one hour. During the electro-chemical polish, 20 volts are applied between a platinum electrode and the mechanically polished aluminum sheet, as shown in Fig. 3-1. Both the platinum and aluminum are immersed inside an electrolyte. The aluminum sheet is electro-chemically polished for either 10-15 seconds in an electrolyte of phosphoric and chromic acids (95 volume % H_3PO_4, 5 volume % H_2SO_4, and 20 g/l CrO_3), or for several minutes in an electrolyte of perchloric acid and ethanol. If the polish is performed in phosphoric and chromic acids, an oil bath and heater are used to keep the electrolyte at 80°C. In the case of the perchloric acid and ethanol electrolyte, the acid is kept at a temperature of $\sim$ 5°C. The quality of the electro-chemical polish was improved when the aluminum sheets were covered with an insulating polymer (nail polish) on the unpolished back side, and allowed to dry for several hours before the electro-chemical polish. Using this method, only one side of the sample is polished, so the current is decreased and the polish became more uniform. After the polish, the polymer is removed with an acetone etch.

For the phosphoric/chromic acid etch, the voltage is set to 20V and the current is limited to 1.5mA. In the first few seconds of the polish, the current is 1.5mA and the voltage is slightly less than 20V. After about 5 seconds, the voltage reaches 20V, and the current drops exponentially. After the current decays to about 0.5mA, the power source is turned off, and the sample is quickly removed from the acid and is thoroughly rinsed with de-ionized (DI) water. In practice, however, the current doesn't always decay exponentially, and since a couple seconds of over polishing destroys the sample, a better way to determine when to end the polish is simply by limiting the time of the polish. For an oil bath at 80±1°C, the ideal polish time was found to be 11 seconds. A schematic of the anodization and electro-chemical polish set up is shown in Fig. 3-1.

Next the alumina formed during the anneal and the electro-chemical polish is

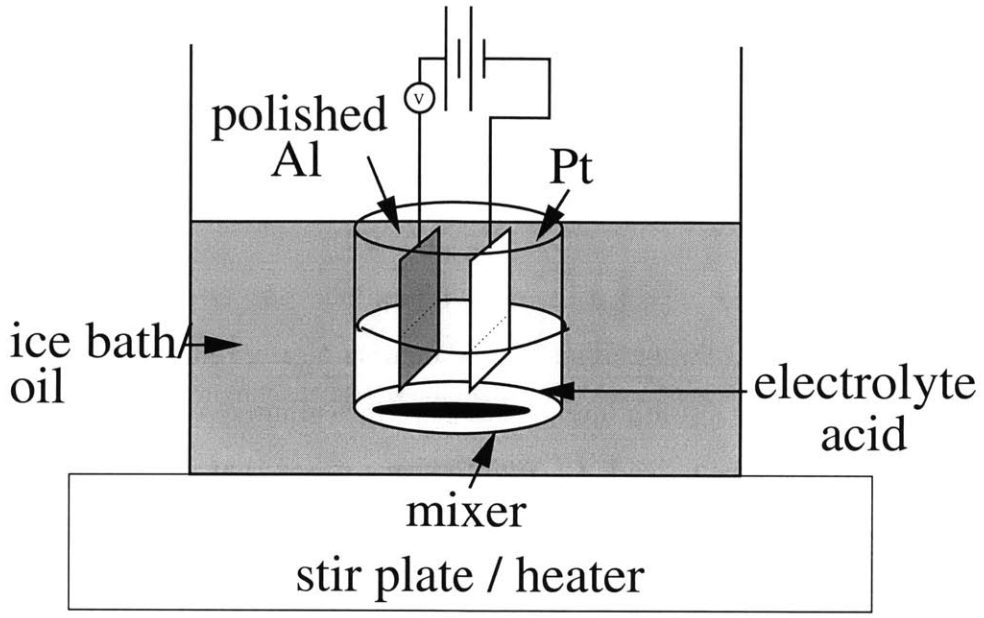

Figure 3-1: The electro-chemical and anodization setup. In the case of high voltage anodizations used to fabricate large pore alumina templates, the ice bath is filled above the acid level, and the stirring of the electrolyte is aggressive.

Table 3.1: Anodization Conditions of Voltage, Temperature, and Electrolyte

V	Electrolyte	T (°C)	pore diameter (nm)
20	20% sulfuric acid (H_2SO_4)	<3	20
40	4% oxalic acid ($C_2H_2O_4$)	10	40
160	10% phosphoric acid (H_3PO_4)	<3	200

removed in an etch solution of 3.5 volume % phosphoric acid and 45g/l of chromic acid. After the sample is mechanically and electro-chemically polished, and the alumina formed during the polish procedure is etched off, the sample is ready for anodization. The same basic setup is used for the anodization as is used for the electro-chemical polish, except that a different voltage is applied and the temperature and type of the electrolyte are different. Table 3.1 lists examples of three anodization recipes used in this thesis.

Since at least 1968, the anodization of aluminum into porous alumina has held the fascination of researchers [3, 46]. The atomic density of aluminum inside alumina is half that of aluminum, so as aluminum is anodized into alumina it expands by roughly a factor of 2. This expansion leads to compressive stresses that cause the alumina to grow up from the aluminum. As the alumina grows, pores are formed in which the O^{2-} and OH^{-} ions can drift to the aluminum and the Al^{3+} ions can drift into the acid. At the bottom of the pores is a thin layer of alumina which is referred to in the literature as the barrier layer, as shown in Fig. 3-2. The pores form with uniform diameters and uniform barrier layer thicknesses because of a delicate balance between electric-field-enhanced diffusion which determines the growth rate of the alumina, and dissolution of the alumina into the acidic electrolyte [3]. For each voltage setting, the alumina has a preferred barrier layer thickness, which corresponds to a specific pore diameter. Hence a fixed voltage reproducibly produces pores with the same diameter. As shown in Fig. 3-2(a), when the pore diameter is larger than the preferred diameter, the barrier layer is smaller, and the field enhanced diffusion of the O^{2-} ions results in an increased oxidation of the aluminum film. This in turn increases the barrier layer and decreases the pore size. As shown in Fig. 3-2 (c), when the pore diameter is smaller than the preferred diameter, the barrier layer is larger, and the etch rate dominates over the field-enhanced diffusion and consequently decreases the barrier layer. This in turn increases the pore size and returns the pore diameter and barrier layer to their preferred values [3].

When the the anodization voltage is increased, the pore diameter, barrier layer thickness, and pore periodicity are increased. The pore periodicity is reproducibly

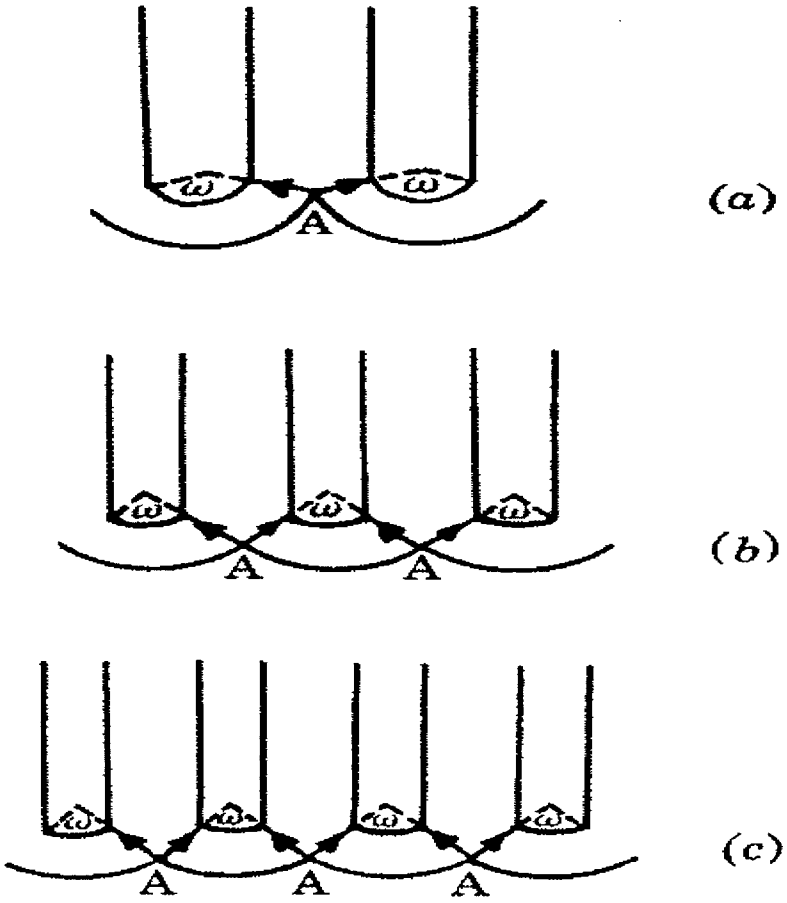

Figure 3-2: The pores in alumina during anodization. (a) The pore diameter is larger and the barrier layer thinner than for the preferred pore diameter. The thinner barrier layer favors electric field enhanced diffusion over etching, thus increasing the barrier layer and decreasing the wire diameter. (b) The pore diameter is such that the etch rate and anodization rate are equal. (c) The pore diameter is smaller and the barrier layer larger than for the preferred pore diameter. Thus, etching is favored over electric field enhanced diffusion and the barrier layer is decreased and the pore widened [3].

shown to scale as 2.77 times the applied voltage [3]. By varying the voltage, the pore diameter can be varied from 7 to 250 nm.

Not only are the pores formed by anodizing aluminum all of the same diameter, but they also self-assemble into a hexagonal array. One theory explains this self-ordering by the mechanical stresses at the aluminum-alumina interface due to expansion during the anodization. This stress produces a repulsive force between the pores, causing them to arrange in a hexagonal lattice [47]. Groups have found that in order to obtain well-ordered porous structures, they need to reach a complicated balance between the etch rate and the electric field enhanced diffusion which determines the oxide growth rate. Often, a different pore size or pore periodicity is needed. In order to obtain a well-ordered hexagonal pore structure, other experimental parameters need to be modified along with the voltage. For example, researchers have varied the voltage, the temperature, the electrolyte acid type, the acid concentration, and the aluminum preparation method [3, 46–49]. For small diameters and small periodicity ($< 30nm$), sulfuric acid is used and voltages $< 30V$ are applied. For diameters around 50nm, oxalic acid is used and voltages of about 40V are applied. For larger diameter pores, phosphoric acid is used and voltages of $\sim 200V$ are applied.

Even with the optimal choice of electrolyte, voltage, temperature, and polishing technique, the self-ordering process is not instantaneous and the first alumina grown is poorly ordered. To avoid having this unordered alumina in the final template, a two step anodization process can be employed, where an oxide is grown, etched off, and then a second oxide with a higher degree of ordering is grown [50]. In this process the first oxide leaves microdents in the aluminum that then serve as preordered nucleation sites for the pores that develop during in the second oxide growth. The final alumina is more ordered, the longer the first oxide is allowed to grow for. Top view SEM pictures of anodic alumina after the first and second anodizations are shown in Fig. 3-3. The top view of the alumina after the first anodization shows the very first alumina formed on this sample, while the top view after the second anodization shows the first alumina grown in the second anodization after the first anodization is etched away. If the remaining aluminum is removed with either mercury chloride or

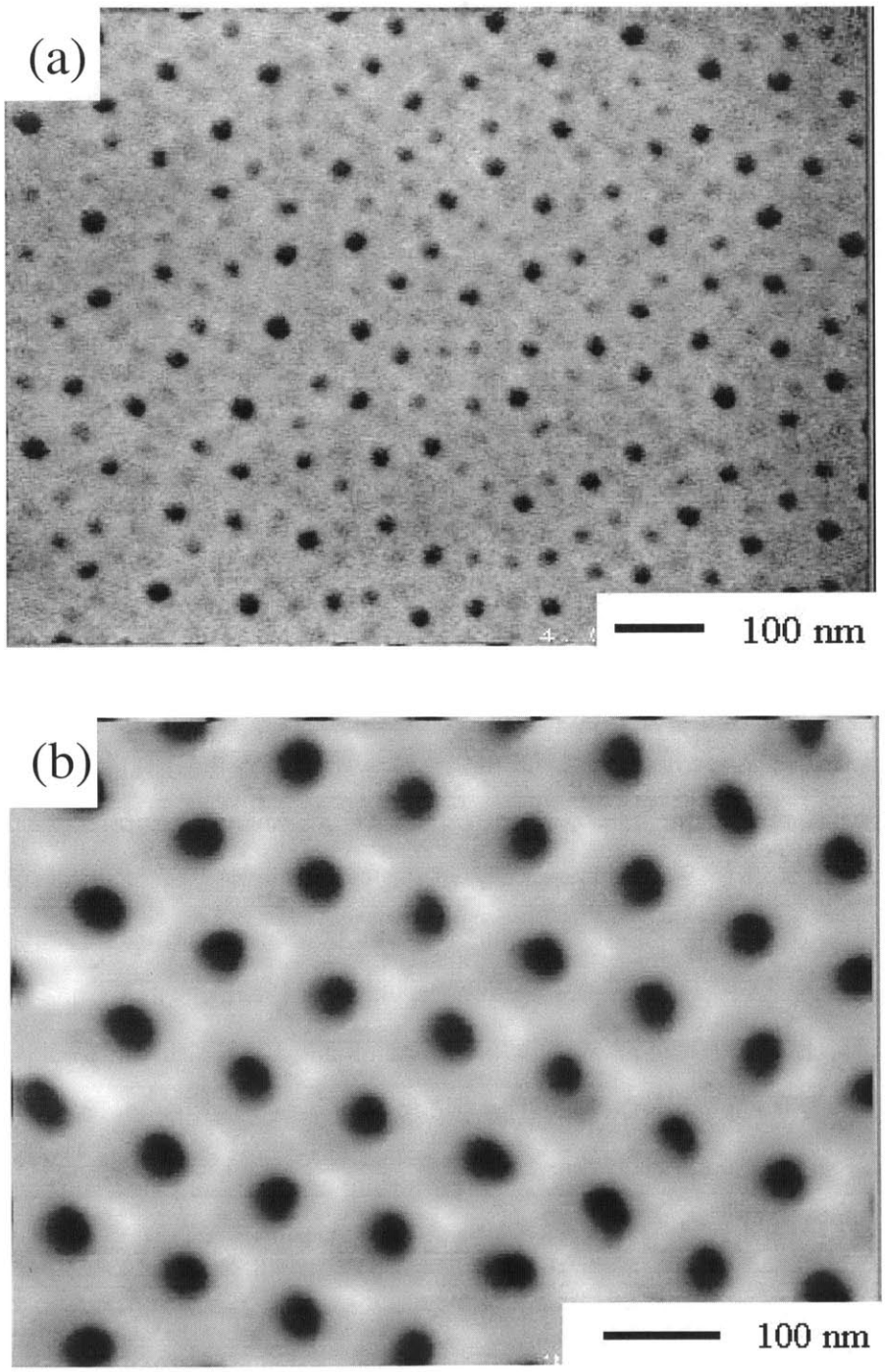

Figure 3-3: Top view SEM pictures of anodic alumina anodized at 45V in 4wt%$H_2C_2O_4$ after the first (a) and second (b) anodizations. (Figures are compliments of YuMing Lin.)

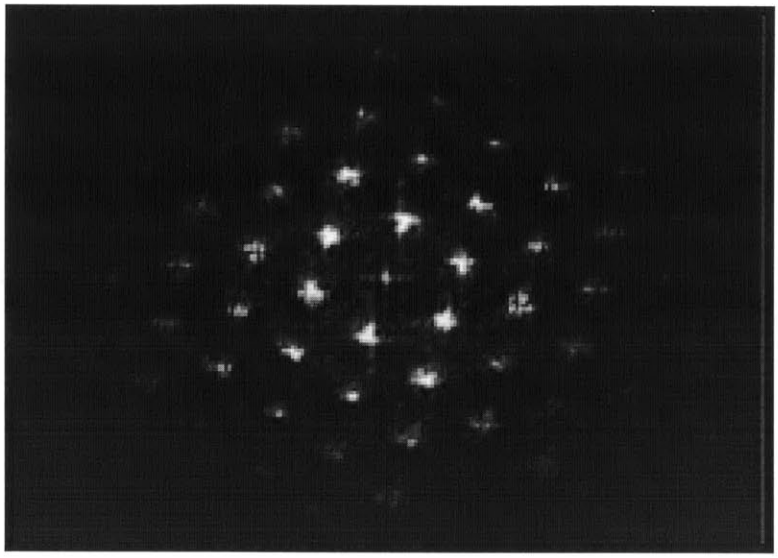

Figure 3-4: A Fourier transform of an SEM image of a very well-ordered alumina template. (Figure is compliments of Karlene Maskaly.)

copper chloride, the alumina nearest to the aluminum can be viewed. The ordering is better on this side than on the top side, since this alumina is the last alumina to be grown and the ordering improves throughout the anodization.

Figure 3-4 shows a Fourier transform of an SEM image from a very well-ordered alumina template. The hexagonal structure is evident in the Fourier transform. Figure 3-5 shows a top view and a cross sectional view of the alumina formed on a silicon wafer. The thicknesses of the samples used in this thesis are 40 - 60 μm, resulting in nanowires with an aspect ratio (length / diameter) on the order of 10^3.

3.2 ULTRA COOL METHOD OF ANODIZATION TO FORM LARGE PORE ALUMINA

When studying the effects of quantum confinement, we desire different samples with different wire diameters. The full set of samples should include those without, at the onset, and with strong quantum confinement. We are able to easily fabricate well-ordered small pore alumina ($< 30nm$) and medium pore alumina ($40 - 55nm$).

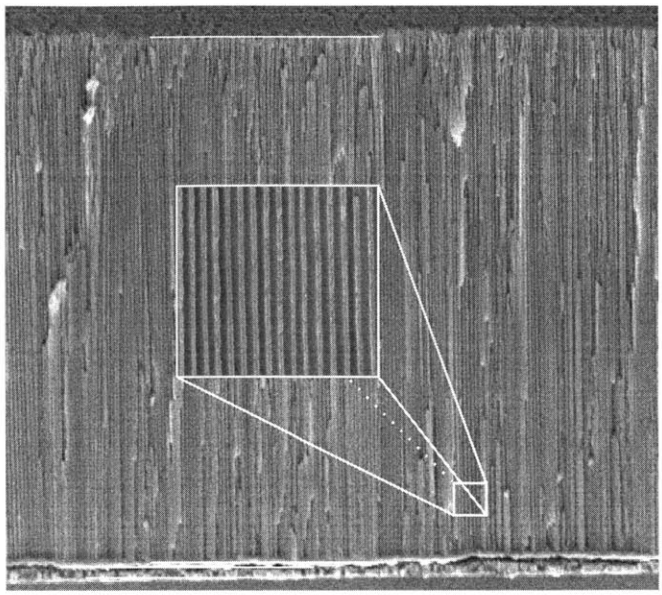

Figure 3-5: A cross section of a porous alumina template on top of Si. The pores go completely through the alumina. (Figure is compliments of Oded Rabin.)

However, alumina with pore sizes which form bismuth nanowires without quantum confinement ($> 100nm$) are much more difficult to fabricate since the high voltages cause local heating effects [4]. Wires with diameters around $100nm$ are key to understanding the absorption spectra of the nanowires. These large diameter wires are small enough to have significant surface effects, but not large enough to have significant quantum confinement. They, therefore, allow us to distinguish between optical absorption spectra features originating from quantum effects and those from surface effects. As part of this thesis, a method to fabricate large pore anodic alumina was developed in collaboration with Professor Yoel Fink and Karlene Maskaly.

Several theories have been presented to explain the formation of the porous alumina, such as Refs. [3] and [48]. In addition, several theories have been recently proposed to explain the ordering of the pores into a hexagonal pattern when very specific conditions for the anodization are used [49, 51]. Recently, a study showed that an optimal porosity of 10% is required to have well-ordered pores [52]. Many papers present excellent experimental results documenting conditions at which the anodization forms ordered pores and those at which the pores are irregular and not

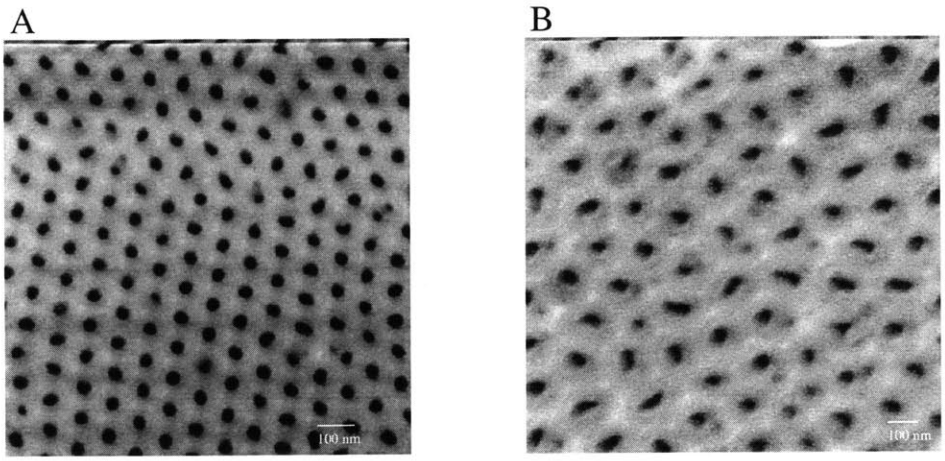

Figure 3-6: Scanning electron microscope images of two samples. The sample shown in (a) was anodized near the optimal voltage for a 4% oxalic acid electrolyte, while sample (b) was anodized above this voltage. Hence, sample (a) has a narrow distribution of wire diameters around 35 nm, while sample (b) has a wide distribution of wire diameters around ~70 nm.

ordered [45, 53, 54]. However, to our knowledge, no complete theory exists to predict the optimal acid type, concentration, and temperature that should be used to obtain well-ordered arrays with a uniform pore diameter for a given anodization voltage and corresponding pore diameter. Therefore, developing a new recipe is time consuming and requires many attempts to establish the recipe for well-ordered large pore anodic alumina. Figure 3-6 shows samples fabricated at optimal (a) and non-optimal (b) anodization conditions.

To minimize the trial and error required to find the ideal anodization conditions for large diameter pores (> 100 nm), we sought to reproduce the well-ordered arrays with a pore size of 200 nm diameter reported in Ref. [49]. However, when repeating their conditions of 160 V anodization voltage in 10 % phosphoric acid at 3°C, the anodization current became unstable. The current increased during the anodization, increasing the temperature of the acid. The rise in temperature in turn further increased the current, until the reaction became uncontrollable. This rapid rise in acid temperature and anodization current is called "breakdown" in the literature. [51]

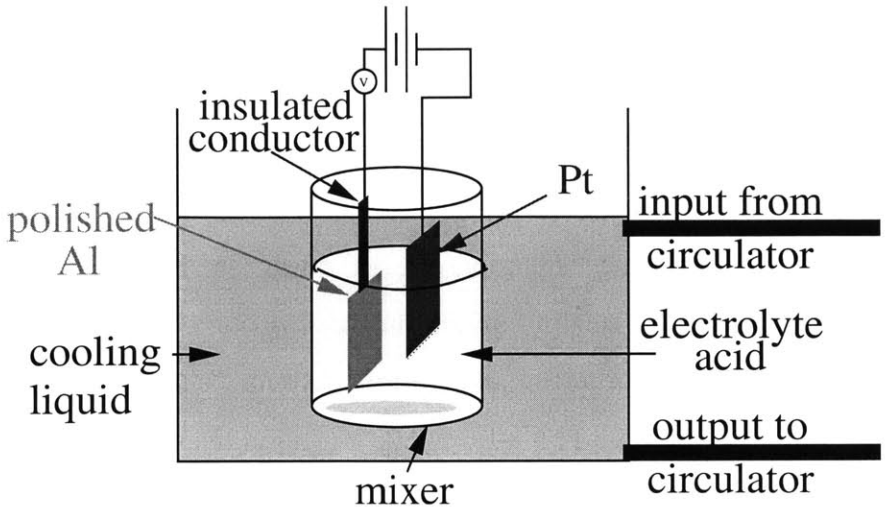

Figure 3-7: The anodization setup for high voltage anodization. The automatic cooling system, the high cooling liquid level, and the insulated conductor, all prevent breakdown during the anodization process.

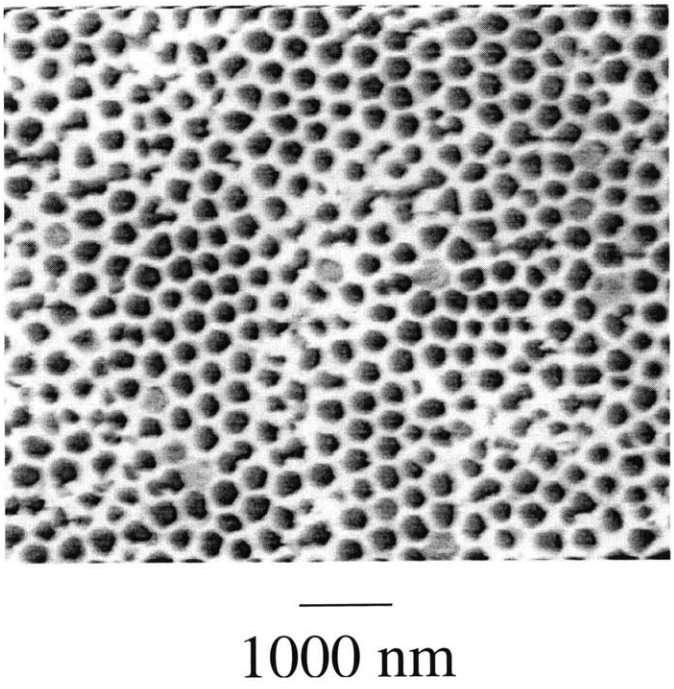

Figure 3-8: Scanning electron micrograph of anodic alumina template anodized at 160 V with pore diameters around 200 nm.

In our samples, in addition to the increase in current at breakdown, sizzling occurred at the air/acid interface where the aluminum was exposed to air. Furthermore, the onset of this sizzling phenomenon was correlated with the ambient air temperature. This suggests that the sizzling is caused by the higher temperature of the sample at the surface (surface heating). We therefore implemented four techniques to reduce surface heating and the likelihood of breakdown (see Fig. 3-7). When all four techniques are implemented, sizzling under our anodization conditions is eliminated. The first improvement was an automatic cooling system. A refrigerated recirculator is used to keep the cooling liquid at $-1.5 \pm 0.05\,^{\circ}\mathrm{C}$. In addition, the acid level is kept below that of the cooling liquid. This helps cool the air around the acid-air interface. Thirdly, the aluminum electrode is completely submerged in the chilled acid. In order to prevent shorting of the contact to the acid, an insulated conductor is used to make contact with the Al sheet inside the acid. Lastly, the back, unpolished side of the aluminum sheet is attached to a glass slide with paraffin so that only one side of the aluminum anodizes, thus keeping the current and the temperature stable. The aluminum is anodized using this method for about 3 hours. The alumina is then etched off and the remaining aluminum subsequently undergoes a second anodization for about 4 hours. The pores from a 160 V anodization are shown in Fig. 3-8 [4]. Researchers at the Max Planck Institute of Microstructure Physics also can reproducibly grow well-ordered anodic alumina at high voltages [49]. As in our procedure, key to their setup is cooling the sample and anodizing only the front side of the aluminum.

The measurements of $\sim 250nm$ diameter bismuth nanowires formed by filling the pores of alumina made by the ultra cool method of anodization are shown in section 5.2.2.

3.3 FILLING

After porous alumina templates are fabricated, the pores are then filled with bismuth. Many groups fill porous anodic alumina templates with metals, for example see references [53, 55–58]. However, only a few groups fill the templates with bis-

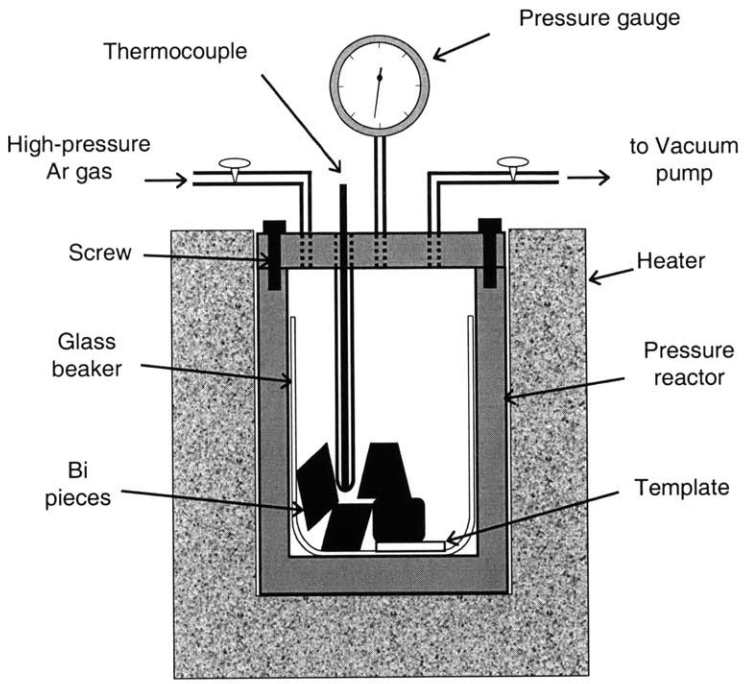

Figure 3-9: Schematic diagram of the pressure-injection method used in this research to fill the pores in the anodic alumina template with bismuth. The figure is from Dr. Zhibo Zhang.

muth [42, 45, 59]. Methods to fill the samples include electro-chemical deposition, vapor phase injection [60], and our liquid and pressure injection method [42]. Our bismuth nanowires are fabricated by filling porous alumina templates with molten bismuth under a high pressure atmosphere [42, 60]. Therefore, most of the reported results herein are from samples filled by the liquid pressure injection process, although shortly our group will be able to fill the pores in the alumina template with bismuth electro-chemically. A schematic of the process setup is shown in Fig. 3-9. For a review of other filling techniques as well as other nanowire fabrication methods see reference [61].

In the liquid-pressure injection technique, the alumina sample is clamped down to the bottom of a beaker and solid bismuth is placed on top. The beaker is then placed in a chamber and evacuated to $\sim 10^{-2}$ mbar at 250 $^{\circ}C$ for 8 hours, slightly below the 271.5 $^{\circ}C$ melting point of bismuth. This step degases the pores in the alumina. Next, the 99.9999% pure bismuth pieces are melted by heating the reaction chamber above the melting temperature of bismuth (271.5° C). The bismuth melts and covers the alumina template. The vacuum pump is then disconnected and high pressure Ar gas is pumped into the chamber until a pressure of $\sim$ 4500 psi is obtained. The chamber is left at this high pressure for 5 hours to ensure that the molten bismuth infiltrates into the pores of the alumina. The chamber is then slowly cooled to room temperature over a period of 12 hours, and the pressure is released. For more details on this process, see reference [42]. The bulk bismuth attached to the nanowire sample is removed with a wire saw and then by a mechanical polish. The samples are then annealed at 200° C for 8 hours.

Scanning electron micrographs of unfilled and filled alumina templates are shown in Fig. 3-10. The nanowires are $\sim$50nm in diameter. From the SEM pictures, we conclude that the sample is 16% air (or bismuth) and 84% alumina, and more than 90% of the pores are filled with bismuth [42].

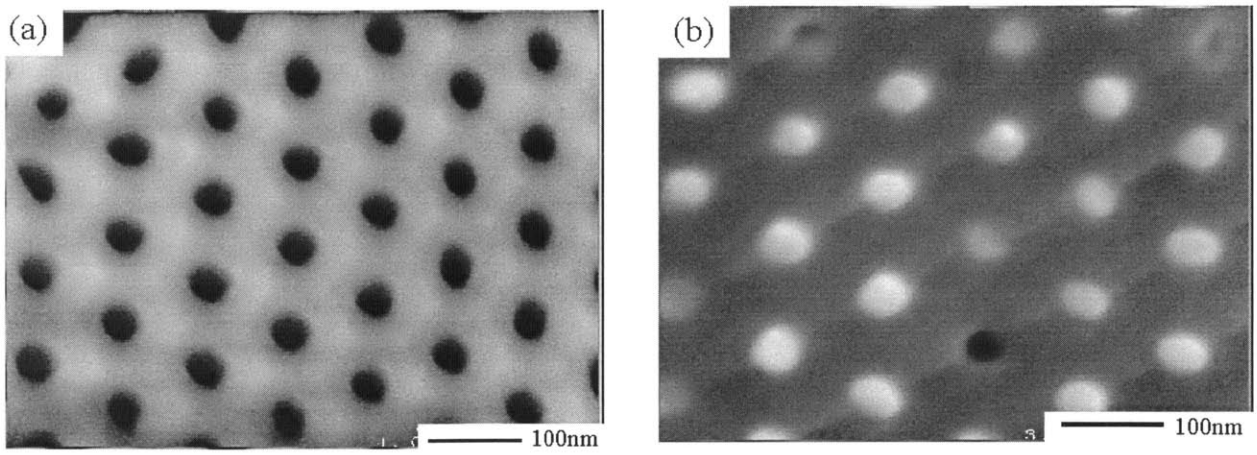

Figure 3-10: Scanning electron microscope picture of an unfilled (a) and filled (b) alumina template. The dark holes in the filled template (b) are pores that remain unfilled after pressure injection. The SEM image of the unfilled alumina (a) is taken of the top side of the alumina (furthest from the aluminum film), while the filled alumina (b) is taken from the bottom side of the alumina (nearest to the aluminum film).

3.4 MAKING FREE-STANDING WIRES

We formed free-standing bismuth nanowires by placing the bismuth and alumina composite into an acid to selectively etch the alumina. As with most small band gap materials, bismuth is not very stable in acid while bismuth oxide is very stable. Therefore, bismuth nanowires oxidize easily in acidic solutions. In addition, the chemical sensitivity of bismuth makes finding a selective etch for the alumina difficult. Two different acid solutions are employed in this thesis for removing the aluminum oxide. The first etch solution is $5\%H_3PO_4$ and $45g/lCrO_3$. The phosphoric acid reduces the alumina, but the chromic acid oxidizes the bismuth, so that this solution forms a continuous but non-uniform $\sim 7nm$ bismuth oxide coating over free-standing bismuth nanowires, see subsection 3.5.2. If the etch solution did not contain chromic acid, the bismuth nanowires would completely dissolve in the acid. The second solution is basic and consists of one mole of KOH to one mole of $NaOH$. This etch formed a more uniform, mostly continuous, slightly thinner bismuth oxide coating over the nanowires [62].

For optical applications, a continuous bismuth oxide is beneficial since it isolates the bismuth nanowires from each other. Since bismuth oxide is an insulator ($E_g \simeq$

eV [63]), bismuth oxide doesn't absorb in the IR from either free carrier or interband transitions. To confirm that bismuth oxide is transparent in the IR, two bismuth oxide samples were measured. Both a polished piece of bismuth, and a thin film of bismuth deposited onto a KBr window were annealed at $250 - 350°$ C for over 10 hours. The thin film of bismuth becomes completely oxidized. Neither the optical transmission of the thin bismuth oxide on KBr nor the optical reflection of the bismuth oxide on a polished bulk piece of bismuth showed any observable features in the energy range (600 to 4000 cm^{-1}) of our experiments.

For both etch solutions, a small ($\sim 1mm^2$) sample of bismuth nanowires inside an alumina template was placed into a container partially filled with an etch solution. Etching overnight is sufficient to remove the alumina. Any excess time in the acid increases the thickness of the oxide formed on the nanowire surfaces. The etch process was being developed at the same time as when most of the free-standing wire experiments reported in this thesis were performed. Therefore, many of the nanowires, whose optical properties are reported here, have a significant bismuth oxide coating surrounding them.

After the allotted time ($7 - 12$ hours), the free-standing wires clump together at the bottom of the jar. Using a pipette, the acid can be removed without removing the majority of the nanowires. While still in the jar, we rinse the nanowires with Isopropyl Alcohol (IPA) until the acid is completely removed. During the rinse, care must be taken to prevent the nanowires from separating and rinsing out as well. At the end of the final rinse, the last remaining drop of IPA and the bismuth nanowire clump is sucked into the pipette and dropped onto a KBr window. Once the IPA dries, only the bismuth nanowires remain on the KBr window. Acetone, and certainly water, should be avoided, since both destroy KBr windows. Occasionally, not all the alumina will be etched from the bismuth nanowires, as determined easily by FTIR. The bismuth nanowires can be etched again by removing the nanowires from the KBr window with IPA and placing them back into the etch solution. This process wasn't always successful, and often the KBr window was destroyed in the process and a second window had to be used.

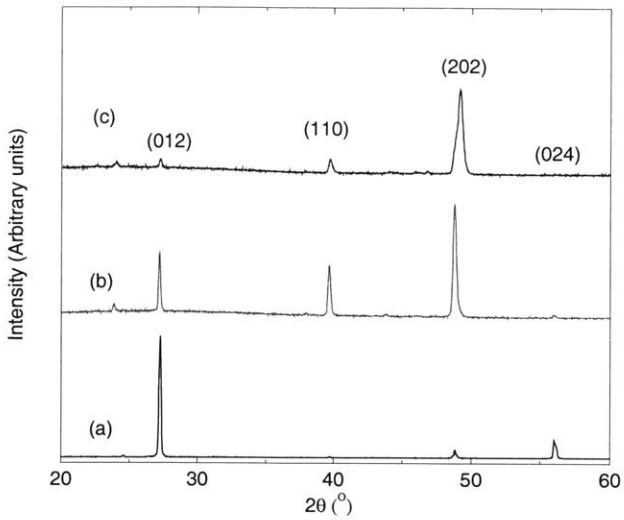

Figure 3-11: XRD patterns of bismuth filled alumina with average wire diameters of (a) 40 nm, (b) 52 nm, and (c) 95 nm. Marked above the individual peaks are Miller indices corresponding to the lattice planes of bulk Bi. The XRD peaks positions are the same as those of the polycrystalline Bi standard. Figure from YuMing Lin.

3.5 CHARACTERIZING THE BISMUTH NANOWIRES

In addition to the SEM and TEM images already presented, X-ray diffraction (XRD), and transmission electron microscopy (TEM) were used to characterize the bismuth nanowires.

3.5.1 XRD

A study on the crystallographic orientation of the bismuth nanowires was performed by Zhang[64]. In a later study by Lin, the nanowires used in this thesis were found to be preferentially aligned along the wire axis, with an orientation dependent on the nanowire diameter. Arrays of wires with a diameter larger than 50 nm, are preferentially aligned in the $< 101 >$ direction, while arrays of wires with a diameter smaller than 50 nm are preferentially aligned in the $\langle 012 \rangle$ direction [65]. The exact reason for this preferential alignment is not yet understood. Interestingly other methods of forming bismuth nanowires, such as the vapor injection method, grow nanowires with the

same crystallographic orientations, ⟨012⟩ for small diameter wires and ⟨101⟩ for larger diameter wires. For example, 200nm diameter bismuth nanowires formed inside anodic alumina using a vapor injection technique [60] are aligned in the ⟨101⟩ direction. Also, bismuth nanowires of 5 to 50nm diameter fabricated inside mica are aligned in the $< 012 >$ direction, the same direction as our smaller wires [66]. However, not all bismuth nanowires are found to be aligned in the ⟨012⟩ or ⟨101⟩ direction. For example, bismuth nanowires formed inside anodic alumina using a similar high pressure injection method as our method, except that higher pressures (1.5 Kbar vs. 0.3 Kbar) were used, formed wires aligned in the ⟨001⟩ direction [44]. Bismuth nanowires with wire diameters between 5 and 60nm formed by electro-chemically filling anodic alumina do not have a single dominant crystallographic alignment direction [67]. An example of XRD data from samples similar to those used in this thesis are shown in Fig. 3-11.

3.5.2 TEM

Dr. S. Cronin and Dr. P. Gai performed a thorough transmission electron microscope study on our bismuth nanowires [68]. Their TEM study provided us with some important information relevant to this thesis. They learned that bismuth nanowires are almost completely crystalline with very large crystalline regions (see Fig. 3-12). The crystalline regions are several microns along the wire direction and limited by the wire diameter in the other directions. The crystalline regions are usually aligned in the same direction (⟨012⟩ or ⟨101⟩), but maybe twisted along the wire axis relative to each other. The TEM study also revealed the pressure of an oxide coating on the bismuth nanowires after they had been removed from the alumina. This oxide was determined to be formed during the alumina etch. The oxide thickness was found to be 7nm for a chromic - phosphoric acid etch. An example of a TEM image is shown in Fig. 3-12. For more detailed information on making contact to a single bismuth nanowire through a bismuth oxide film see reference [69].

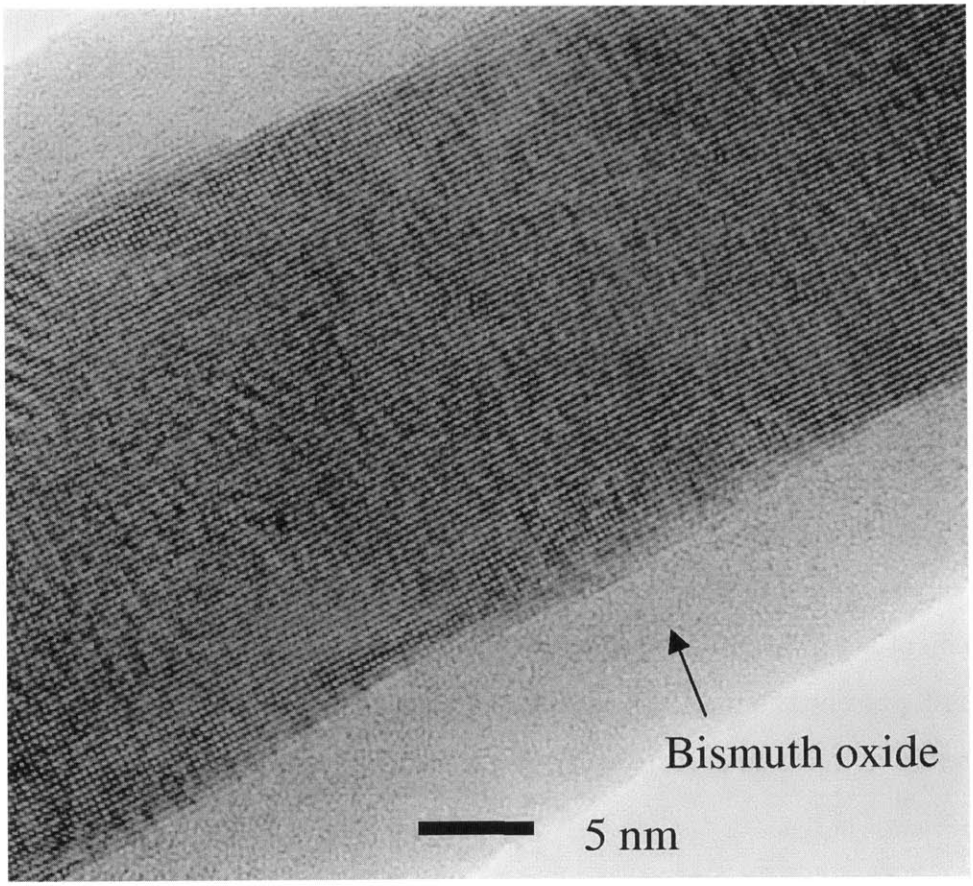

Figure 3-12: High resolution TEM of a bismuth nanowire. Figure from Dr. Steve Cronin.

Chapter 4

FINDING THE DIELECTRIC FUNCTION OF BISMUTH NANOWIRES

This chapter explains how the dielectric function of bismuth nanowires is deduced. In this thesis two types of samples are measured; those inside the alumina template and those where the alumina template has been etched away. Section 4.1 explains the measurement setup used to measure both of these types of nanowires, while sections 4.2 and 4.3 present the methods used for obtaining the dielectric function of bismuth nanowires in alumina and of free standing bismuth nanowires, respectively.

4.1 FTIR SETUP

Optical reflection, R(ω), and transmission, T(ω), spectra as a function of wavenumber were measured using a Nicolet Magna-IR 860 Fourier Transform infrared spectrometer and Nic-Plan IR Microscope. Data were taken in the infrared region from $600 < \nu < 4000$ cm^{-1} at 300K using a gold reference for reflection. A resolution of 2 cm^{-1} was used.

Figure 4-1 shows (a) a Fourier Transform Infrared Spectrometer (FTIR) as well as (b) a picture of the FTIR microscope stage at MIT's CMSE shared facility. Several

a)

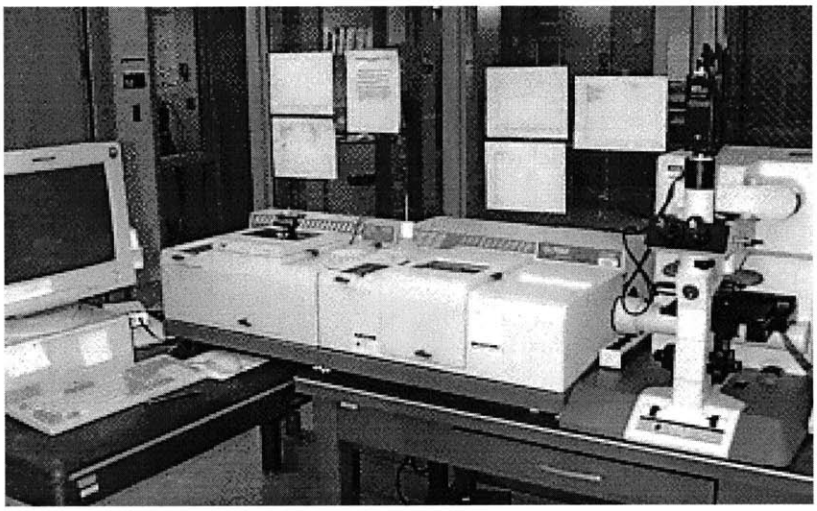

b)

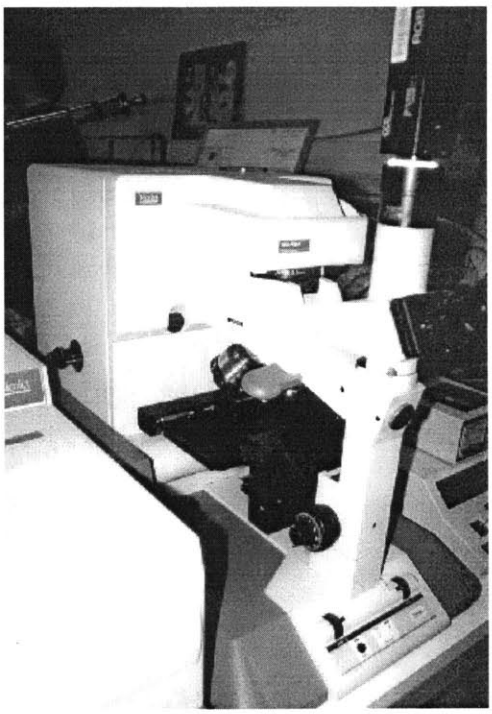

Figure 4-1: a) A Nicolet FTIR setup with a Nic-Plan microscope and a computer attached.
b) CMSE shared facility's microscope FTIR.

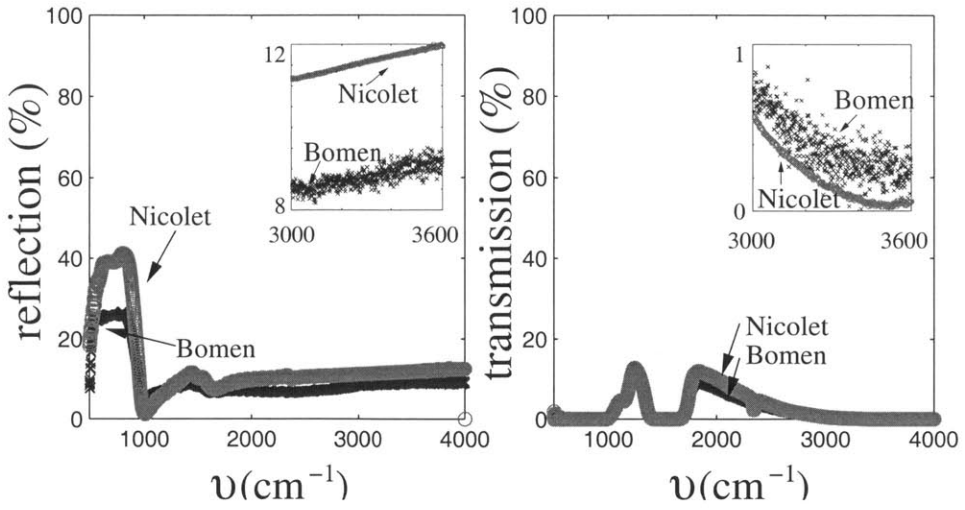

Figure 4-2: A comparison of the reflection and transmission data taken from two different experimental systems. The data on the Nicolet instrument were taken at MIT's CMSE and was obtained using the microscope accessory. The data taken with the Bomem instrument were taken at Prof. Eklund's laboratory in the University of Kentucky. The spectra are similar but some differences are observed that may be accounted for by differences in temperature, humidity, and pressure.

limitations of the experimental setup are of importance to our measurements. Firstly, although the light incident onto the sample is mostly normal to the sample plane, some of the light does hit the sample at an angle. Nicolet reports that the angle varies from $0 - 40°$. The second limitation of our experimental setup is inherent in an FTIR instrument. Light of many energies are incident onto the sample surface at the same time. Hence, FTIR measurements can not distinguish between transmission/reflection at a particular energy and photo luminescence at that energy induced by a photon of a higher energy. In order to measure luminescence, monochromatic light, and thus a monochromator, should be used. See section 6.2.

To ensure that the optical reflection $R(\mathrm{cm}^{-1})$ and transmission $T(\mathrm{cm}^{-1})$ are accurate, the measurements taken on MIT's Nicolet FTIR were compared to spectra taken on a Bomem FTIR spectrometer (model number DA3) at the University of Kentucky. Both sets of data are taken in the same infrared region, $600 < \nu < 4000\,\mathrm{cm}^{-1}$, and at room temperature. The wavenumber resolution chosen for the data taken on the Bomem spectrometer is $1\,\mathrm{cm}^{-1}$. The reflection and transmission spectra from the

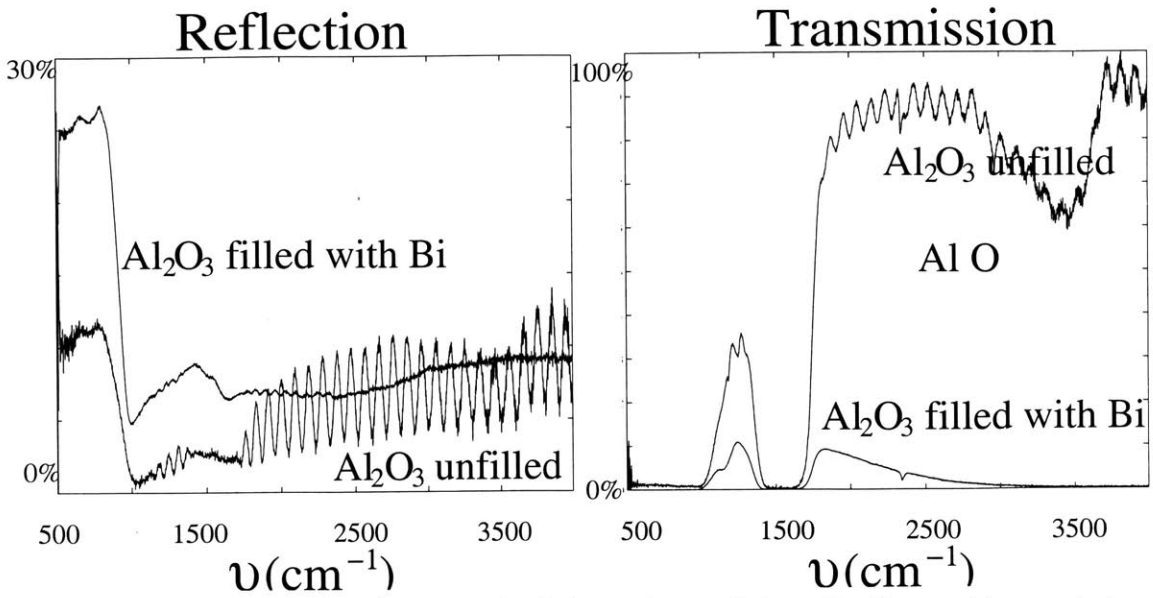

Figure 4-3: Photon energy (wavenumber) dependence of the reflection and transmission of porous alumina and porous alumina filled with Bi nanowires: Both the transmission and reflection data show a large interference pattern in the range 2000 - 4000 cm^{-1} only for the unfilled sample. The absence of interference patterns in the Bi filled templates indicates an increase in absorption with the addition of Bi. Also indicating an increase in absorption, the transmission through the sample is decreased with the addition of Bi. The larger reflection in the filled samples is the result of an increase in the index of refraction with the addition of Bi.

two FTIR systems agreed well, see Fig. 4-2, demonstrating that either systems can be used for this analysis.

The two systems have different advantages. The Bomem system at the University of Kentucky can measure the reflectivity and transmission at smaller wavenumbers, while the Nicolet system at MIT has less noise (See the insert Fig. 4-2). In addition, the Nicolet microscope setup enables the measurement of samples as small as $\sim 1mm^2$ with relative ease.

4.2 NANOWIRES INSIDE ANODIC ALUMINA

4.2.1 REFLECTION AND TRANSMISSION MEASUREMENTS

Examples of reflection and transmission spectra of unfilled and bismuth filled alumina templates are shown in Fig. 4-3. Both the transmission and reflection data of the unfilled template show large interference patterns for wavenumbers in the range of $2000 < \nu < 4000\text{cm}^{-1}$ indicating a low absorption for this energy (wavenumber) range. The absence of interference patterns in the transmission and reflection spectra of the bismuth filled template is the result of an increase in absorption with the addition of Bi. Also indicating an increase in absorption, the transmission through the sample decreases with the addition of Bi. Furthermore, the higher reflection in the bismuth filled sample, predominantly for $\nu < 1000\ \text{cm}^{-1}$, results from a larger absorption coefficient and index of refraction in this sample.

Unfortunately, anodic alumina has optical features in the energy range of our experiments. For example, the amorphous anodic alumina template material absorbs light with wavenumbers less than $900\ \text{cm}^{-1}$, an absorption inherent to alumina and present in sapphire (crystalline alumina) as well. The effect of the alumina on the reflection and transmission, therefore, cannot be ignored.

4.2.2 FINDING ϵ_1 AND ϵ_2 FROM R AND T

After the reflection and transmission of bismuth alumina composites are measured, the frequency dependent dielectric function, $\epsilon_1 + i\epsilon_2$ of the composite samples can be extracted. Depending on the magnitude of the transmission and reflection, one of three methods can be used to find the dielectric function as a function of photon energy. The first method makes use of the Kramers-Kronig relations and is valid when the transmission is negligible, and the sample thickness is assumed to be infinite. This assumption is good for materials in which the absorption coefficient times the sample thickness is large (> 1). The Kramers-Kronig relationship used in this work relates

the measured reflection, R, to the phase of the reflected light, θ, according to:

$$\theta(\omega') = -\frac{\omega}{\pi}\int_0^\infty \frac{logR(\omega) - logR(\omega')}{\omega^2 - \omega'^2}d\omega. \tag{4.1}$$

The reflection coefficient, r, is defined as the ratio of the reflected to the incident light, and is related to the measured reflection intensity, R, and the angle, θ, by the relation

$$r(\omega) = \sqrt{R(\omega)}e^{i\theta(\omega)t}. \tag{4.2}$$

Since the integral in Equ. 4.1 is for frequencies from $\omega = 0$ to $\omega = \infty$, the reflection is extrapolated beyond the measured spectra, 200 cm^{-1} below 650 cm^{-1} and 200 cm^{-1} above 4000 cm^{-1}. The resulting dielectric function varied only slightly depending on how the reflection coefficient was extrapolated, as long as it didn't decay to 0 too quickly. A constant R, an R that linearly goes to 0, and an R that exponentially decayed to 0 were all tried. Since Maxwell method described below accurately determines the dielectric constant for parts of the spectra, these results were compared to the Kramers-Kronig results from each of the three different methods for extrapolating R. The best fit with the values obtained from the Maxwell method was found for an R that remained constant from $400-600$ cm^{-1} and from $4000-4200$ cm^{-1}, consistent with preliminary measurements in the far IR which showed a relatively flat reflection for bismuth nanowires for energies slightly below 600 cm^{-1}.

Once the phase of the reflection is determined from Equ. 4.1, the real and imaginary parts of the index of refraction can be found by relating r to the complex index of refraction, n.

$$r(\omega) = \frac{n(\omega) - 1}{n(\omega) + 1} \tag{4.3}$$

Relating Equ. 4.3 to Equ. 4.2 and using the relation between the index of refraction and the dielectric constant, Equ. 2.30, the real and imaginary parts of the dielectric function as a function of ω can be obtained.

The second method that can be used to determine the dielectric function from

reflection and transmission data is using the interference pattern in the data. In this region, both the transmission and reflection are of equal magnitude; in other words, the absorption coefficient times the sample thickness is small (< 1). If the sample thickness is known, the real part of the dielectric function can be found very accurately. Usually in this regime, the absorption coefficient and the imaginary part of the dielectric function are assumed to be zero. This method is not employed for the bismuth nanowire samples since their thicknesses are not accurately determined, and since there is significant absorption even in the unfilled alumina samples.

When a material has both a measurable transmission and reflection and the interference pattern is small, a third method can be used to find its dielectric function. In this case Maxwell's equations are solved for a sample of finite thickness. The real and imaginary parts of the dielectric function are varied and the reflection and transmission are simulated. In this method the sample thickness must be known, but the results are much less dependent on thickness than for the interference pattern method.

In the bismuth nanowire samples, the dielectric function ($\epsilon_1 + i\epsilon_2$) was calculated from the reflection and transmission data by solving Maxwell's equations with appropriate boundary conditions for each of the two sample - air interfaces. Possible ϵ_1 values were tried at increments of 0.05. For each value of ϵ_1, values of ϵ_2 were tried with a step size of 0.01. For each measured frequency from 600 to 4000 cm^{-1} with a transmission and reflection above the measurement limits of the FTIR instrument, the combination of ϵ_1 and ϵ_2 yielding the minimum error was found.

$$Error = (R_{\text{calculated}} - R_{\text{measured}})^2 + (T_{\text{calculated}} - T_{\text{measured}})^2 \tag{4.4}$$

For regions where $\epsilon_2 < 0.01$, the transmission is almost 100% and the reflection is small. Since this method of appling Maxwell's equation to find the dielectric function of a sample requires measurable reflection and transmission values, it is not usable for photon energies where the transmission was below the limits of the spectrometer.

In our samples, either the Kramers-Kronig method or the Maxwell method can

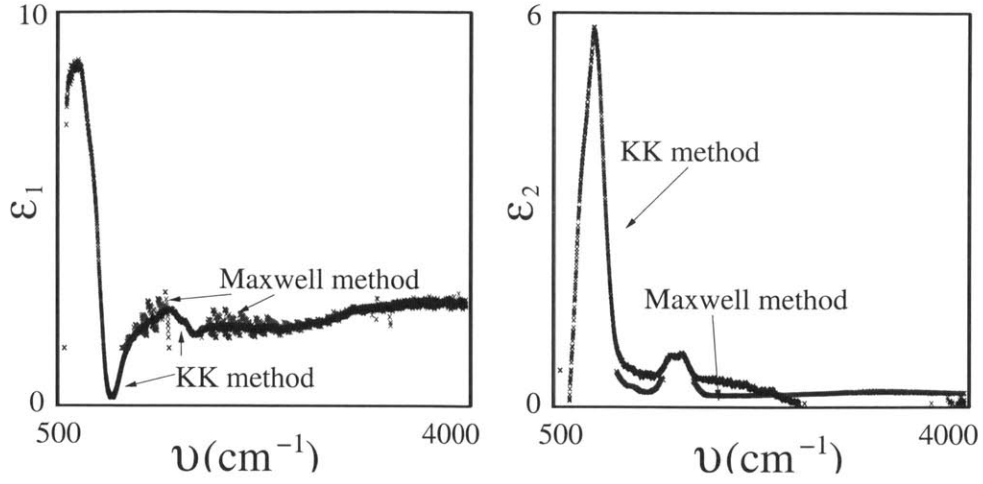

Figure 4-4: A comparison of the dielectric function obtained from two methods: the first from frequency dependent reflection data using the Kramers-Kronig relations, and the other method which involves solving Maxwell's equations and then optimizing the fit between the frequency dependent reflection and transmission data.

be used to find the dielectric function. Since the Kramers-Kronig relations are only accurate when the transmission is negligible, and since our samples have 10% transmission at some wavenumbers (See Fig. 4-2 B.), we had to ensure that this method for determining $\epsilon_1(cm^{-1}) + i\epsilon_2(cm^{-1})$ was accurate enough. In figure 4-4, we show the dielectric function found by solving Maxwell's equations, for ν where the transmission and the reflection are measurable. The dielectric function calculated by the Kramers-Kronig relations is also shown for comparison. The analysis in Fig. 4-4 shows that the above two methods agree well. The Kramers-Kronig method is more accurate when the absorption is high and the transmission is small, and the Maxwell method is accurate if the thickness is known precisely and both the reflection and transmission are accurately measurable. Since the transmission is small, but measurable for most of the wavenumber range we are interested in, either method can be used, although neither method is perfect. We therefore decided to use the Kramers-Kronig method to obtain the dielectric function of our bismuth filled samples and the Maxwell method for obtaining the dielectric function of the unfilled alumina samples.

4.2.3 REVERSE EFFECTIVE MEDIUM THEORY (REMT)

Our calculations show that significant quantum confinement requires that the Bi nanowires be 50 nm or less in diameter, at room temperature. For the wires used in this study, the first intersubband, interband, and indirect interband transitions are expected to occur in the mid-IR. Therefore we are interested in an energy region where the wavelength of light (λ) is much larger than the diameter of the nanowires (d_w): $\lambda >> d_w$. Therefore, one oscillation of the electric field in real space crosses over many alumina / Bi boundaries. Since a single wavelength of the electric field sees an array of Bi wires in an alumina host, the dielectric function of a sample contains information about both the alumina template and the bismuth nanowires. In addition, the shape of the nanowires can modify the optical properties as described by reference [25]. Here we use an effective medium theory (EMT) in reverse to obtain the dielectric function of the Bi nanowires inside the alumina when the dielectric function of the composite material is known [70]. We refer to this method as reverse effective medium theory (REMT).

Many prior studies have developed an EMT for predicting the dielectric function of a composite material when the dielectric function of both the constituent materials are known [6, 25, 26, 71]. These theories have been applied to many different composite materials [22, 23, 57, 58, 72–77]. When a sample is composed of more than one material, with the size of the constituents smaller than the wavelength (λ) of the optical fields, an effective medium theory models this inhomogeneous material as a single material with a single dielectric function. In the present study we utilize the Maxwell-Garnet (M-G) EMT [25, 26], which is valid for nanoparticles smaller than λ inside a dielectric material. We chose the M-G EMT, since it agrees with an exact calculation for the case of cylindrical pores in alumina [28]. The M-G EMT relates the dielectric function of the composite material to that of the guest material (bismuth or air) and host material (alumina) by:

$$\frac{\epsilon_{\text{composite}} - \epsilon_{\text{host}}}{\epsilon_{\text{composite}} + \kappa * \epsilon_{\text{host}}} = f \frac{\epsilon_{\text{guest}} - \epsilon_{\text{host}}}{\epsilon_{\text{guest}} + \kappa * \epsilon_{\text{host}}} \tag{4.5}$$

where f is the percentage of the total volume occupied by the guest material in the composite (the "filling factor"). For bismuth nanowires f is the percentage of either Bi or air inside the porous alumina template, and is found to be 0.16 by scanning electron microscopy, (See Fig. 3-10). Here, κ is the screening parameter, and for infinitesimally small nanowires, $\kappa = 1$. The MG-EMT then equals the exact equation [28].

Once the dielectric function results for the composite are obtained, the dielectric function of the alumina is found by substituting the values of the dielectric function of the unfilled alumina, a filling factor of 0.16, and the dielectric constant of air (1) into Equ. 4.5. Likewise, by substituting into Equ. 4.5 the previously deduced dielectric function of alumina, a filling factor of 0.16, and the dielectric function of the filled alumina template, the dielectric function $\epsilon_1 + i\epsilon_2$ for the Bi nanowires was obtained for the wavenumber range $600 - 4000$ cm^{-1}. From Equ. 4.5, the dielectric function of the nanowires is described by the equation

$$\epsilon_{\text{guest}} = \epsilon_{\text{host}} \frac{\kappa\epsilon_{\text{composite}} - \kappa\epsilon_{\text{host}} + f\epsilon_{\text{composite}} + f\kappa\epsilon_{\text{host}}}{-\epsilon_{\text{composite}} + \epsilon_{\text{host}} + f\kappa\epsilon_{\text{host}} + f\epsilon_{\text{composite}}}. \tag{4.6}$$

The dielectric function of bismuth nanowires inside an alumina template presented in this thesis are deduced by applying Equ. 4.6 to the measured dielectric function of Bi-filled and unfilled alumina templates.

4.3 FREE STANDING WIRES

Although REMT gives reasonable results, one should keep in mind that it is an indirect method for obtaining the dielectric function of bismuth nanowires. Furthermore, the alumina templates absorb for part of the measured spectra, possibly leading to inaccurate values of the absorption for this energy range. Figure 4-5 shows the transmission of an unfilled alumina template (b), a bismuth filled alumina template (c), and a free-standing bismuth nanowire sample (a). Some of the features in the free-standing wires are for wavenumbers (ν) less than 1000 cm^{-1}, where the transmission through the alumina is small. Therefore, the optical spectra of bismuth nanowires

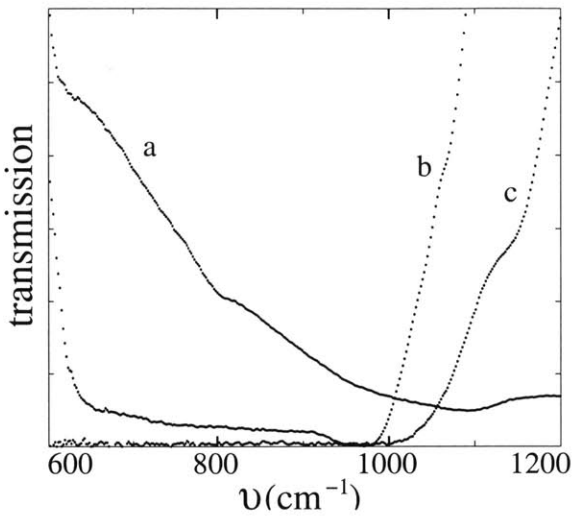

Figure 4-5: Transmission data for: (a) free-standing Bi nanowires, (b) an unfilled alumina template, and (c) a Bi filled alumina template.

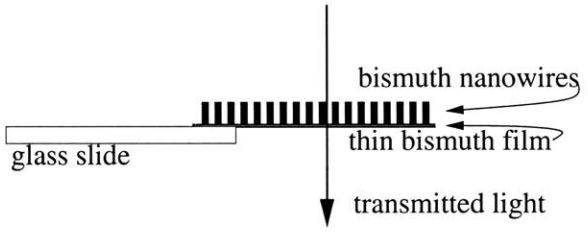

Figure 4-6: A schematic diagram of a free-standing bismuth nanowire array mounted on a glass slide.

inside alumina will at best only weakly show these optical features. Therefore, in addition to measuring bismuth nanowires inside alumina, the optical absorption of free-standing bismuth nanowires is also studied.

The free-standing wires are formed by the process described in section 3.4. Using the microscope FTIR, the reflection and transmission were measured from a sample containing free-standing Bi nanowires, a bismuth oxide coating over the nanowires, and a thin Bi film holding the nanowires together. A thin piece of bismuth with nanowires protruding like blades of grass is balanced on the edge of a glass slide, as shown in Fig. 4-6, or placed on a potassium bromide (KBr) window, while light is transmitted through the sample.

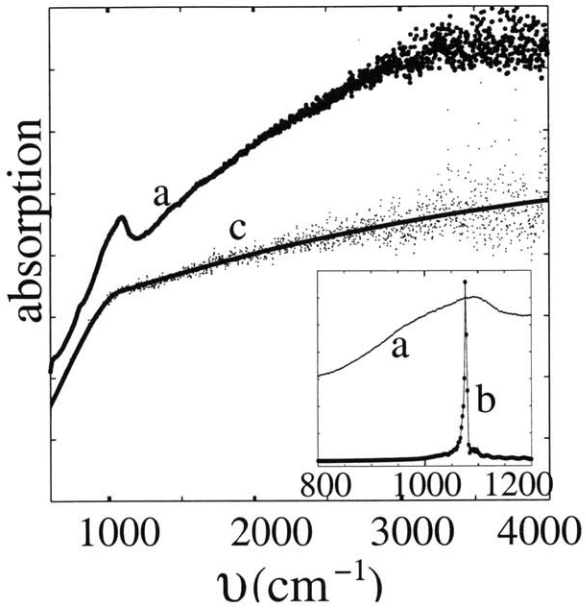

Figure 4-7: The wavenumber (ν) dependence of the absorption coefficient found by taking the negative log of the transmission of free-standing bismuth nanowires (a), as well as the absorption of a thin piece of bismuth (points) and the fit to this absorption (line curve) (c). The insert compares the absorption of the free-standing wires (a), with the absorption [Im $(\epsilon_1 + i\epsilon_2)^{1/2}$] of bismuth nanowires inside an alumina template (b) as obtained by reverse EMT. The main absorption peaks of the two samples occur at about the same ν value.

Since the transmission is proportional to $e^{-\alpha d}$, where α is the absorption coefficient and d is the sample thickness, the negative log of the transmission is proportional to the absorption coefficient. Only the bismuth contributes to the measured optical absorption since bismuth oxide is non-absorbing in this energy range. Note: the non-unity index of refraction of bismuth oxide will slightly change the reflection and hence the transmission of the bismuth nanowires, but will not change the location or the shape of the absorption peaks.

The absorption coefficient (α) times the sample thickness d as a function of wavenumber of the free-standing bismuth nanowires (a), is shown in Fig. 4-7. For comparison, Fig. 4-7 also shows the absorption from $\sim 40\,\text{nm}$ Bi nanowires inside an alumina template curve (c) obtained by using the reverse EMT analysis [70]. The wires used for the free-standing nanowire measurements had a diameter of 60 nm before the alumina template surrounding the wires was etched away. Since a $\sim 7\,\text{nm}$

oxide grows on the free-standing wires after the alumina is selectively etched away [78] (see section 3.4), the inner bismuth portion of the free-standing wires is expected to have a diameter of around 45 nm. The two nanowire arrays are therefore of comparable wire diameters. The results of figure 4-7 also include the absorption spectrum of a thin film of bismuth (c) which is used to provide the background spectra later used in Fig.4-9 and in fitting the absorption spectra to simulations of intersubband absorption (See section 5.3.2). The thickness of the template is poorly determined, and therefore the absolute magnitude of the absorption cannot be obtained quantitatively, and arbitrary units for the absorption are consequently used.

The free-standing Bi nanowires absorb strongly at $\sim$1050 cm^{-1} (curve (a) in Fig. 4-7), in agreement with the peak absorption energy (wavenumber) of Bi wires in the alumina template obtained by the reverse EMT approach (curve (b) in the insert to Fig. 4-7). The agreement in the position of the absorption peak found by these two methods validates the use of the reverse EMT approach for measuring large absorption peaks at wavelengths larger than the feature size of the sample. However, the absorption peak is much sharper for the Bi nanowires embedded in the alumina template, which absorb only from 1000 to 1100 cm^{-1}, than the peak for the free-standing wires, which extends from about 950 to 1150 cm^{-1}. The difference in the absorption peak widths may have several explanations. The difference might indicate limitations of the reverse effective medium theory, since the accuracy of the reverse effective medium theory depends on the magnitude of the imaginary part of the dielectric function of the host material. By comparing the transmission spectra of the filled and unfilled alumina templates as shown in Fig. 4-5, we know that the absorption in alumina is large for wavenumbers less than 1000 cm^{-1}. We thus expect a decrease in the accuracy of the absorption obtained by reverse effective medium theory for wavenumbers less than 1000 cm^{-1}. The difference in absorption peak widths could also result from the wire diameter distribution widening and from inhomogeneities in the nanowire diameter along the length of each wire and among the various wires. This imhomogeneity in diameter increases during the Bi oxide growth after the removal of the wires from the alumina template.

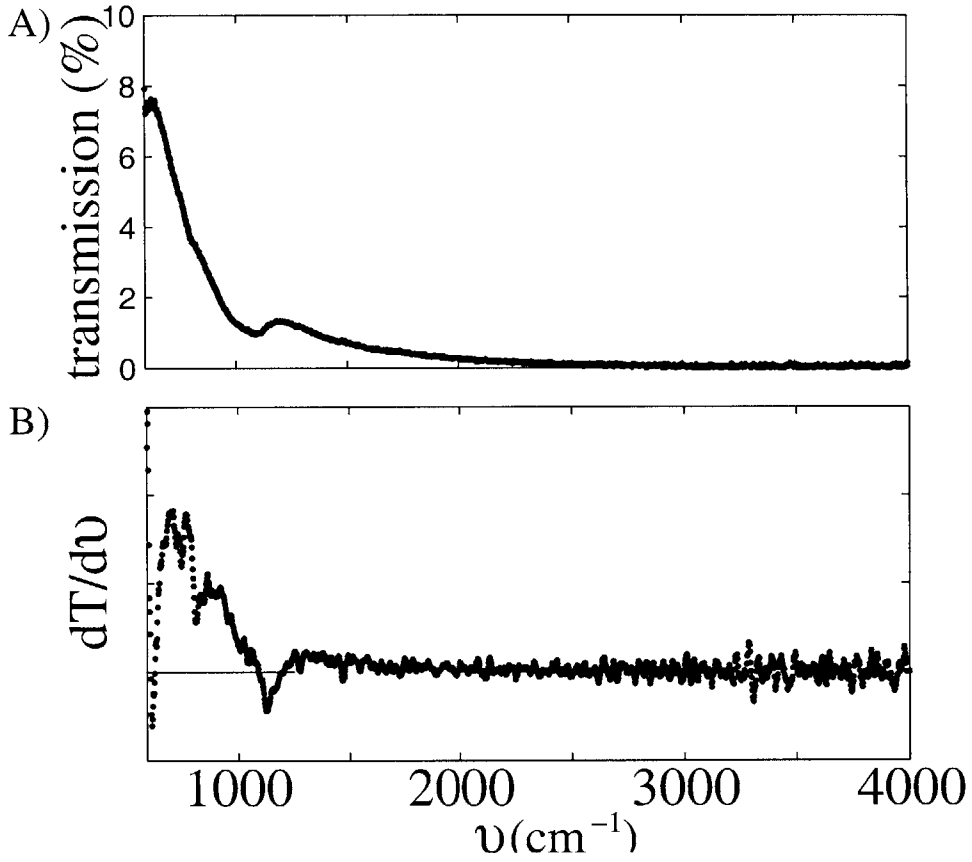

Figure 4-8: A) The transmission as a function of wavenumber of free-standing bismuth nanowires. B) The derivative of the transmission ($dT/d\nu$) as a function of wavenumber.

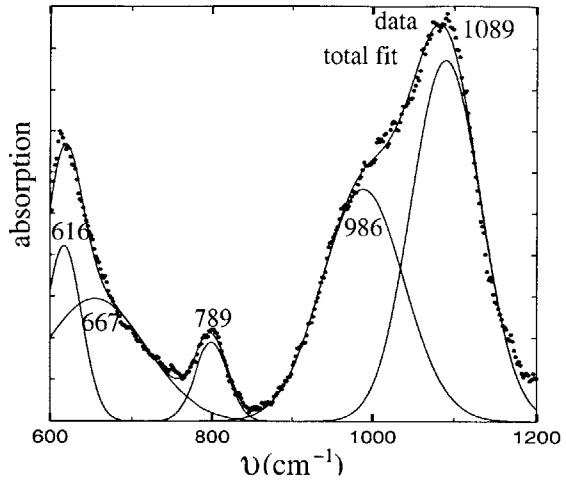

Figure 4-9: Fit of Gaussian peaks to the absorption spectrum in the free-standing Bi nanowire sample. Five broad peaks are observed at 616, 667, 798, 986, and 1090 cm^{-1}. The absorption from the thin bismuth sample is used as the baseline and the absorption due to all 5 peaks is shown as the "total fit" to the data points. This spectrum is discussed further in section 5.3.2.

In addition to the large absorption peak at ~1050 cm^{-1}, smaller absorption peaks are observed at ~616, ~667, ~798, and ~986 cm^{-1} in the free-standing Bi nanowires. The smaller peaks can be more easily identified by looking at the wavenumber derivative of the transmission as a function of wavenumber, Fig. 4-8, or by looking at the fit of the absorption spectra to Gaussian peaks with using the absorption of the thin bismuth film as the background spectra, Fig. 4-9. These smaller peaks are not seen for the nanowires embedded inside alumina. Even though the experiment using alumina/Bi nanowire template samples and the reverse EMT allows us to determine the optical properties of aligned and non-oxidized bismuth nanowires, the alumina template masks the smaller peaks observed in the free-standing wire experiment. We therefore chose to use the data obtained from free-standing wires when the shape of the absorption peak is important, for example in comparing experimental and simulated absorption curves. Likewise, we use data obtained from nanowires inside the template when the alignment or uniform wire diameters are important, for example in the polarization and wire diameter dependence studies.

Chapter 5

IDENTIFYING THE ABSORPTION MECHANISMS

This chapter explains how, the background from chapter 2, the samples, whose fabrication is described in chapter 3, and the methods to find the dielectric function of bismuth nanowires, described in chapter 4 are used to identify the absorption mechanisms of bismuth nanowires. Section 5.1 explores how we expect different absorption mechanisms to contribute to the optical absorption in the mid IR. Section 5.2 presents experimental results which help to determine the dominant absorption mechanisms in our energy range. Section 5.3 complements the experimental results with theoretical simulations of different possible contributions to the absorption spectra. Section 5.4 combines the experimental and theoretical results to determine the dominant optical absorption mechanisms in bismuth nanowires in the mid-IR spectral range.

5.1 OVERVIEW

In bismuth nanowires many mechanisms are expected to contribute to the optical absorption within the same energy range. Therefore, interpretation of the absorption spectra of bismuth requires careful consideration of the possible absorption mechanisms and a thorough examination of the experimental data.

One of the most commonly investigated absorption mechanisms is direct interband

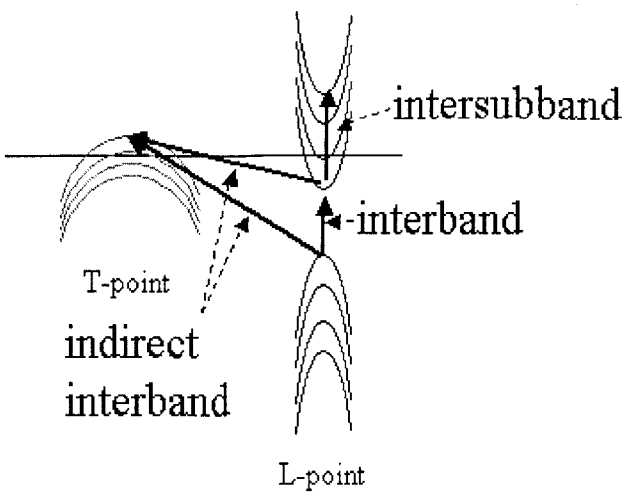

Figure 5-1: The L and T point bands and subbands in bismuth nanowires, and the possible types of band-to-band electronic transitions.

electronic transitions. In this scenario, a photon transfers its energy to an electron, thus exciting it from the valence band to an empty state in the conduction band. For intrinsic semiconductors, ignoring excitonic effects, the threshold for optical absorption from a direct interband transition is equal to the band gap. The direct (L-point) band gap of bulk bismuth is 290 cm^{-1} (36 meV) [1] at room temperature and 110 cm^{-1} (13.6mev) at $T < 5K$ [9, 79]. In bulk bismuth, optical absorption near 290 cm^{-1} at room temperature could result from a direct interband transition. However this absorption is bulk bismuth is mostly quenched since both the final and initial states are partially filled, see below.

Likewise, indirect interband transitions require a photon to transfer its energy to an electron which is then excited into a higher state. However, for indirect transitions, the creation or destruction of a phonon provides the momentum needed for the electronic transition. The optical absorption resulting from an indirect interband transition is expected to occur near the energy of the indirect bandgap. For several reasons, the exact energy of the transition will be slightly different than the energy of the indirect bandgap. For example, although small, ($\sim$ 100 cm^{-1} in bismuth [9]), the phonon energy will shift the energy of the absorption peak away from the indirect bandgap. In addition, the joint density of states has a singularity at an energy

slightly different from the indirect bandgap. Furthermore, if the Fermi energy is near either the initial or final electronic bands, the optical absorption peak maybe at an energy slightly different from the indirect interband transition energy. While all these effects need to be considered when calculating the exact energy of an indirect transition, a good estimate of the energy of the indirect interband transition is the indirect bandgap energy itself.

Bulk bismuth has two indirect L-T point transitions. The first is from the T-point valence band to the L-point conduction band. This transition occurs down to energies approaching zero, since these two bands overlap; see Fig. 5-1. The majority of optical absorption resulting from an electronic transition from the T-point valence band to the L-point conduction band will occur well below the experimental measurement range of $600 - 4000\ \mathrm{cm}^{-1}$. This absorption mechanism, therefore, will not significantly contribute to our measured absorption spectra.

The second indirect interband transition in bismuth nanowires is from the L-point valence band to the T-point valence band. The electronic energy of this transition is $742\mathrm{cm}^{-1}$ (92meV) at room temperature and $161\ \mathrm{cm}^{-1}$ ($\sim$20meV) at low temperatures ($< 77K$) for bulk bismuth. Since the energy of this transition, at room temperature, is in the energy range of the experiments, it must be considered as a possible absorption mechanism. Since the T-point valence band to the L-point conduction band indirect interband transition is a not major contributor to the measured absorption spectra, while the L-point valence band to the T-point valence band indirect interband transition may contribute to the measured spectra, the T-point valence band to L-point valence band transition will be referred to as simply the "indirect (L-T-point)" transition.

When bismuth is quantum-confined, as in our wires, quantum confinement increases the direct (L-point) bandgap and both of the indirect (L-T-point) bandgaps. We would therefore expect that the energy of the optical absorption resulting from all of these electronic transitions would increase when bismuth is formed as a nanowire, and to further increase as the wire diameter is decreased. For example, for undoped 40 nm diameter bismuth wires at 293 K, the lowest energy of a direct interband tran-

sition is calculated to occur at 800 cm^{-1} (99meV) at room temperature. In this case, ignoring for now the phonon energies, the indirect (L-T-point) transition from the first subband at the L-point valence band to the first subband at the T-point valence band is calculated to occur at 1690cm^{-1} (210 meV), while the first subband at the L-point valence band to the Fermi energy occurs at 1014 cm^{-1} (126 meV).

Another commonly studied absorption mechanism is absorption from free carriers. As the free carriers oscillate in response to the optical electric field, they dissipate energy. A large absorption peak is observed at the free carrier plasmon frequency. In bulk bismuth the free carrier plasmon frequencies is 333 cm^{-1} (41.3 meV) at room temperature, and the plasmon frequency decreases as the temperature is decreased [80]. While the low dielectric constant of alumina increases the plasma frequency, the reduced carrier concentration of quantum-confined bismuth decreases the plasma frequency. As the wire diameter decreases, the bandgap increases and thus the carrier concentration decreases. Although the energy of the free carrier plasmon is below the measurement range of our experiments for undoped samples, the tellurium-doped samples have an increased carrier concentration and hence an increased free carrier plasmon energy. Free carrier absorption is therefore briefly discussed is section 5.3.1.

Often in the mid IR range, phonons can be observed. However, since the phonon energy scales as $1/M$ where M is the mass of the atom, and bismuth is a heavy atom (atomic mass = 209), the optical phonons occur in bismuth at 75 and 100 cm^{-1} [9]. The phonon frequencies are therefore below the measurement range of our experiment. Furthermore, since the phonons in bismuth are symmetric, they likely couple only weakly to IR radiation.

An absorption mechanism unique to low dimensional materials in an electronic excitation from a low energy subband to a high energy subband for the same bulk energy band. This intersubband transition should decrease in energy as the wire diameter is increased. For wire sizes where quantum confinement is not significant, the energy of this absorption should approach zero. Even in structures with significant quantum confinement, this absorption mechanism is usually weak, since the lowest (highest) subbands in the conduction (valence) band are often empty (filled), leaving

very few electrons (holes) to be excited to higher (lower) states. However, in bismuth nanowires, the lowest subband states in the L-point conduction band are filled (at 293K the Fermi energy is at or above the band-edge of the lowest subband for wires with a diameter larger than 44nm), thus, leaving the possibility of significant absorption from intersubband transitions in bismuth nanowires.

Since our measurements are made in the frequency range of $600\,\mathrm{cm}^{-1}$ to $4000\,\mathrm{cm}^{-1}$, we may observe allowed direct transitions and indirect interband transitions and some intersubband transitions, but not the free carrier plasmon (for undoped samples) or phonon absorption in our nanowires.

The intensities of interband (and intersubband) absorption processes depend on both the joint density of states and on the number of electrons in the final and initial states. In a material that is quantum-confined in two dimensions (quantum wires), the electronic joint density of states has singularities at energies corresponding to each indirect, direct, and intersubband transition. Thus, if the transition is allowed, incident light at this energy may be strongly absorbed. When the initial and final states of an electronic transition track each other, many electronic states contribute to the optical absorption at similar energies, and therefore absorption resulting from bands that track each other is expected to be larger and sharper than for those transitions that do not track each other. In bismuth the initial and final states of an indirect L-T point valence band transition and those of intersubband transitions roughly track each other, while those of a direct interband L-point transition and those of an indirect L-point conduction band to T-point valence band transition do not.

The absorption is most intense when the initial state is filled with electrons and the final state is empty of electrons. In undoped bismuth, the Fermi energy crosses the T-point valence band and the L-point conduction band, see Fig. 5-1. Thus the direct interband transitions from the first few subbands have both the initial and final states partially filled. This is also true for bulk bismuth at both room temperature and at $77K$. The absorption from these transitions are therefore weak. The crossing of the Fermi energy through the L-point should make the intersubband transitions

stronger since the lower states are occupied and the higher energy states are mostly empty. The crossing of the Fermi energy through the T-point carrier pocket implies that the T-point valence band is empty at the band edge. Therefore the L-T indirect transition has both partially empty final states and mostly filled initial states. When the diameter of the bismuth nanowires is decreased, the L-point conduction band moves up in energy, while the T-point hole band moves down in energy. Eventually the L-point conduction band edge moves above the Fermi energy and the T-point valence band moves below the Fermi energy. Theoretical calculations predict that at 293K(77K) the L-point conduction band is above the Fermi energy when the diameter is $< 44nm (< 53nm)$ while the T-point valence band is below the Fermi energy when the wire diameter is $< 14nm (< 45nm)$. When the Fermi energy is below the L-point conduction band edge, the optical absorption from intersubband transitions should decrease, and those from interband transitions should increase. Likewise, when the Fermi energy is above the T-point hole band, the intensity of the indirect L-T valence band transition should decrease. This transition at room temperature, however, is not at all discrete and the transitions only slowly change as the Fermi energy varies. The wire diameters at which the L-point conduction band is above the Fermi energy and that at which the T-point valence band is below the Fermi energy are near the wire diameter at which bismuth makes a transition from a semi-metal to a semi-conductor (16 nm at room temperature). As can be seen from the above discussion, studying the energy, intensity, and line width of the absorption peaks as a function of wire diameter is key to understanding which absorption mechanisms are important under specific situations.

Separating the effect of different absorption mechanisms from each other is difficult, and, therefore, requires an extensive experimental study and theoretical modeling of each mechanism. We therefore experimentally investigate the energy, wire diameter, polarization, doping, and temperature dependencies of the absorption spectra and compare these results to theoretical predictions for the optical absorption resulting from direct and indirect interband transitions as well as intersubband transitions.

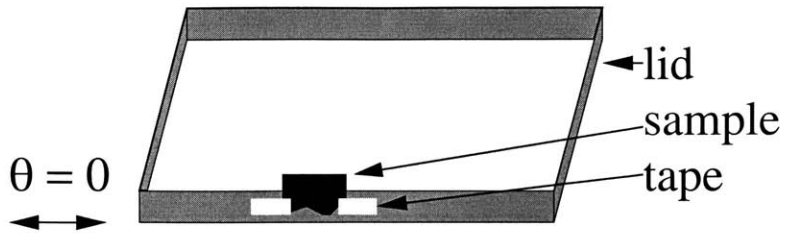

Figure 5-2: A sample mounted on the edge of a lid in preparation for polarization studies. The $\theta = 0$ mark is the direction in which the polarizer internal to the FTIR is set at 0.

5.2 EXPERIMENTAL MEASUREMENTS

This section presents the polarization, wire diameter, doping, and temperature dependent measurements of the optical absorption of bismuth nanowires. In each case the significance of the measurements is discussed. The polarization study helps us determine the selection rules for the absorption mechanism. The wire diameter dependence study helps us deduce the importance of quantum confinement and surface effects to the absorption spectra. Since tellurium acts as an n-type dopant in bismuth, the spectra of the Te-doped samples tell us the dependence of the absorption on the Fermi energy. The temperature dependence helps us to determine the importance of phonons and thermal excitation in the absorption spectra.

5.2.1 POLARIZATION

Since the wires inside the alumina are aligned with their wire axes perpendicular to the surface, the electric field of light incident normal to the sample surface is always perpendicular to the wire axis. In the Nicolet Nic-Plan microscope, in order to do polarization measurements, the sample must be turned onto its side. These measurements use the polarizer internal to the FTIR microscope. In order to put the polarizer into the beam path, the knob on the left side of the microscope should be pulled out. To rotate the polarizer turn the knob. A rotation of 500 units is equal to 180°.

After the sample was cleaved as neatly as possible, it was taped onto the edge of a lid so that the sample formed a right angle to the sample stage. The lid and

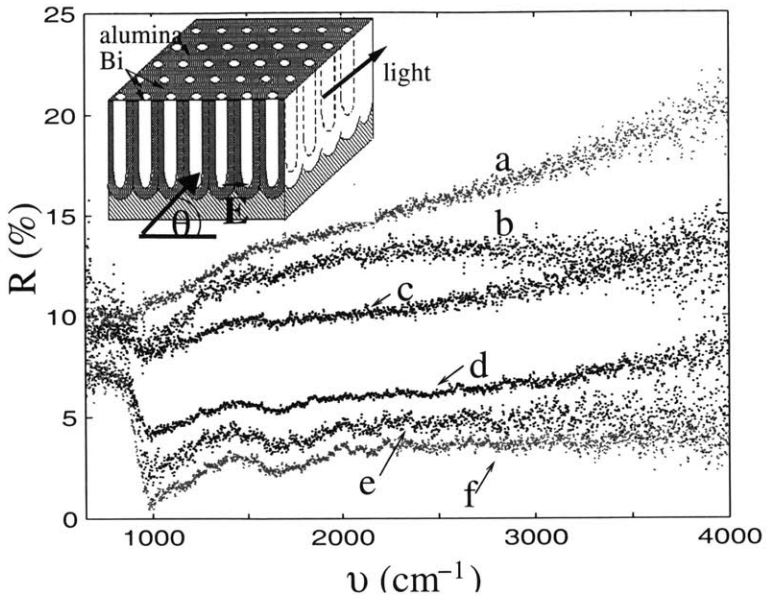

Figure 5-3: Reflection $[R(\nu)]$ of a Bi anodic alumina sample with several polarization angles θ: (a) 90°, (b) 117°, (c) 63°, (d) 27°, (e) -27°, (f) 0°. Curve f ($\theta = 0°$) shows features around $1000\,\mathrm{cm}^{-1}$, while curve a ($\theta = 90°$) does not exhibit clear features in this spectral region. The insert shows a schematic of the sample and the definition of θ.

sample were than placed onto the working stage. Using the FTIR microscope, the edge of the sample was brought into focus. The sample was then manipulated so that the plane of the sample was aligned with the polarizer. Figure 5-2 shows the sample mounted on the edge of a lid and aligned with respect to the polarizer internal to the FTIR. A separate background reference for each polarization direction was taken by measuring the reflection of a gold mirror.

The reflection spectra for light incident from the side of a bismuth-filled template are shown in Fig. 5-3. Curve (f) shows the frequency-dependent reflectivity (vs. ν) for the incident light, polarized perpendicular to the wire axis ($\theta = 0°$), while curve (a) is for light polarized parallel to the wire axis ($\theta = 90°$). The reflectivity spectra for incident light polarized at $\pm 27°$ away from the high-symmetry directions of 0° and 90° are also shown in curves (b)-(e).

As curve (a) in Fig. 5-3 demonstrates, the reflectivity of the bismuth-filled sample when the light is polarized parallel to the wire axis does not exhibit any strong features near $\sim$ 1000 cm^{-1}. A change in polarization, however, causes the appearance

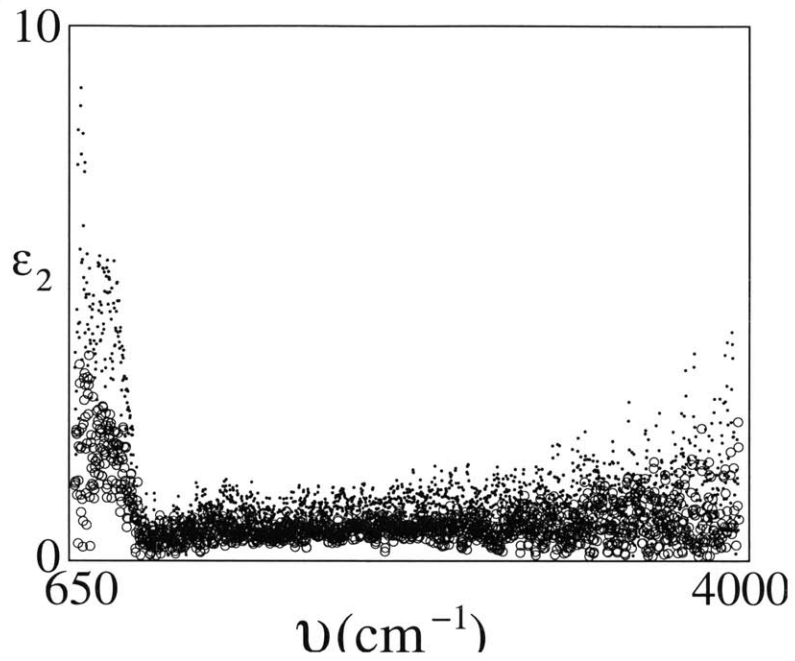

Figure 5-4: The deduced wavenumber dependent imaginary part of the dielectric function (ϵ_2) of alumina for light with the electric field parallel ($\circ$) and perpendicular (.) to the pore axis of the alumina template.

of absorption bands in the reflection spectrum of the filled sample (see Fig. 5-3 b - f). This polarization-dependent absorption was not detected for unfilled alumina templates (see figure 5-4), indicating that this feature is indeed caused by the presence of the Bi nanowires. This polarization dependence is opposite to that seen in polarizers and in carbon nanotubes.

5.2.2 WIRE DIAMETER

Obviously, since strong optical absorption features appear in the mid-IR spectral range in bismuth nanowires that are not present in bulk bismuth, the absorption is highly dependent on wire diameter. This section quantifies this dependence, which is then later related to simulation results in section 5.3.

Figure 5-5 shows the reflection of a polished piece of bulk bismuth and of free standing bismuth nanowires for comparison. The large feature in the reflection spectra of bismuth nanowires near $\sim$ 1000 cm^{-1} is not present in bulk bismuth. Figure

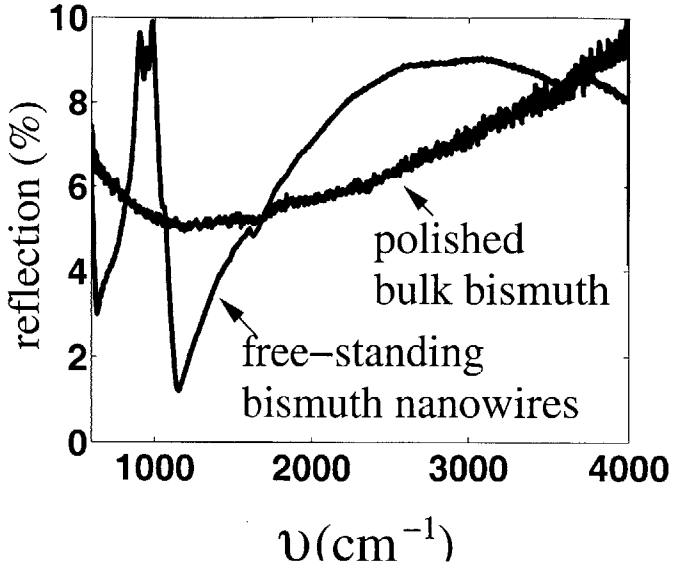

Figure 5-5: Reflection $[R(\nu)]$ of a polished piece of bulk bismuth and of free-standing Bi nanowires for comparison. The large feature near $\sim$ 1000 cm^{-1} in the reflection spectra of the free-standing wires is not present in the reflection spectra of bulk bismuth. The broad features in the bulk bismuth are likely a result of a non-perfect polish or of a misalignment with the sample stage.

5-6 presents the deduced imaginary part of the index of refraction (K) as a function of wavenumber for both 200 nm and the absorption coefficient for 45 nm free-standing bismuth nanowires. The 200 nm wires were formed by filling the pores of the alumina template which was anodized at 160V at 0° C. The alumina was etched away using a selective etch (see section 3.4). Since the sample was too thin to handle without structural support, I left the sample attached to a large piece of bulk bismuth which remained after pressure injection (see section 3.3). Both the nanowires and the bismuth piece were placed into the etch solution to remove the alumina. The reflection was taken on the nanowires protruding out of the bulk bismuth.

The reflection spectra of the nanowires are remarkably different from that of bulk bismuth. The large and intense absorption peak at $\sim$ 1000 cm^{-1} which is present in bismuth nanowires is not measurable in the bulk bismuth spectra (see Fig. 5-5). In addition, even though 200 nm wires of bismuth are too large to have significant quantum confinement effects, an absorption peak at 965 cm^{-1} is measured in these wires.

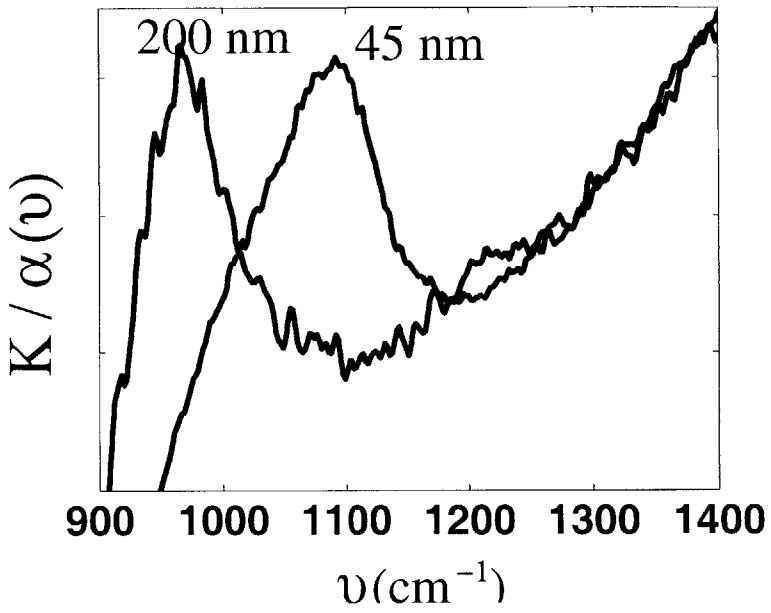

Figure 5-6: The wavenumber dependence of the imaginary part of the index of refraction of $200\,nm$ and absorption coefficient of $\sim 45\,nm$ diameter bismuth nanowires fabricated inside an alumina template but with this template then removed. The absorption peak of the 200 and $\sim 45\,nm$ wire diameter samples are at 965 and 1090 cm^{-1}, respectively. The imaginary part of the index of refraction of the $200\,nm$ diameter wires was obtained by Kramers-Kronig relations and measurements of the optical reflectivity of the sample. The absorption of the $\sim 45\,nm$ diameter wire was obtained from the negative log of the transmission of the sample. The absorption values are not corrected for surface roughness or sample thickness, and so the y-axis scales for the two graphs are different and arbitrary.

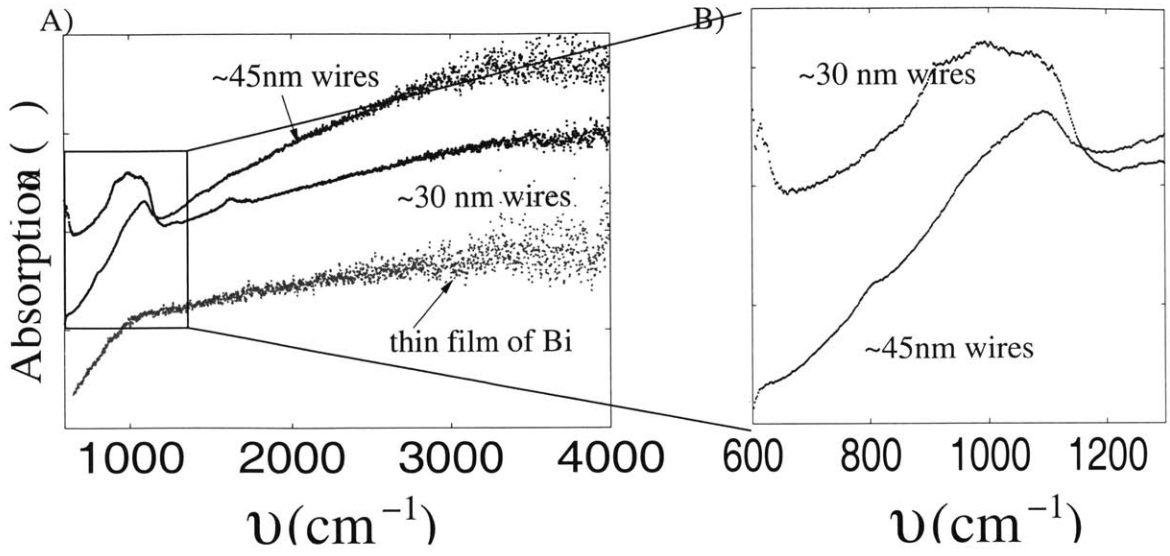

Figure 5-7: A) The dependence of the absorption coefficient on wavenumber, found by taking the negative log of the transmission of free-standing bismuth nanowires with diameters around 45 and 30 nm as well as the absorption on a thin piece of bismuth. An expanded view of the data for the 30 nm and 45 nm wires in the wavenumber range $600 < \nu < 1300$ cm^{-1} is shown in B).

Since the free-standing wires have an oxide thickness that is both uneven along the length of the wire axis and dependent on the etch time (see section 3.4), the diameter of the free-standing wires is not well know. Therefore, for a quantitative wire diameter dependence study, we chose to use the bismuth nanowires inside an alumina template. However, the transmission results for free standing wires with two different wire diameters are shown in Fig.5-7 for comparison. This figure shows that both the 45nm and 30nm diameter wires have optical absorption peaks near 1000 cm^{-1}, but that the spectral shape varies with wire diameter.

The frequency-dependent reflectivity spectra of samples (1-4) in Table 5.1 were measured for the incident light directed parallel to the wire axis. With this sample orientation, the optical electric field is always perpendicular to the wire axis, even for unpolarized light, and therefore intersubband transitions may occur. Using Kramers–Kronig relations and the measured reflection verses wavenumber, the dielectric constant for the composite material is obtained as a function of energy (or wavenumber) (see section 4.2.2). The dielectric function of non-porous alumina

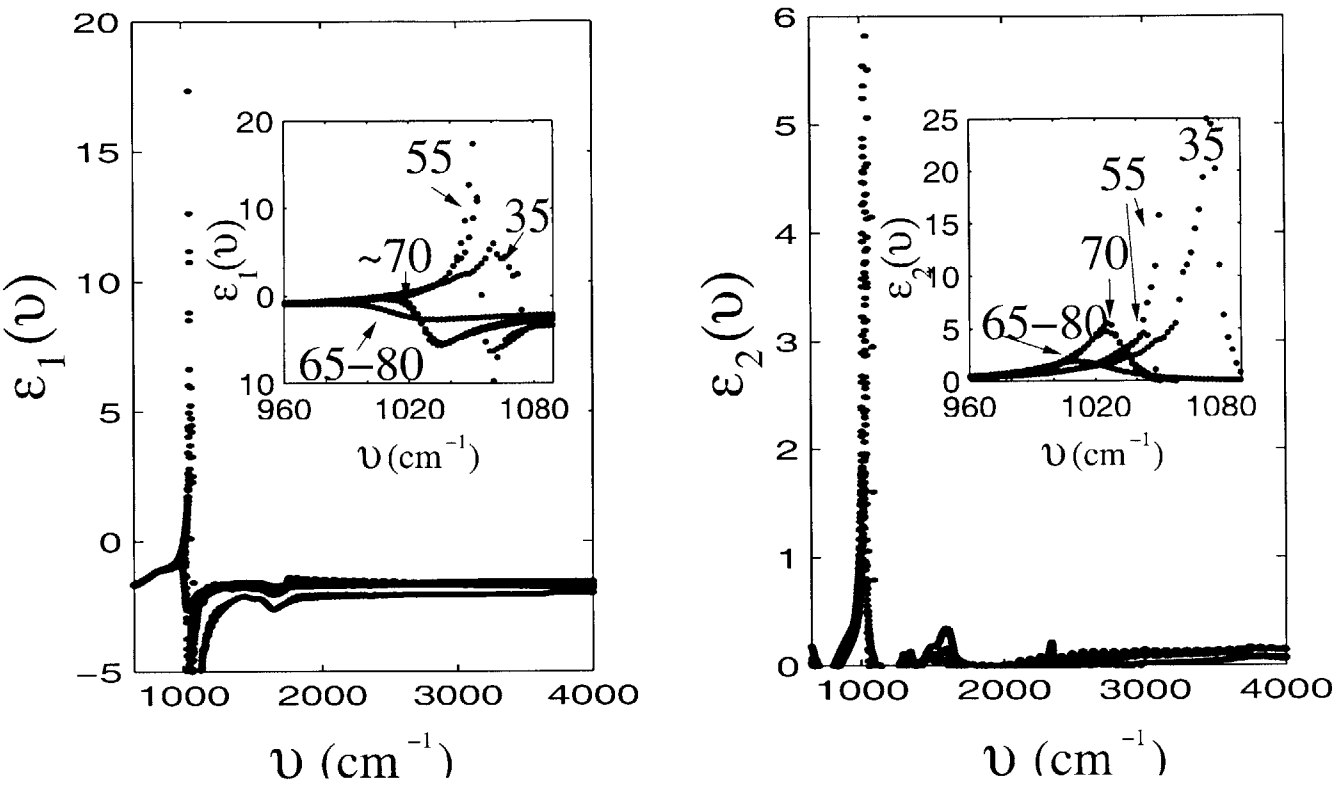

Figure 5-8: The wire diameter dependence of the dielectric function ($\epsilon_1 + i\epsilon_2$) of bismuth nanowires vs. wavenumber obtained from analysis of reflectivity measurements for 35, 55, 70, and 65-80 nm diameter wires. The dielectric function of the bismuth nanowires are deduced by the method described in section 4.2. The deduced dielectric function from two different reflectivity measurements, taken from different locations, for both the 70 and 55 nm diameter samples are shown in the inserted figures for $\epsilon_1(\nu)$ and $\epsilon_2(\nu)$, in order to demonstrate the reproducibility of the results. The inserts show an expanded view of the real and imaginary parts of the dielectric function for the wavenumber range of $960 - 1090$ cm^{-1}.

Table 5.1: Sample processing conditions

voltage (volts)	temperature (K)	wire diameter (nm)	purity of Bi used to fill template(%)
60	273	65-80	99.99
60	275	~70	99.999
40	290	55	99.999
35	273	35	99.999

is obtained using effective medium theory with the aid of the dielectric function of an unfilled alumina template, and the measured porosity of the alumina from SEM images. Again applying effective medium theory, the contribution to the dielectric function of the bismuth nanowires as a function of wavenumber (ν) is deduced from the dielectric function of the bismuth/alumina composite by subtracting the dependence of the dielectric function of the alumina composite (See section 4.2.3). Results thus obtained for the dielectric function $[\epsilon_1(\nu) + i\epsilon_2(\nu)]$ of the bismuth nanowires from samples 1-4 are shown in Fig. 5-8 as a function of wave number (ν). As the wire diameter of the samples decreases from 65-80nm to 35nm, the energy (wavenumber) of the absorption peak increases by 65 cm^{-1}.

The magnitude of the observed increase in the wavenumber of the peak in $\epsilon_1(\nu)$ and $\epsilon_2(\nu)$ with decreasing wire diameter can be explained by quantum confinement. Using a simple model of a particle in a square box and an effective mass that is both parabolic and isotropic, the effective mass corresponding to a 65 cm^{-1} increase in energy when the diameter is decreased from 80nm to 35 nm is calculated to be $0.245m_o$.

5.2.3 TELLURIUM DOPING

Tellurium (Te) impurities are incorporated into our nanowires during the melt process. Concentrations of 0.090, 0.044, 0.018, and 0 weight percent of tellurium were added to produce four samples with different doping levels. Using the density of bismuth ($9.8 g cm^{-3}$) and the atomic mass of Te ($127.6 g/mole$), these weight percentages are

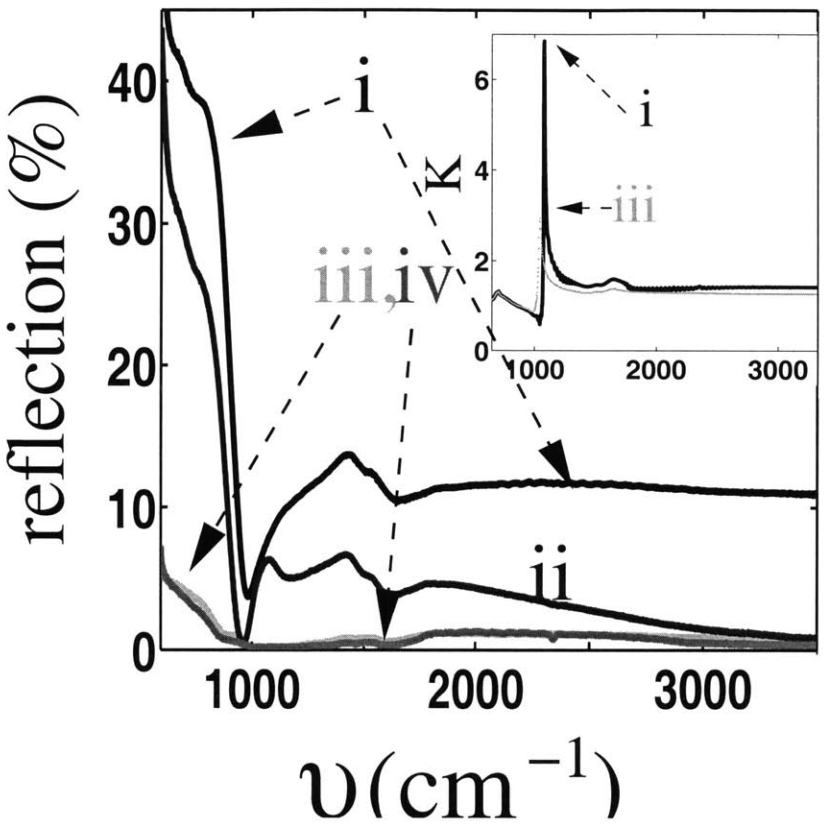

Figure 5-9: (a) The measured optical reflection as a function of wavenumber for: (i) non-doped, (ii) lightly n-type doped, (iii) medium n-type doped, and (iv) heavily n-type doped arrays of bismuth nanowire 40nm in diameter inside an alumina template. The insert shows the deduced imaginary part of the index of refraction, K, for a (iii) doped and (i) undoped sample [4].

turned into an estimate of doping levels of $\sim 4x10^{19}$ cm^{-3}, $\sim 2x10^{19}$ cm^{-3}, $\sim 8x10^{18}$ cm^{-3}, and 0 respectively. Again EDS is not sensitive enough to measure impurity concentrations in the final nanowire sample. The samples are therefore referred to as heavily-doped, medium doped, lightly-doped, and undoped, respectively.

Tellurium impurities in crystalline bismuth act as electron donors, and raise the Fermi energy to account for the increase in electron concentration. The addition of tellurium dopants may also decrease the average time between scattering events (τ), hence decreasing the coherence length, and thereby decreasing our ability to detect quantum effects. Only considering the increase in Fermi energy, we expect that at higher doping levels the lower conduction subbands will become more occupied with electrons. When the conduction band is completely filled with electrons, an optical transition from the valence band to the conduction band is forbidden by the Pauli exclusion principle. Therefore, as the doping increases, transitions involving the higher energy conduction subbands (or lower energy hole subbands) may dominate the optical spectra.

The measured reflection as a function of wavenumber is shown in Fig. 5-9. These nanowire arrays have varying levels of n-type tellurium dopant concentrations. Normally for intrinsic materials, the absorption either remains constant or increases when dopants are added. In bismuth nanowires, however, the reflection decreases as doping is increased. This corresponds to a decrease in the imaginary part of the index of refraction K as seen in the relation

$$R = \frac{(1-n)^2 + K^2}{(1+n)^2 + K^2} \tag{5.1}$$

where R is the reflection of an infinitely thick sample, n is sample's index of refraction, and K is related to its absorption coefficient.

The insert in Fig. 5-9 shows the calculated imaginary part of the index of refraction (K) calculated from the Kramers–Kronig relations from the reflection spectra for the undoped and medium doped samples. The undoped sample has a larger K than the medium doped sample, contrary to the more common effect of increasing

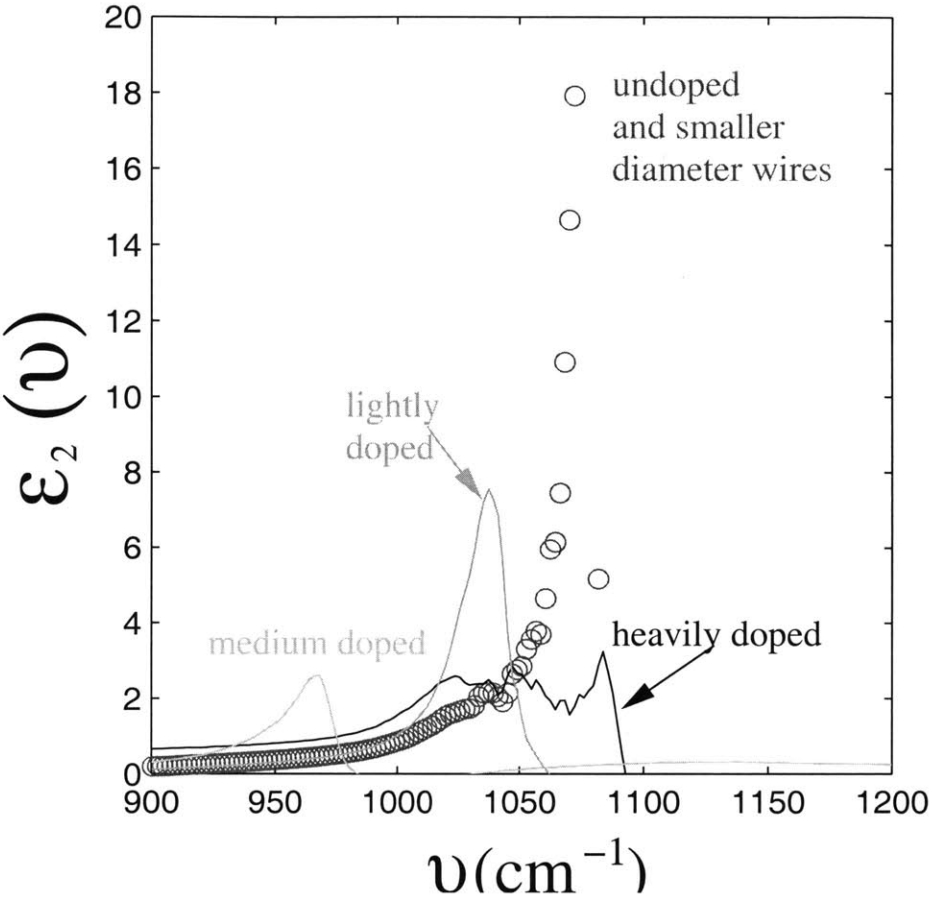

Figure 5-10: The effect of tellurium doping on the imaginary part of the dielectric function $\epsilon_2(\nu)$ as a function of wavenumber of bismuth nanowires ($\sim 55nm$ in diameter) obtained from analysis of reflectivity measurements.

Table 5.2: Processing conditions of Te-doped wires

doping level	voltage (volts)	temperature (K)	diameter (nm)	purity of Bi (%)	dopant type	wt.%Te in melt
none	40	290	55	99.999	none	0
light	45	273	55	99.9999	Te	0.0189
medium	45	273	55	99.9999	Te	0.044
heavy	45	273	55	99.9999	Te	0.090

the absorption intensity with increasing levels of dopants. The unusual trend of a decreased K with an increased doping level will help in identifying the dominant optical absorption mechanism in our samples.

Unfortunately, Kramers–Kronig analysis can not be accurately used on the tellurium-doped samples, especially on the heavily-doped samples, since the transmission at some energies is too large (see section 4.2.2). In addition, the method of fitting Maxwell's equations is only accurate for energies in which both the reflection and transmission are measurable. In these spectra, however, the transmission is below the measurement range of the FTIR instrument for the energies near the absorption peak. Therefore, the dielectric functions of these samples near the absorption peak (and hence K) are not accurately determined. However, in order to get an *estimate* of the absorption of these samples, the Kramers–Kronig analysis is applied to the reflection spectra in order to obtain the dielectric function, and the results are shown in Fig. 5-10. As the doping increases from undoped to light and medium doping, the optical absorption peak shifts slightly to lower wavenumbers. For the heavily doped sample, optical absorption occurs over a wider wavenumber range ($950 - 1100$ cm^{-1}) than for the other samples, and includes significant optical absorption at wavenumbers even larger than that observed in the undoped sample. This curious behavior is likely, at least partially, a result of limitations to the Kramers–Kronig analysis pertaining to the increased transmission intensity in the doped samples. The decrease in the energy of the optical absorption peak with the addition of n-type dopants will be discussed further in section 5.3.4.

5.2.4 SLOPE OF THE ABSORPTION SPECTRA OF FREE-STANDING WIRES

Figure 5-11 shows the negative log of the transmission spectra from four free-standing nanowire samples. The absorption spectra in Fig. 5-11 (a) are normalized to the peak absorption intensity, while the absorption spectra in Fig. 5-11 (b) are simply the negative log of the transmission spectra. Normalization corrects for differences in sample

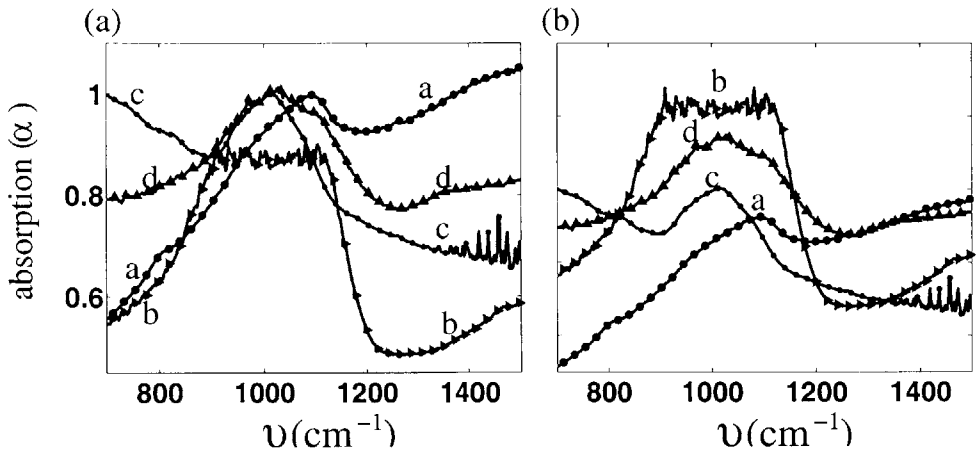

Figure 5-11: The normalized (a) and non-normalized absorption spectra for four free-standing nanowire samples. The absorption was found by taking the negative log of the transmission spectra. The spectra in (a) are normalized to the absorption peak intensity, with the exception of sample b, which was normalized to the extrapolated absorption peak intensity. Samples b, c, and d are were anodized at 45V, while sample a was anodized at 60V. Sample b is tellurium doped, while sample c is antimony doped. Samples a and d are undoped.

thicknesses, but does not account for differences in surface scattering, reflection, and the fact that not all the light goes through the bismuth nanowire sample (since the sample is smaller than the spot size). For sample d, in Fig.5-11, the transmission intensity near the absorption peak was below the limits of the spectrometer, and so the absorption peak could not be resolved. Therefore, the absorption peak value used to normalize the spectra was extrapolated for sample d. Samples b, c, and d were anodized at 45V, while sample a was anodized at 60V. The higher anodization voltage of sample a indicates that in the template this sample had a larger wire diameter. However this sample was etched much longer than the other samples, and therefore also likely has a larger bismuth oxide film. Hence, conclusions of the wire diameter dependence of these samples, therefore should not be made. In addition to the differences in etch time and anodization voltages, these samples differ in doping type. Samples a and d are undoped, while sample b is tellurium doped, and sample c is antimony doped.

Despite the differences in the four samples, their absorption spectra are very similar. For example, the rise in absorption with increasing energy, at the onset of the

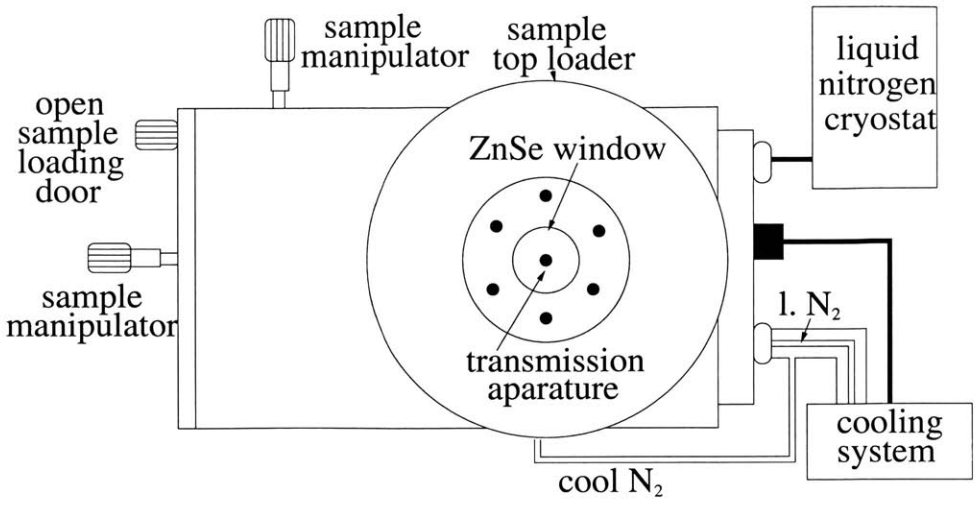

Figure 5-12: A schematic of the Linkum Hot/Cold stage.

absorption peak, is similar in the four samples. This rise in the absorption is a measure of the absorption peak width, and can be quantified by determining the difference between the energy of the peak's maximum absorption intensity and the energy at which the absorption is half its maximum value. For all four spectra, if the slope near the absorption peak is extrapolated, the absorption rises from half its maximum value to its maximum value in about 300 cm^{-1}.

5.2.5 LOW T MEASUREMENTS

Low temperature reflection and transmission measurements were taken using a Linkum Scientific FTIR 600 Hot/Cold Stage. The cold stage fits into the NicPlan microscope FTIR. Measurements are done through a Zinc Selenide window, see Figs. 5-12 and 5-13. The cold stage is designed for both transmission and reflection measurements down to liquid nitrogen temperatures. The sample space inside the cold stage is 2mm high and 18mm in diameter.

Since the samples were often small, they were usually placed onto a KBr window for experimental ease. The window was then placed onto the sample holder. Since the sample holder can be moved relative to the beam path by knobs external to the sample space, see Fig. 5-12, different locations of the sample could be measured

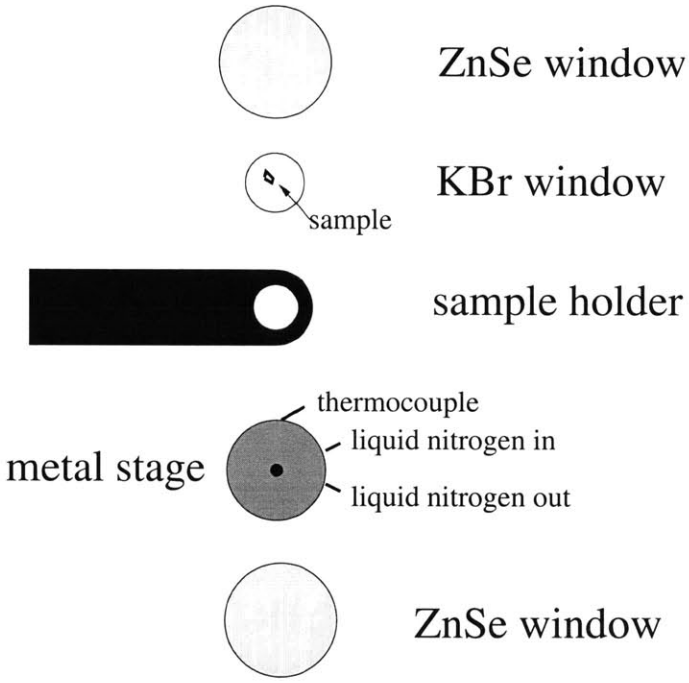

Figure 5-13: A cross-sectional schematic of the Linkum Hot/Cold stage. The sample is placed on top of a KBr window, which is then placed on top of the sample holder. The sample holder allows the sample to be moved relative to the beam path. The sample holder is in contact with the metal stage which is cooled by liquid nitrogen. The temperature reading of the cold-stage is measured from a thermocouple in contact with the metal stage. ZnSe windows are placed above and below the sample to isolate the chilled sample space and to allow for optical measurements.

Table 5.3: Temperature of Sample vs. Metal Plate

T metal plate (°C)	T on top of KBr (°C)
19	22
-50	-29
-100	-65
-150	-98
-170	-112
-190	-123

without heating and re-cooling the sample. However, the temperature controller on the cold-stage monitors the temperature of the metal stage underneath the sample and not the actual sample temperature. The location of the thermocouple internal to the cold stage is shown in Fig.5-13. When the sample is placed on top of a KBr window, on top of the sample holder, on top of the metal stage, the temperature of the sample might be different than that of the metal stage. In order to measure the temperature difference between the metal stage and that on top of the KBr window, a thermocouple was wired through the sample loading door and placed on top of the KBr window. Using this thermocouple, the temperature on top of the window, where the nanowires sit during a measurement, was compared to the temperature reading internal to the cold stage of the metal stage. These temperature values are shown in Table 5.2.

The temperature on top of the KBr window was consistently higher than the temperature on the metal stage. This calibration gives a conservative estimate of the sample temperature, since in order to measure the voltage across the thermocouple, the sample loading door was left ajar. In the optical measurements, this door is shut, and so the temperature of the sample maybe cooler than that measured in this calibration. In addition, to the difference in temperature of the sample and that of the metal stage (hence the cold stage's internal temperature reading), the temperature on top the KBr window increases with time. Since cooling is partially obtained by cold nitrogen gas flowing through the sample holder, and since when the temperature

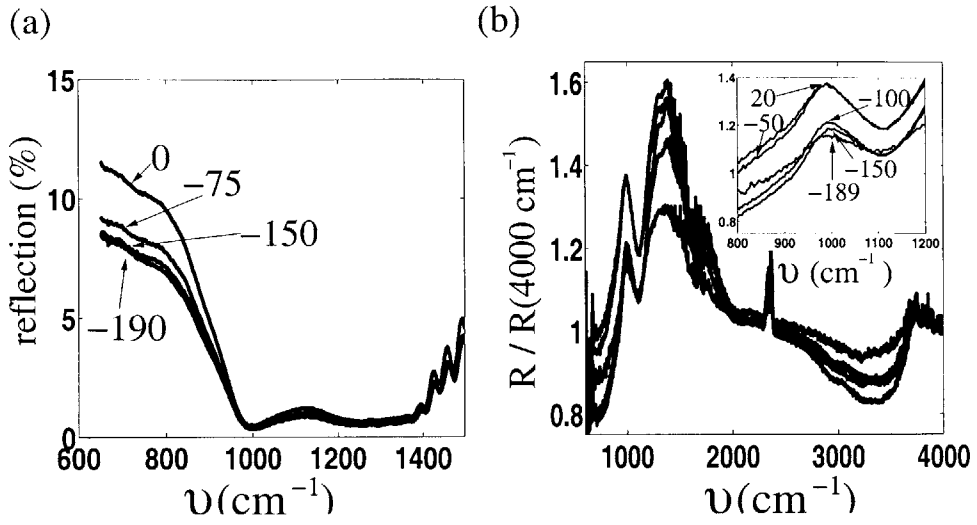

Figure 5-14: (a) Reflection of a bismuth-filled alumina template anodized at 20V at a temperature of 0°C, −75°C, −150°C, and −190°C. (b) Reflection of a same sample in (a), but with the alumina removed. The reflection is normalized to the reflection at 4000 cm^{-1}. The bismuth nanowires are on top of a gold film. The reflection measurements were taken at 20°C, −50°C, −100°C, −150°C, and −189°C. The insert shows an expanded plot of the normalized reflection for a wavenumber range of 800 − 1200 cm^{-1}

is constant very little cool gas flows over the sample, the sample heats up slightly if the temperature of the metal plate is held at a cold temperature.

In order to keep the sample as close to the temperature measured by the cold-stage as possible, for large samples, the sample was placed directly onto the metal stage. For reflectivity measurements, the beam path was mis-aligned slightly so that the light shone onto the sample and did not go through the aperture used for transmission measurements. In other words, the KBr window and the sample holder shown in Fig.5-13 were not used for samples large enough to not require a KBr window. This method could only be applied to samples inside an alumina template since all the free-standing wire samples were much too small to be handled when not using a KBr window.

Figure 5-14 presents the reflection of both a bismuth-filled alumina template and free-standing bismuth nanowires for various temperatures. The reflection near 1000 cm^{-1} decreases slightly with decreasing temperature for both the bismuth nanowires inside an alumina template, Fig. 5-14 (a), and for free-standing wires, Fig. 5-14 (b).

The decrease in reflection in Figs. 5-14 (a) and (b), indicates a slight decrease in the absorption with decreasing temperature. Surprisingly, the energy (wavenumber) of the optical feature near 1000 cm^{-1} remains relatively constant for temperatures down to $-190°C$, as evident by the similar shapes of the spectra in both Figs. 5-14 (a) and (b). Since the bandgap, band-overlap, free carrier concentrations, phonon energies, and free-carrier effective masses of bismuth are all temperature dependent, this result is unexpected.

5.3 SIMULATIONS OF OPTICAL ABSORPTION RESULTING FROM ELECTRONIC TRANSITIONS IN BISMUTH NANOWIRES

Models of the optical absorption in bismuth nanowires from different absorption mechanisms are presented in this section in order to gain insight into the mechanism responsible for the absorption peaks in the experimental data. Free carrier absorption, intersubband transitions within the L-point conduction band, interband transitions from valence subbands at the L-point to conduction subbands at the L-point, and indirect transitions from valence subbands at the L-point to valence subbands at the T-point are presented. These simulations are then compared and discussed in relation to the measured spectra shape, energy of the peaks, and diameter, polarization, and temperature dependencies of the absorption in bismuth nanowires.

5.3.1 INTRABAND TRANSITIONS - FREE CARRIER ABSORPTION

The typical reflection curve resulting from free carrier absorption in metals is different from the measured reflection spectra of both the bismuth nanowires inside alumina and that of free-standing wires. An example of a reflection spectra dominated by free carrier absorption in a material is shown in Fig. 5-15. In this figure the parameters

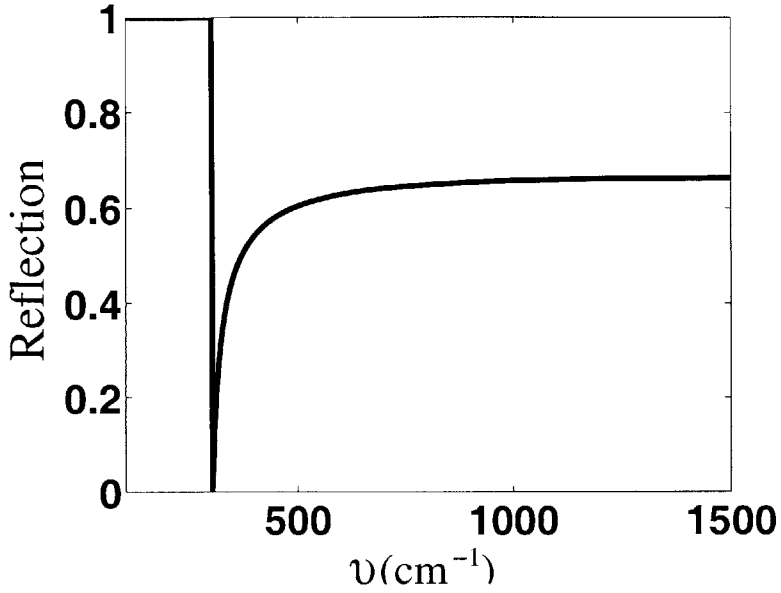

Figure 5-15: Calculated reflection spectra resulting from free carrier absorption where the plasmon frequency is 333 cm^{-1}, $\epsilon_{core} = 100$, and $\omega\tau >> 1$.

measured in bulk bismuth are used; the core dielectric function (ϵ_{core}) is set to 100 and the plasmon frequency to 333 cm^{-1} [80]. In addition, the scattering time (τ) is assumed to be much larger than the frequency of light (ω). In this spectra, the dominant feature is below the lower limit of 600 cm^{-1} for our measurement range and therefore was not measured. In addition, for most of the experiments, the electric field of the incident light is perpendicular to the wire axis, and so the free electrons are limited in motion by the wire boundaries. Since the wavelength of the light inside the bismuth ($\sim 10\mu m/\sqrt{100} = 1\mu m$) is much larger than the wire diameters used in this study, the free-carrier scattering is so intense that the free carrier absorption is not expected to be significant.

Figure 5-16 a) shows the calculated free carrier plasmon frequency of bismuth nanowires as a function of diameter at 293 K. The free carrier plasmon frequencies of bismuth nanowires are calculated by assuming $\epsilon_{core} = 100$ and a bulk plasmon frequency at room temperature of 333 cm^{-1}. In addition, the scattering time, τ, is assumed to be large. By calculating the ratio of the free carrier concentration in bulk bismuth to that of bismuth nanowires of a fixed wire diameter, the plasmon

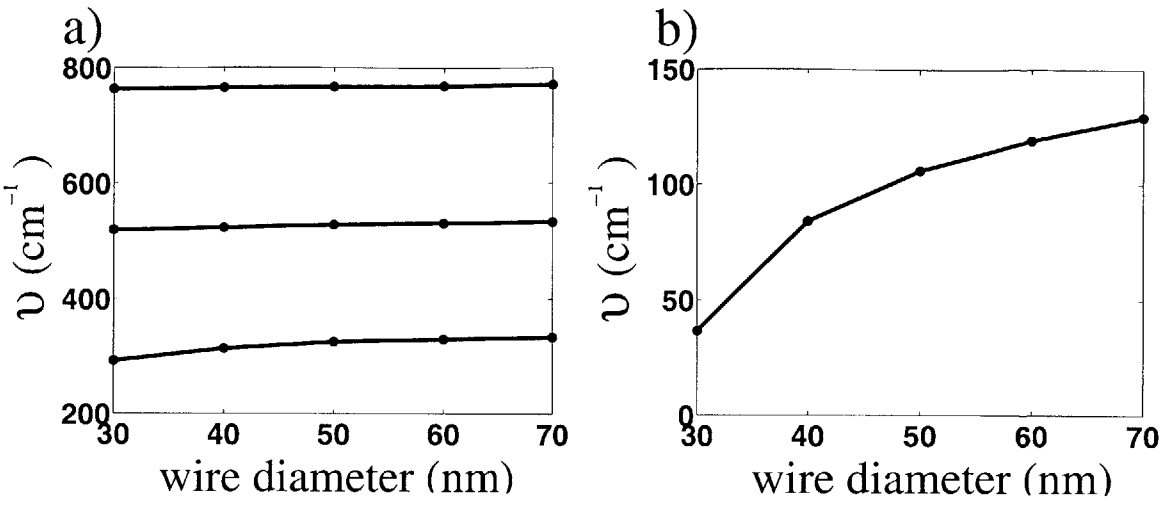

Figure 5-16: a) The calculated free carrier plasmon frequency as a function of wire diameter at room temperature for undoped, $8x10^{18}$ cm^{-3} doped, and $2x10^{19}$ cm^{-3} doped bismuth nanowires. b) The calculated free carrier plasmon frequency as a function of wire diameter at 77K for undoped bismuth nanowires.

frequency for the bismuth nanowires is obtained. As the wire diameter decreases, the free carrier concentration decreases, and so that the plasmon frequency decreases. For example, in 30 nm diameter wires, at room temperature, the carrier concentration is $3.0x10^{18}$ cm^{-3}, while in bulk bismuth the carrier concentration is $3.9x10^{18}$ cm^{-3}, thus giving a plasmon frequency of 292 cm^{-1} for 30nm diameter wires compared to a plasmon frequency of 333 cm^{-1} in bulk bismuth. For the doped samples, the plasmon frequency is larger than in undoped samples and is only weakly dependent on wire diameter. Figure 5-16 a) plots the plasmon frequency as a function of wire diameter for wires doped at a concentrations of $8x10^{18}$ cm^{-3} and $2x10^{19}$ cm^{-3} assuming all dopants are activated. Figure 5-16 b) shows the calculated plasmon frequency, under the same assumptions, for undoped nanowires, at 77K, as a function of wire diameter. For the 77K, the measured bulk plasmon frequency is 158 cm^{-1} [80]. The calculations of the carrier concentration make use of a previously published model [14, 70] and take into the non-parabolicity of the L-point bands.

5.3.2 INTERSUBBAND

Inter-subband transitions were suspected to be the cause of certain features in the observed optical absorption in bismuth nanowires for several reasons. The most convincing reason is that the polarization dependence of the optical absorption is consistent with absorption from intersubband transitions. The absorption is observed when the electric field of the incident light is perpendicular to the wire axis but is not observed when the electric field is parallel to the wire axis. For the light polarized parallel to the wire axis ($\theta = 90°$), we do not expect to see any intersubband transitions, since in this case, the electric field is uniform in the quantum-confined direction. Therefore, the electromagnetic dipole matrix element, $\langle c_1|\frac{e}{mc}\vec{p}\cdot\vec{A}_{\text{light}}|c_2\rangle$, between the two conduction subband states, c_1 and c_2, vanishes, and no electromagnetic coupling occurs between the two subbands. In addition, when the light is polarized parallel to the wire axis, the reflection is dominated by the free carriers contributing to the reflectivity. When the light is polarized perpendicular to the wire axis ($\theta = 0°$), the subbands may be coupled through the electromagnetic interaction which couples the momentum of the electrons to the vector potential of the light. Thus, we expect to observe an intersubband resonance for light polarized perpendicular and not for light polarized parallel to the wire axis, consistent with observations. In addition, we suspect the measured absorption to be the result of intersubband absorption because the energy (wavenumber) of the peak absorption was found to increase with decreasing wire diameter as expected for intersubband transitions. Furthermore, the energy range where absorption peaks are observed is the energy range in which absorption from inter-subband transitions is expected. [70]

A photon can excite an electron to an unfilled higher energy state if the energy of the photon exactly equals the energy difference between the final and initial states and if momentum is conserved. The photon absorption from this process can be measured by the energy-dependent optical absorption spectrum. When stimulated emission as well as absorption is accounted for, the optical absorption coefficient for the Bi nanowire quasi 1D system as a function of photon energy, $\hbar\omega$, is given by

$$\begin{aligned}\alpha_{abs,1D}(\omega) &= (\pi e^2/\epsilon_0 c\eta\omega m^{*2}) \sum_{n,m}(2/2\pi) \\ &\times \int dk_z |\langle n|p|m\rangle|^2 [f(E_n) - f(E_m)] \\ &\times \delta(E_n - E_m - \hbar\omega)\end{aligned} \tag{5.2}$$

where α is the optical absorption coefficient, ω is the frequency of the incident light, $\langle n|p|m\rangle$ is the momentum matrix element for coupling between the nth and the mth states, z is wire axis direction, η is the index of refraction, m^* is the effective mass of the carriers, c is the speed of light, and E_n and E_m are the energy of states n and m, respectively. $f(E_n)$ and $f(E_m)$ are the Fermi-Dirac distribution functions for the states n and m, respectively as calculated from the equation

$$f(E) = \frac{1}{exp[(E - E_f)/k_B T] + 1} \tag{5.3}$$

where E_f is the Fermi energy and k_B is the Boltzmann constant. The imaginary part of the dielectric function, ϵ_2, can be related to the optical absorption coefficient by

$$\epsilon_2(\omega) = c\eta\alpha_{abs}(\omega)/\omega. \tag{5.4}$$

Combining Eqs. 5.2 and 5.4, we obtain an expression for the imaginary part of the dielectric function:

$$\begin{aligned}\epsilon_{2,1D}(\omega) &= (\pi e^2/\epsilon_0 \omega^2 m^{*2}) \sum_{n,m} \\ &\times (2/2\pi) \int dk_z |\langle n|p|m\rangle|^2 [f(E_n) - f(E_m)] \\ &\times \delta(E_n - E_m - \hbar\omega).\end{aligned} \tag{5.5}$$

Many commonly used approximations are not valid for calculations on bismuth nanowires. For example, since the bandgap of our bismuth nanowires is less than $3k_B T$ at room temperature, the complete Fermi-Dirac distribution must be used. In addition, since the L-point bands are strongly coupled, a simple parabolic band

model is insufficient, and the Lax 2-band model for non-parabolic coupled bands must be used to describe the dispersion relations [81]. Furthermore, since the L- point electronic bands are extremely anisotropic and have strong non-parabolic effects, the calculation of the wave functions of the quantum states (as well as the coupling between these states and the joint density of states) requires a numerical calculation.

Some assumptions were made in the model presented here that in future studies should be further explored. For example, interband to inter-subband coupling is not considered. Also, electron-electron interaction including the depolarization effect is not considered in this study. Since the electron pockets are localized in k-space, the k-dependence of the momentum matrix elements are not considered. Lastly, only the dominant crystalline direction $\langle 012 \rangle$ is considered for the orientation of the Bi nanowires.

The selection criteria for inter-subband transitions in most systems can be summed up by a few selection rules. However, since bismuth has a very anisotropic band structure and because of the bismuth nanowire's radial symmetry, the selection rules are more complicated than for quantum wells, quantum dots, square nanowires, or even circular wires made from a material with an isotropic band structure. Therefore, a numerical method is used to solve for the oscillator strengths of the inter-subband transitions. Even though the coupling between lower order states is strong, the lower energy limit of our measurement setup prevents us from observing these transitions. The energy (wavenumber) between the first subband and the second subband edge is only $140\,\mathrm{cm}^{-1}$, while the lowest energy (wavenumber) measured by our experimental setup is $600\,\mathrm{cm}^{-1}$. Therefore only higher order transitions with significant coupling are experimentally observed, and for this reason the model calculations include absorption from higher order states.

A more complete version of a previously published model of the electronic structure[14] is used to find the energy levels and wave functions for the first 50 subbands, using a certain wire crystallographic orientation along the wire axis, and using as variables, the wire diameter, and the temperature. Using the energy levels and wave functions calculated with this model, the oscillator strengths between each of the 50

states to every other one of the 50 states are calculated. The oscillator strengths, F_{nm}, are found in terms of the following integral

$$\begin{aligned} F_{nm} = & \ [2/(m^*\hbar\omega_{n,m})]|\langle n|p_{x,y}|m\rangle|^2 \propto |\langle n|p_{x,y}|m\rangle|^2/\omega_{n,m} \\ \propto & \ |\int \psi_n(E_x d/dx + E_y d/dy)\psi_m dA|^2/\omega_{n,m} \end{aligned} \tag{5.6}$$

where ψ_n and ψ_m are the wavefunctions for the nth and mth states, and E_x and E_y are the electric field components of the incident light perpendicular to z, the wire axis, and $\hbar\omega_{n,m}$ is the energy between states n and m. We assume that the incident light is TEM (transverse electromagnetic wave) and hence, the integration is carried out over the cross sectional area, A, of the wire.

Figure 5-17 shows the oscillator strengths, F_{nm} from Eq. 5.6, for transitions from the first ($n = 0$) state to the 50 lowest states ($n = 0 - 49$). In doing the calculations, the polarization of the incident light is varied by 5.6° increments to cover the whole 360° range. Since unpolarized light is used in our experiments, the polarization that gives the largest oscillator strength for each transition is shown in Fig. 5-17. The coupling between the first 50 states, or 2,500 transitions, is calculated for the three L-point carrier pockets.

Higher order states have more nodes in their wavefunctions, and hence the overlap integral with the first state in general decreases with increasing n. However, this decrease is not at all monotonic, since some transitions do not allow for first-order coupling because of selection rules. Since bismuth is anisotropic, and since the circular wire has only one index number, the higher order states sometimes have only a few nodes and hence have a relatively large coupling to lower order states. The $n = 32$ state is an example of a high n state that is slowly varying with few nodes and therefore has significant coupling to the $n = 0$ state. The 2-D wavefunctions of the $n = 0$, 1, 2, 3, 14, 15, 31, and 32 states in a circular bismuth nanowire are shown in Fig. 5-17.

The frequency dependence of $\epsilon_2(\omega)$ resulting from inter-subband transitions from states $n = 0$–29 to states $n = 0$–49 for 41.5 nm diameter, $\langle 012\rangle$ oriented, bismuth

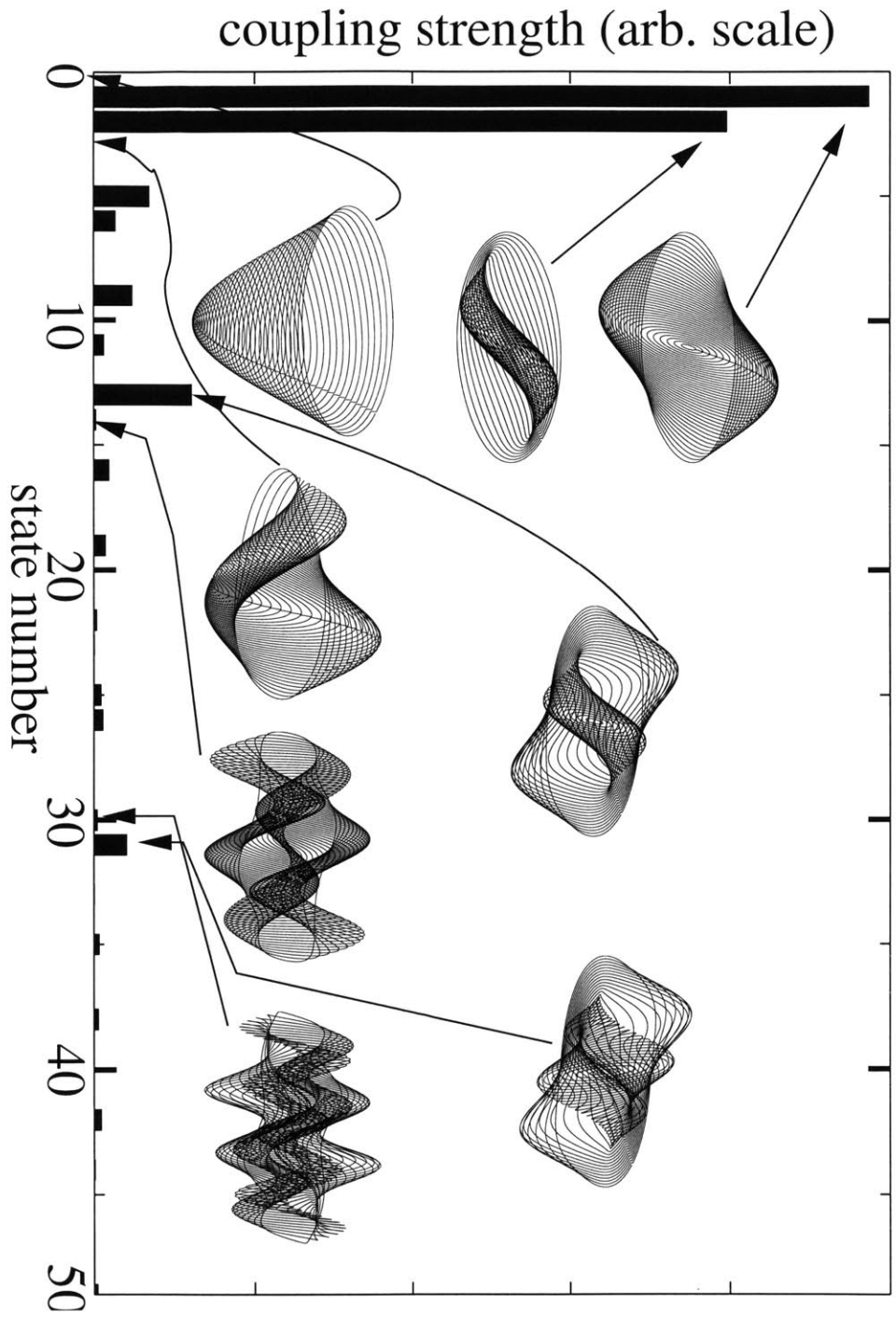

Figure 5-17: The coupling strength, $F_{n.m}$ from the $m = 0$ state to the $n = 0$ to 49 states for carrier pocket A (see insert of Fig. 5-18). The wavefunctions of some states are shown ($n = 0$, 1, 2, 3, 13, 14, 30, and 32). States that are radially anti-symmetric have a larger coupling to the symmetric lowest energy $m = 0$ state. Also, the figure shows that even higher order states can have significant coupling to the $m = 0$ state.

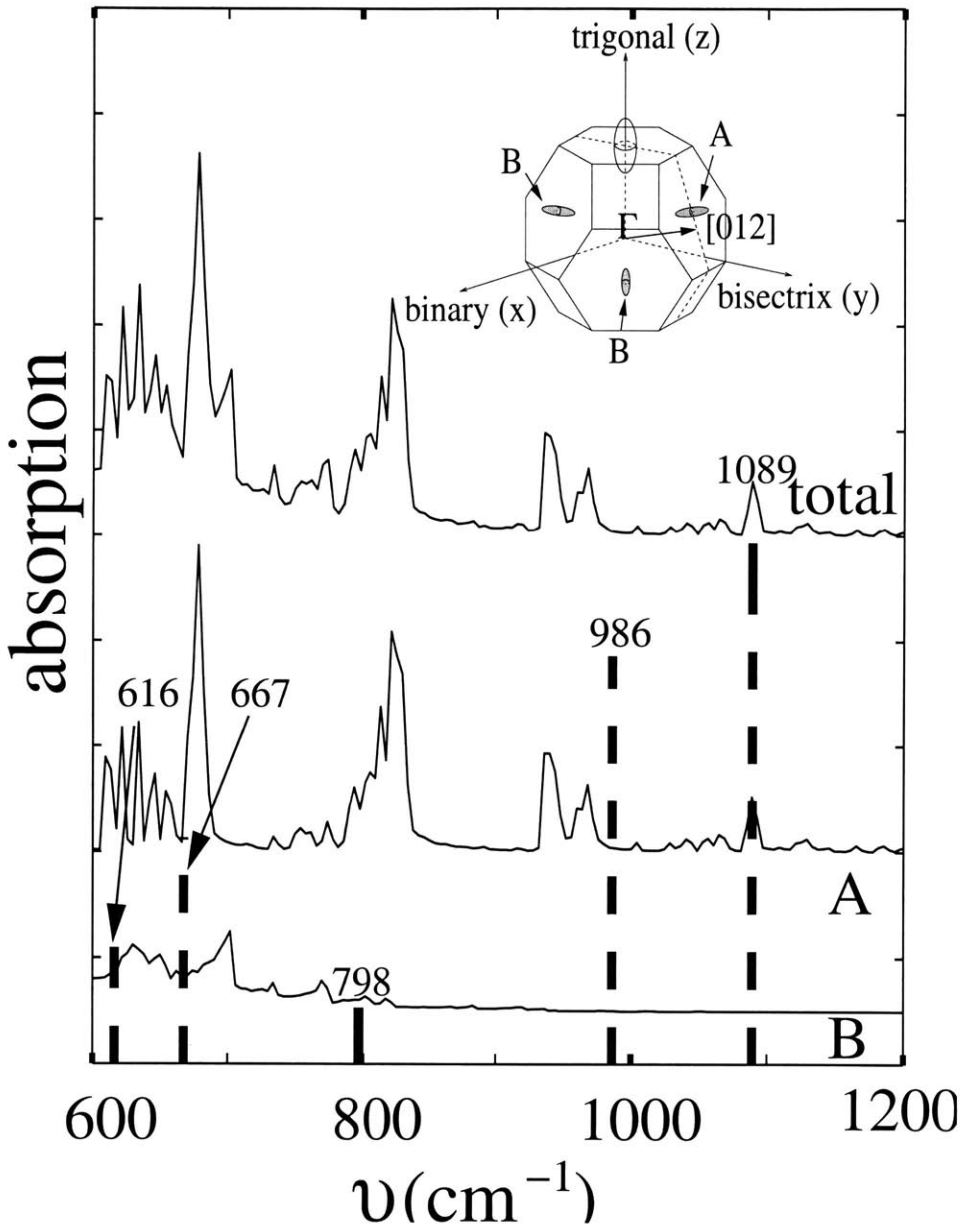

Figure 5-18: The calculated optical absorption at 293 K resulting from inter-subband transitions for 41.5 nm Bi nanowires oriented along the ⟨012⟩ crystalline direction. The separate contributions from the two types of electron carrier pockets, A and B, as well as the total optical absorption are presented. The energies and relative intensities of the experimental absorption peaks are shown by the heavy dashed lines. In the insert, the Brillouin zone of bismuth is shown and the ⟨012⟩ crystalline direction is indicated by the arrow from the Γ point.

nanowires at 293 K is calculated by the equation

$$\begin{aligned} \epsilon_2(\omega) &\propto (1/\omega) \sum_p \sum_{n=l0}^{29} \sum_{m=0}^{49} \int \delta[E_n(k) + E_m(k) - \hbar\omega] \\ &\times F_{nm}[f(E_n(k) - f(E_m(k)]dk_z \end{aligned} \tag{5.7}$$

where the sum over p is over the three electron carrier pockets (the singly degenerate pocket A and the doubly degenerate pockets B), as shown in the insert of Fig. 5-18, and the sums over n and m are for the initial and final states, n and m. The integral includes a delta function where the energy of the incident light equals the energy difference between the initial and final states (n and m). The integral also includes the oscillator strength, F_{nm}, as discussed above. The integral is carried out over momentum, k_z, in the direction of the wire axis. The doping of the nanowires can be changed by adjusting the Fermi energy in the Fermi-Dirac distribution function, see Eq. 5.3. For all calculations in this work, the wires are assumed to be undoped, so the Fermi energy is set so that the nanowires are charge neutral. Since bismuth has both L-point and T-point valence bands and only an L-point conduction band near the Fermi energy, the Fermi energy in undoped samples is much closer to the L-point conduction band than to the L-point valence band. Therefore, intersubband absorption from the conduction band will dominate over the intersubband absorption from the valence band.

The resulting frequency-dependent absorption curve for $41.5nm$ wires is shown in Fig. 5-18. In $\langle 012 \rangle$ aligned Bi wires (such as our wires), two of the three electron pockets are degenerate. The two degenerate pockets are labeled "pocket B" in Fig. 5-18 and the third electron pocket is labeled "pocket A". On one hand, the optical absorption should be dominated by pocket A, since this pocket has the largest effective mass in the unconfined direction and therefore has the largest joint density of states. On the other hand, pocket B is doubly degenerate. Therefore, both types of pockets contribute significantly to the inter-subband absorption spectra. Pocket A has the smaller effective mass in the confined directions and therefore has a larger energy separation between subbands. Pocket A, hence, has larger absorption peaks separated by larger energy intervals compared to those of pocket B.

For perfectly parabolic and symmetric bands, the energy for an electron to make an $n \rightarrow m$ transition over a fixed number of states is independent of the initial state. For example, the energy for a transition between the first and third states is the same as the energy for a transition from the third to the fifth states. Even though Bi nanowires are very anisotropic and non-parabolic, we see from Fig. 5-18 that the 1,500 transitions modeled for each pocket tend to have energies similar to other transitions in that pocket, so that the complete absorption spectra includes only a few absorption peaks, each broader than the spectra resulting from a single transition. For example, the peak at around $800\,\mathrm{cm}^{-1}$ is a sum of the absorptions from transitions from states 3, 5, 8, and 10 to states 21, 26, 32, and 37 respectively. Similarly the absorption peak around $1100\,\mathrm{cm}^{-1}$ is a sum of the absorptions from transitions between states 5 and 7 with states 36 and 42 respectively. This effect is more obvious for pocket A than for pocket B, since pocket A has a larger energy difference between states. In addition to the transitions having similar energies, many transitions are not allowed by symmetry, or are only weakly allowed. These two effects combine to result in only 6-10 expected large absorption peaks in the frequency range 600 and $2000\,\mathrm{cm}^{-1}$.

Included in Fig. 5-18 are dashed lines indicating the frequencies for the absorption peaks that are experimentally observed for $\sim 45nm$ wires, as shown in Fig. 4-9. The height of the dashed lines are proportional to the absorption peak intensity used in the fit. In addition, Fig. 5-19 shows the fit to the experimental data (after background subtraction), the simulated spectra for 41.5 nm diameter Bi nanowires, and the energy derivative of the measured spectra. The calculated energies of the absorption peaks of the 41.5 nm diameter wires agree well with of the experimentally measured energies of the absorption peaks in the ~ 45 nm diameter free-standing wires. The agreement between the experimental and model results is quite good considering that the data for the room temperature bismuth band parameters used for the calculations are not accurately determined [1], that the wire diameters are only known to ± 5 nm (as discussed is section 3.4 in connection with the oxide coating), and that the Fermi energy is not independently known. However, the ratio of the absorption peak intensities as well as the overall spectral shape do not agree well with theory. From Fig. 5-18

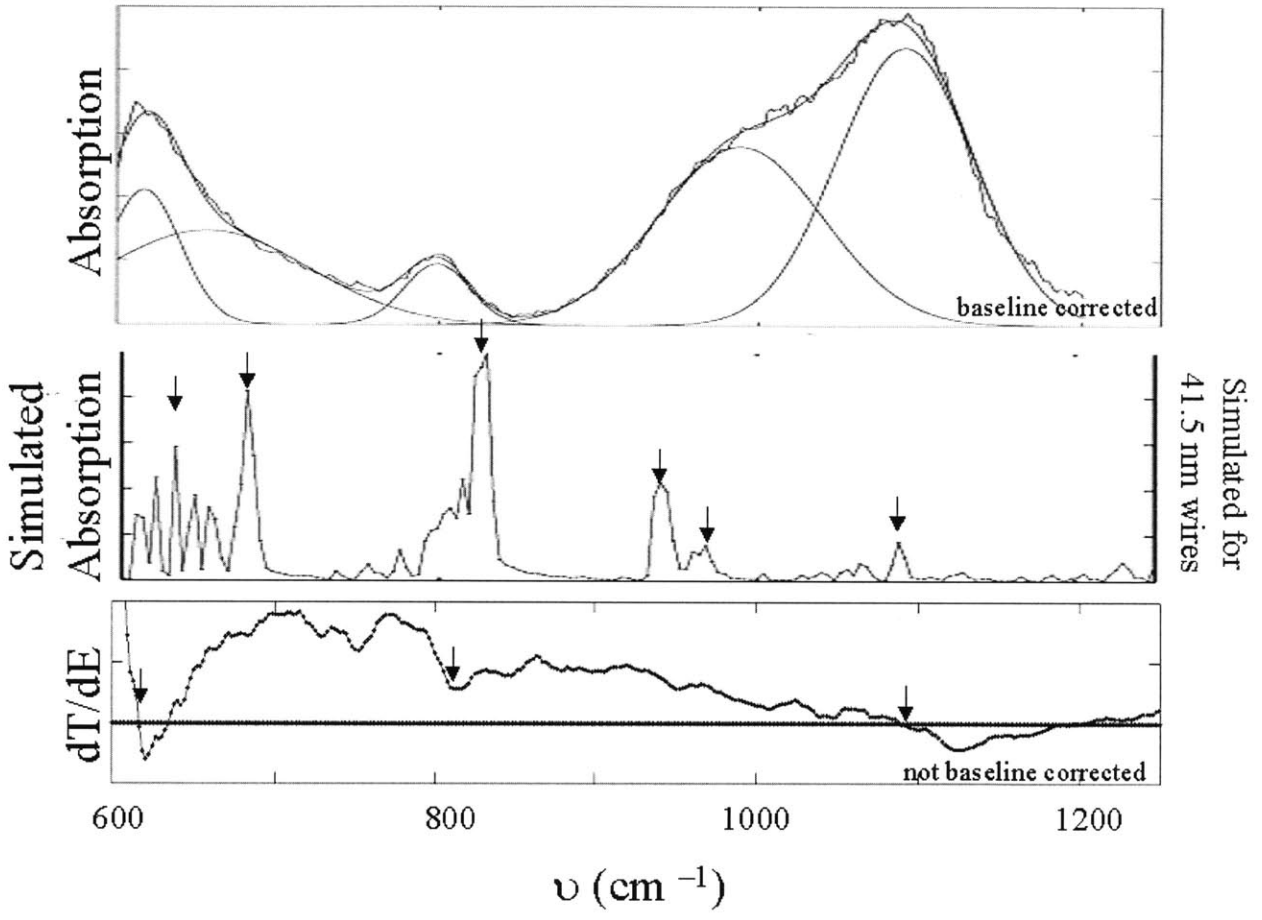

Figure 5-19: The measured absorption spectra of $\sim 45nm$ diameter wires and the fit of the spectra to a sum of Gaussian curves after background subtraction, the simulated absorption spectra resulting from intersubband absorption from $41.5nm$ diameter wires, and the energy derivative of the measured data from $\sim 45nm$ diameter wires.

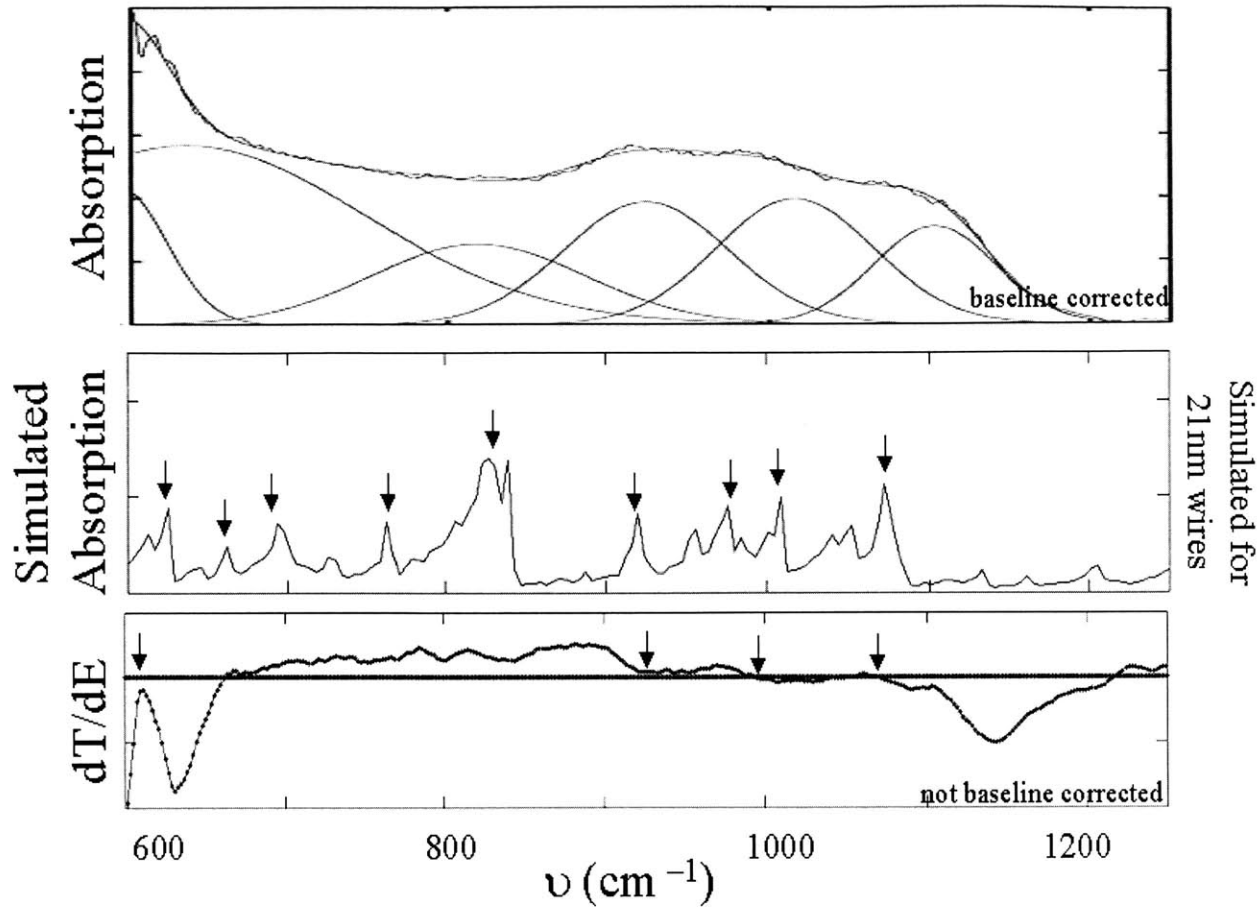

Figure 5-20: The measured absorption spectrum of $\sim 30nm$ diameter wires and its fit to a sum of Gaussian components, after background subtraction, the simulated absorption spectra resulting from intersubband absorption from $21nm$ diameter wires, and the energy derivative of the measured transmission data from $\sim 30nm$ diameter wires.

and Fig. 5-19 we see that the experimental $1089\,\mathrm{cm}^{-1}$ absorption peak is significantly larger than the peaks at ~ 616, ~ 667, and $\sim 798\,\mathrm{cm}^{-1}$. In the simulations, the $1089\,\mathrm{cm}^{-1}$ peak is relatively small, since the absorption peak intensities decrease with increasing wavenumber, because of the decreasing coupling, as shown in Fig. 5-17. The difference in the peak intensities between the theory and experimental results could be explained by other absorption mechanisms contributing to the absorption at around $1100\,\mathrm{cm}^{-1}$, including interband L-point absorption and indirect L-point to T-point absorption as discussed in the next two sections.

In addition to the $\sim 45nm$ wire, absorption of a $\sim 30nm$ wire was also measured,

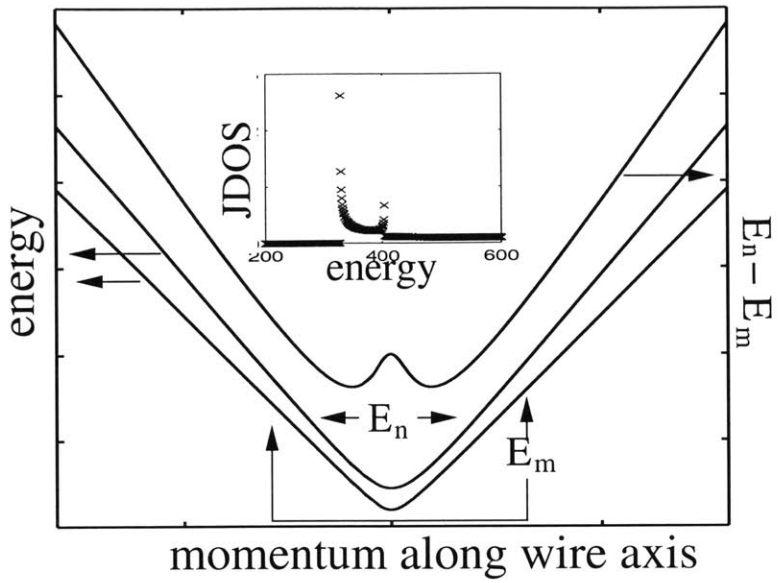

Figure 5-21: Two subbands (labeled E_n and E_m) and the energy difference between them ($E_m - E_n$) shown as a function of momentum along the wire axis. The corresponding joint density of states (JDOS) is shown in the insert. The non-parabolic effects cause the minimum energy difference between two subbands to be away from the subband edges. Thus, the joint density of states, as shown in the insert, has two singularities: the higher energy singularity resulting from transitions at the subband edge, and the lower energy singularity resulting from transitions at the location of the minimum energy difference between the subbands.

fit, and compared to theory. Figure 5-20 the shows the fit to the experimental data (after background subtraction), the simulated spectra, and the energy derivative of the measured transmission spectra of the $\sim 30nm$ wires. Again the fit is reasonable, but since the 30nm wires have more absorption peaks in the energy range of the experiment, making a conclusion on the degree of the fit is more difficult.

Another interesting effect is that the non-parabolic bands cause the minimum energy difference between two subbands to be slightly away from the band edges, as shown in Fig. 5-21. Therefore, for one inter-subband transition, there can be two energies with singularities in the joint density of states, one at the subband separation at the band edge, and the other at the minimum energy separation between the subbands away from the band edge (see Fig. 5-21). The two singularities in

the joint density of states cause two peaks to occur in the absorption spectra for each inter-subband transition. The two asymmetric peaks have their tails facing each other, and therefore one has positive dispersion and the other has negative dispersion. Depending on the position of the Fermi level relative to the subband edges, either the low energy, the high energy, or both absorption peaks will be observed. The simulated absorption spectrum of an isolated transition, as shown in the insert of Fig. 5-21, exhibits this double absorption peak effect, but when the absorption from all transitions are considered, as in Fig. 5-18, this effect is washed out. The double absorption peak resulting from the non-parabolic bands in bismuth may not be observed in wires with a significant electron population, since the many-body depolarization effect can modify the line shape resulting from non-parabolic bands [82].

The modeled intersubband absorption results for $\langle 012 \rangle$ bismuth nanowires with diameters 35, 40, 42.5, and 45 nm at 293 K are shown in Fig. 5-22. As the wire diameter is decreased, more absorption peaks appear with decreasing intensity. From this figure, we also observe an increase in the energy of the peak positions as the wire diameter is decreased. This increase in energy with decreasing wire diameter is consistent with that observed experimentally for the large peak at 1000 cm^{-1}. However, the magnitude of the calculated energy shift is much larger than that observed experimentally. For example, a decrease of the wire diameter from 80 to 35 nm increases the energy of intersubband transitions by ~ 900 cm^{-1} while the measured energy increase of the ~ 1000 cm^{-1} peak is only 65 cm^{-1}. The diameter dependence of the smaller intensity peaks was not determined, since they are masked by the absorption in the alumina for bismuth nanowires inside an alumina template, and since the diameter of free-standing wires are not accurately known.

Several other dependencies also do not agree with the measured data for the large absorption peak. As the Fermi energy, E_f, is increased, by adding n-type tellurium dopants, the absorption from intersubband transitions should increase significantly. This effect is demonstrated in the simulated absorption curves resulting from intersubband transitions in $45nm$ diameter bismuth nanowires shown in Fig.5-23. Results

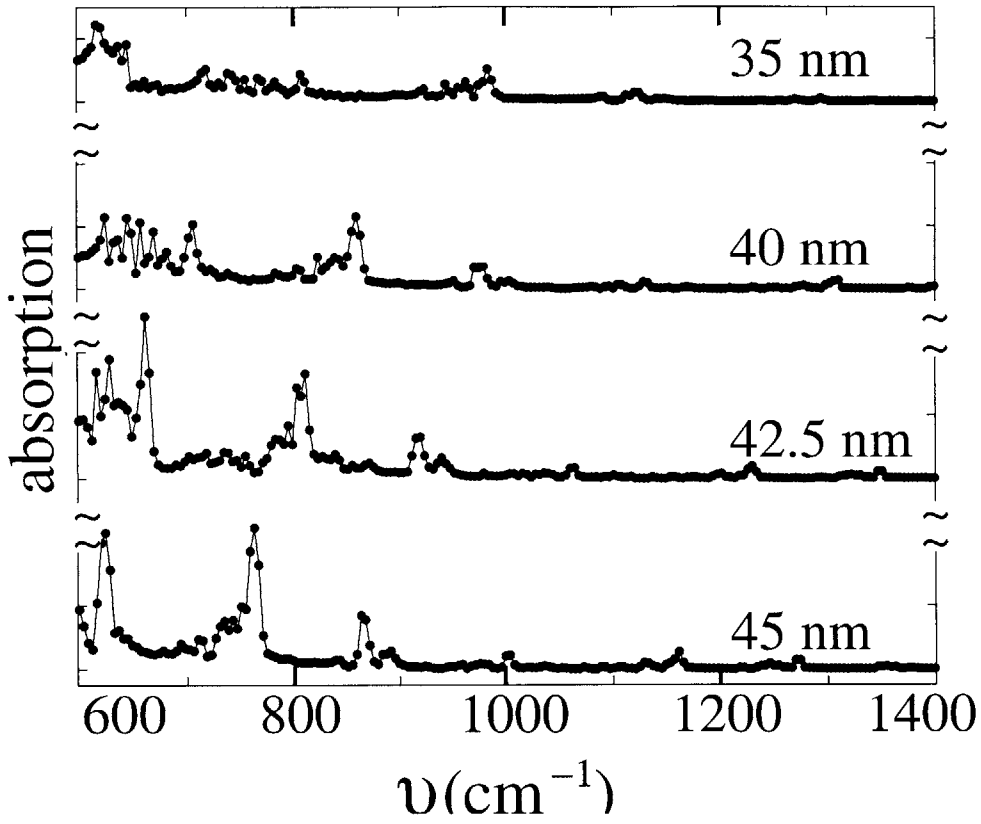

Figure 5-22: Simulated wavenumber dependence of the inter-subband absorption at 293 K for 45, 42.5, 40, and 35 nm diameter wires. As the wire diameter decreases, the number of absorption peaks increases and the absorption peak intensities decrease.

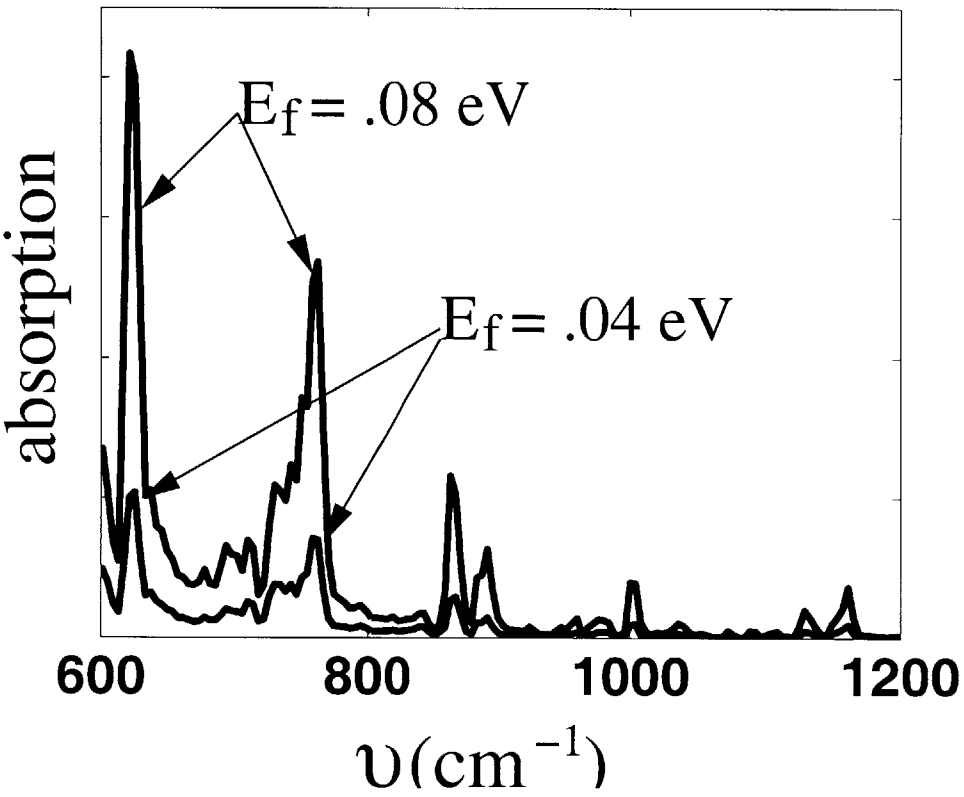

Figure 5-23: Simulated wavenumber dependence of the inter-subband absorption at 293 K for 45 diameter wires with Fermi energies, E_f, of $0.04eV$ and $0.08eV$ relative to the energy of the center of the L-point, the midpoint between the L-point valence and conduction bands. As the Fermi energy, E_f, increases, the absorption intensity increases, since the occupation of the initial subband states increases.

for nanowires with Fermi energies of $0.04eV$ and $0.08eV$ are simulated. As the Fermi energy is increased, the simulated absorption increases, since the absorption of intersubband transitions is limited by the number of free carriers in the conduction band. The trend is contrary to the observed doping dependence.

The temperature dependence is also different from that measured. As the temperature is decreased, the mass of the L-point carriers decreases, so the energy separation of the subbands is increased, thus leading to an increase in energy (wavenumber) for all the peaks as the temperature is decreased.

In summary, the intersubband absorption of bismuth nanowires is modeled and compared to experimental results. Simulations of the optical absorption resulting from intersubband transitions predict the energy of the experimentally measured absorption peaks in $\sim$ 45 and $\sim$ $30nm$ wires. In addition, this model explains the polarization dependence of the absorption and the qualitative diameter dependence of the absorption peak energy [70, 83]. However, some aspects of the absorption curve remain unexplained by intersubband absorption theory. Firstly, although the energy of the experimentally measured absorption peak at around $1000\,\mathrm{cm}^{-1}$ increases with decreasing wire diameter, as predicted by the intersubband model for intersubband transitions, it does not increase as rapidly as expected. Secondly, the relative intensities of the absorption peaks in the free standing wires are different from those predicted by intersubband theory [84]. In particular, the absorption peak at around $1000\,\mathrm{cm}^{-1}$ is much more intense in the experimentally measured absorption than in the simulated intersubband absorption [84]. Thirdly, the predicted spectral shape is different from that predicted on the basis of purely intersubband absorption. Fourthly, the predicted dependence on doping is opposite to that experimentally observed. Finally, a very large temperature dependence is expected for intersubband transitions, but the large absorption peak at $\sim$ 1000 cm^{-1} shows very little temperature dependence. Therefore, we conclude that the smaller intensity absorption peaks are likely to result from electronic intersubband transitions, but the dominate absorption probably results from another absorption mechanism, as discussed further in sections 5.3.3 and 5.3.4.

5.3.3 INTERBAND THEORY

For interband transitions, transitions between the n^{th} valence subband to the n^{th} conduction subband are allowed. From equation 2.9, the coupling between the valence band (v) and conduction band (c), as expressed by the square of the momentum matrix element $|\langle v|p|c\rangle|^2 = P^2$, is related to the effective mass (m^*) and the bandgap (E_g) by the following relation:

$$\frac{1}{m^*} = 2\frac{P^2}{E_g m_0} \tag{5.8}$$

where m_0 is the free electron mass. In the 2-band model, the valence to conduction band coupling, P^2, is assumed to be constant and not dependent on the momentum, k, so that even though different subbands have different effective masses and band gaps, the coupling between the valence and conduction bands remains the same. The higher subbands have a larger band gap due to quantum confinement, and therefore have a correspondingly larger effective mass.

Since, P^2 does not depend on the subband number, at the band edge ($k = 0$), the momentum matrix element for the different subband states is the same. In other words, under the 2-band approximation, the valence subband 1 couples to conduction subband 1 as strongly as valence subband 10 couples to conduction subband 10. Therefore, when calculating the relative absorption strengths of different interband transitions or the shape of the absorption spectra from interband transitions, the matrix element need not be considered, under the 2-band approximation.

The simulation results of the first 10 interband transitions are shown in Fig. 5-24 for both 45nm and 41.5nm diameter wires. Included in Fig. 5-24 are dashed lines (arrows) indicating the frequencies for the absorption peaks that are experimentally observed, as shown in the fit to the experimental spectra in Fig. 4-9. The absorption peak values observed in the ~ 45 nm diameter free-standing wires are included on the figure for comparison. The calculated spectral shape as well as the peak energies of the absorption resulting from the interband absorption process in bismuth nanowires do not agree well with the experimentally measured spectra in the ~ 45 nm diameter

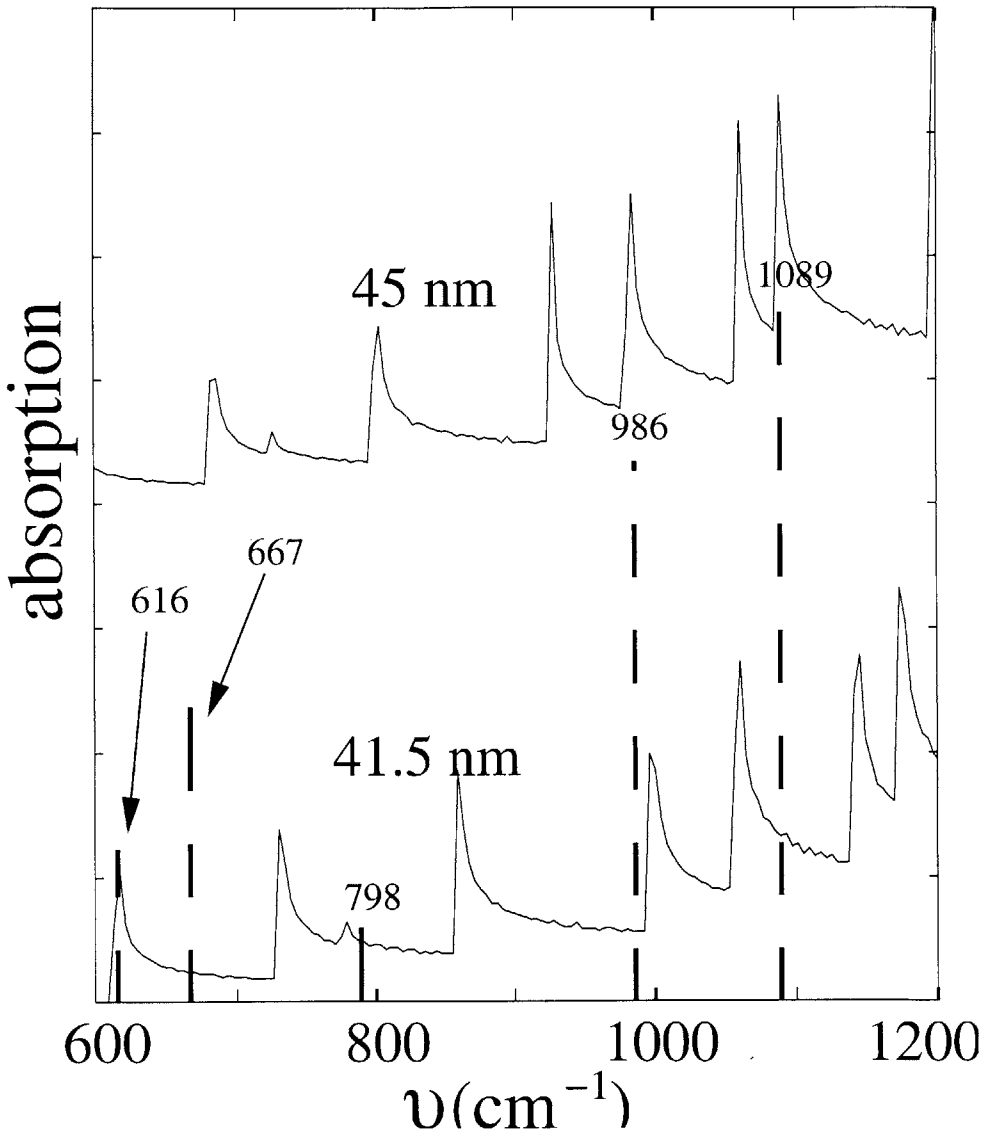

Figure 5-24: The calculated optical absorption at 293 K resulting from a direct interband transition for 41.5 and 45 nm Bi nanowires oriented along the ⟨012⟩ crystalline direction. The energies and relative intensities of the experimental absorption peaks are shown by the dashed lines.

free-standing wires. While the diameter of the simulated wires is varied for the range of experimentally possible wire diameters, the calculated absorption spectra remains significantly different from that of the measured absorption spectra. In addition, since the conduction and valence bands do not track each other, the joint density of states for these transitions are expected to be smaller than inter-subband or indirect L-T transitions where the subbands do track each other approximately. Furthermore the polarization, diameter, and temperature dependences do not agree with the measured data. The simulations of the optical absorption from interband transitions do predict an increase in the peak energy with decreasing wire diameter, but this increase is an order of magnitude too large. As the temperature is decreased, the bandgap and the effective mass of the free carriers at the L-point decrease in bismuth. A decrease in bandgap alone would result in a decrease in the energy of the absorption, while the decrease in the effective mass of the free carriers leads to increased quantum confinement effects and hence leads to an increase in the energy of the absorption. For wires with diameter $\sim 40nm$, the change in the effective mass is the dominant factor and the energy of the absorption peak should increase as the temperature is decreased. However, very little temperature dependence is observed in the measured spectra.

For all these reasons, I do not believe that interband transitions contribute significantly to the measured absorption spectra for bismuth nanowires.

5.3.4 INDIRECT INTERBAND L-T TRANSITION

The wire diameter and polarization dependences, as well as the energy of the absorption peak at ~ 1000 cm^{-1}, strongly suggest that this absorption is from intersubband transitions, as discussed in section 5.3.2. However, the absorption resulting from indirect intersubband transitions can, in principle, also explain a large absorption peak at ~ 1000 cm^{-1}. Often indirect transitions are weaker than direct transitions, since a phonon is required for conservation of momentum. However, since the Debye temperature of bismuth [9] is only 86.5-112 K, many phonons are available at room temperature to contribute to an indirect transition in a phonon absorption process.

Since bulk bismuth is a semimetal, the Fermi energy crosses the T-point valence band, creating many unoccupied electronic states (holes). The L-point valence band, however, is 90 meV below the Fermi energy and is therefore mostly filled at room temperature, see section 2.1. Since the two types of valence bands track each other approximately (have similar shifts in energy with varying momentum), like in the case of intersubband transitions, and since the initial L-point valence band is fully occupied while the final T-point valence band is partially unoccupied, we expect a strong indirect L-T-point absorption over a narrow wavenumber range.

Both the L and T-point valence bands exhibit significant quantum confinement for the bismuth nanowire diameters used in this study. Since the L-point carriers have in general a smaller effective mass than the T-point carriers, the subbands at the L-point are separated by a larger energy difference than those at the T-point. In other words, with decreasing wire diameter, both the L and T point valence bands move down in energy, but the L-point valence bands move down at a faster rate than the T-point valence bands. The energy of the indirect transition from the L to the T-point valence bands is therefore expected to increase with decreasing wire diameter, but not as rapidly as for a direct interband or an intersubband transition. Experimental measurements show[70] that when the wire diameter is decreased from 80 to 35 nm, the energy of the absorption peak increases by 65 cm^{-1}. The theory of intersubband transitions in bismuth nanowires predicts an increase in the energy of the absorption peak measured in wavenumbers by ~ 900 cm^{-1} at room temperature for a wire diameter change from 80 to 35 nm. However, since the energy shift of the absorption peak from an indirect L-T point valence band transition is determined mainly by the difference between the two effective masses and not so much by the values of the effective masses themselves, this shift with wire diameter is much less for the indirect L-T transition than for the direct L-point transition, and the L-T transition energy fits much better with the experimental measurements on the wire diameter dependence of the peak energy. As the wire diameter decreases from 70 to 35 nm, the simulations for the indirect transition predict a modest increase in the absorption peak energy by only $\sim$ 100 cm^{-1}, close to the experimentally observed

shift, as discussed below.

The optical absorption at $\sim 1000\ \mathrm{cm}^{-1}$ has a very strong polarization dependence as discussed in section 5.2.1 [70]. When light is polarized perpendicular to the wire axis, the absorption vs. energy has a strong sharp feature at $\sim 1000\ \mathrm{cm}^{-1}$. As the polarization angle is rotated away from the normal to the wire axis, the intensity of this feature decreases, and eventually, for light polarized parallel to the wire axis, this absorption peak disappears [70]. This polarization trend agrees with the selection rules of intersubband absorption and is one reason why the strong absorption peak at $\sim 1000\ \mathrm{cm}^{-1}$ was initially attributed to an intersubband absorption [70]. However, the polarization dependence can also be explained by an indirect transition enhanced by surface effects [85]. One explanation for why an indirect transition would be enhanced by surface effects is that proposed by Miller *et al.* Miller *et al.* predict an enhancement of indirect transitions at the interface between two materials having a dielectric constant mismatch due to a surface contribution to the optical matrix element [85] given by the following argument.

The optical transition matrix element, M_e, is composed of two terms

$$M_e = < \Psi_{final} | A \bullet \nabla + \nabla \bullet A | \Psi_{initial} > . \tag{5.9}$$

The first term, $< \Psi_{final} | A \bullet \nabla | \Psi_{initial} >$, is used to calculate the optical matrix element in bulk solids. The second term, $< \Psi_{final} | \nabla \bullet A | \Psi_{initial} >$, results from the spacial derivative of the vector potential and in a homogeneous material (for one commonly used gauge of A) this term is zero. In contrast, since the wavelength of light is much larger than the wire diameter, for the gauge of A that gives a zero $\nabla \bullet A$ value for a bulk material, a non-zero value results at the interface between two materials with different dielectric constants, for example at the bismuth / alumina interface in our nanowires [85, 86]. Furthermore, since the dielectric function does not instantaneously change at the interface, but instead changes throughout a distance, d, and since the wire diameter is small, this change could occur throughout most of the wire radius.

In the case of a large surface interface area, as in bismuth nanowires, the surface

matrix element term cannot be ignored. Miller *et al.* found experimentally that the surface contribution to the matrix element enhances the indirect transition in their gold samples [85]. In another study, Enders and Schuchardt observed an increase in the amplitude of the dielectric function of bismuth with the addition of antimony [87]. They attributed the increase in the dielectric function to an enhanced indirect transition in bismuth resulting from the short-range scattering potential of the Sb dopant sites. In bismuth nanowires, since bismuth has a significant index of refraction ($n = 2.6$ at 1000 cm^{-1} [12]), both bismuth / alumina ($n = 1.7$) and bismuth / air ($n = 1$) have significant dielectric constant mismatches, and therefore the surface contribution to the matrix element is significant.

If the strong optical absorption at ~ 1000 cm^{-1} is a result of the surface enhancement of the optical matrix element, this absorption should have a large polarization dependence. When the light is polarized such that the electric field crosses an interface perpendicular to the wire axis, the surface term is non-zero. However, when the electric field of the incident light is parallel to the wire axis, the surface term should be zero, since the electric field does not cross a bismuth / air(or alumina) boundary.

This argument has additional credibility since, when the reflection of a roughed up bulk bismuth sample was measured, it had a feature at around ~ 1000 cm^{-1} (not shown). In addition, the thin film of bismuth that was used to provide a background spectra when fitting the spectra to interband transitions [83], shown in Fig. 5-7 A), also shows a shallow feature in the transmission at ~ 1000 cm^{-1}, but it is broader and weaker. The feature in the thin film bulk bismuth sample likely results from some small surface roughness inherent in the thin film fabrication. Furthermore, even though $200\,nm$ diameter bismuth wires are too large to show significant quantum confinement, they still show an absorption peak (as evident from a peak in K) at 965 cm^{-1}, see Fig. 5-6. The $200\,nm$ diameter wires and their absorption peak at 965 cm^{-1} are, therefore, characteristic of crystalline bulk (not quantum confined) bismuth with a large surface area. Since rough bulk samples, thin films, and $200\,nm$ diameter wires all show an absorption peak around ~ 1000 cm^{-1}, this strong absorption peak likely results from the indirect L to T-point transition and not from intersubband

transitions, in agreement with the argument discussed above regarding the diameter dependence of the strong sharp absorption peak.

Theory and numerical solutions of the optical absorption from an L-T-point indirect electronic transition

Model calculations are presented in order to understand the indirect L-T transition in bismuth nanowires, and hence to gain insight into the mechanism responsible for the absorption peak(s) observed in the experimental data. For this work, a phonon assisted process is assumed, although one possibility is that the indirect transition is assisted by a surface defect at the bismuth-oxide interface. Since a surface defect is localized in real space, it is distributed in momentum space, and therefore a phonon might not be required if the surface state couples the initial and final states.

A photon can excite an electron to an unfilled higher energy state if the energy of the photon exactly equals the energy difference between the final and the initial states (plus or minus the energy of a phonon in an indirect process) and if momentum is conserved. The photon absorption from this process can be measured by energy-dependent optical absorption spectra. In order to conserve momentum, in an indirect transition, a phonon with momentum equal to the momentum difference between the final and initial states must be absorbed (or emitted). The optical absorption coefficient, α_{L-T}, resulting from an indirect electronic excitation from the L-point valence band to the T-point valence band in a Bi nanowire as a function of photon energy, $\hbar\omega$, is given by

$$\begin{aligned} \alpha_{L-T}(\omega) \quad & \propto \textstyle\sum_{p=1,2,3} \sum_n \sum_m \int dk_n \int dk_m \\ \times \quad & N_{ph}(E) \times M_e(n,m)^2 \times [f(E_n(k_n)) - f(E_m(k_m))] \\ \times \quad & \delta(E_m(k_m) - E_n(k_n) \pm E_{phonon} - \hbar\omega) \times \delta(k_m - k_n \pm k_{phonon}) \end{aligned} \tag{5.10}$$

where ω is the frequency of the incident light, p is 1, 2, *or* 3 corresponding to the

three L-point hole pockets, n and m are the L-point and T-point subband indices, respectively, k_n and k_m are the wave vectors of the L and T-point valence band states in the direction of the wire axis, N_{ph} is the phonon population described by the Planck distribution function, $M_e(n,m)$ is the momentum matrix element coupling strength between the initial, n, and final, m, subbands, $f(E_n)$ and $f(E_m)$ are the Fermi-Dirac distribution functions for the states n and m, respectively, and E_n and E_m are the corresponding energies. In Eq. (5.10), the momentum of the incident photon is ignored, since it is much less than the momentum of the phonon, and the electron-phonon coupling strength is for simplicity assumed to be constant.

In our calculations, the acoustic phonons are modeled using the Debye model so that the velocity of sound, c_s, is taken as a constant of 2.54×10^3 m/s [12]. The simulation results are found to be insensitive to the velocity of sound. Since the L-point bands are strongly coupled, the Lax 2-band model for non-parabolic coupled bands is used to describe the dispersion relations [81]. Since the L-point electronic bands are extremely anisotropic and show strong non-parabolic effects, the calculation of the wave functions is done numerically. The Fermi energy as well as the energy levels and wave functions for the first 50 subbands are found by a modified version of a previously published model of the electronic structure [14], the modified version taking into account the non-parabolic dispersion relations of the subbands in calculating the Fermi energy. The model takes as variables, the wire crystallographic orientation along the wire axis, the wire diameter, and the temperature. For all calculations in this work, unless otherwise stated, the wires are assumed to be undoped, so that the Fermi energy is set to ensure charge neutrality.

The matrix element, $M_e(n,m)$, is calculated by assuming a penetration depth, d_{pd}, of the surface component of the matrix element in Eq. 5.9 and by calculating the integral

$$M_e(n,m) = \int \psi_n[exp(-\frac{(1-r)}{d_{pd}}) + exp(-\frac{1}{d_{pd}})exp(-\frac{r}{d_{pd}})]\psi_m \, dr d\theta \qquad (5.11)$$

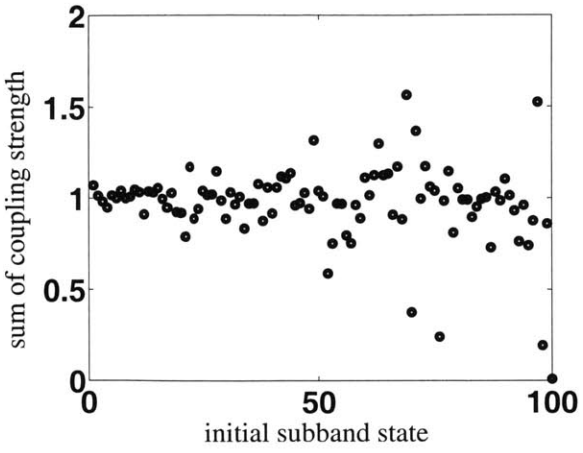

Figure 5-25: The sum of the matrix elements, $M_e(n,m)$, for the first 100 initial states, n, to the first 100 final states, m.

where the integral is taken over the cross sectional area of the wire, $dr\,d\theta$, and ψ_n and ψ_m are the wavefunctions of states n and m respectively. Various matrix elements were tried, including coupling of the initial and final states through an intermediate state. All methods gave very similar results. Hence, the simplest version is presented here.

Figure 5-25 shows the sum of the matrix elements from the first 100 initial L-point valence subband states to the first 100 final T-point subband states, for the case where the penetration depth, d_{pd}, is much larger than the wire diameter. The f-sum rule holds well for the subband states used in our simulations, i.e., the first 20 subbands. However, the f-sum rule doesn't hold as well for the higher energy subbands due to limitations of the numerical method used to solve for the wavefunctions.

The penetration depth, d_{pd}, of the surface matrix element is varied to better fit the experimental data. When the penetration depth is large compared to the wire diameters, Eq. 5.11 reduces to a spatial overlap of the wavefunctions. Unlike for the case of intersubband transitions [83], when the spacial overlap as the matrix element, one initial T-point subband state usually couples strongly to only one (or at the most three) L-point subband state(s). In addition, because of the differences in the effective mass tensors at the T and L points, the lower order T-point subbands couple more strongly to an L-point subband than higher order T-point subbands couple to

an L-point subband. In other words, the first T-point subband will couple strongly with only the first L-point subband, while the 10^{th} T-point subband will couple most strongly with the 10^{th} L-point subband, and the coupling between the first states will be stronger than between the 10^{th} states.

As the penetration depth of the surface component of the matrix element, d_{pd}, decreases, each T-point subband state couples to more L-point subbands. In addition, for small decay lengths, higher order states couple more strongly than the lower order states since their wavefunctions are on average closer to the boundary of the wire. Both these trends lead to a broader absorption peak. In addition, as the decay length is decreased, the smaller wire diameter wires absorb more strongly than the larger diameter wires, since they have a larger surface area to volume ratio. Although the smaller the diameter of the wires, the less volume an individual wire occupies, for a given sample size, the smaller the wire the more wires are simultaneously measured, and so the volume measured is roughly independent of wire diameter. Hence, an increase in the surface area to volume ratio increases the absorption intensity.

Even for the limiting case of $d_{pd} >> d_w$, where d_w is the wire diameter, the experimental spectra have a narrower absorption peak than the simulated spectra. This discrepancy could indicate that the higher order subbands are not well defined in the wires either because of limits in the infinite barrier approximation or because of surface roughness on the wires. The discrepancy could also result from limitations of the 2-band model assumed in this calculation. Instead of fitting d_{pd} to the line width of the spectrum, d_{pd} is fit to the ratio of the intensities of the experimentally observed absorption peak for 35nm and 60-80nm diameter wires [70]. Using this method, d_{pd} is found to be $\sim 15nm$.

In order to determine the dependence of the peak width on the number of subbands that were included in the simulation, the matrix element was multiplied by a decaying exponential function with a dependence on the subband numbers of the initial, n, and the final, m, states

$$M_e(n,m) \rightarrow M_e(n,m)\ exp(-s\,n)\ exp(-s\,m) \tag{5.12}$$

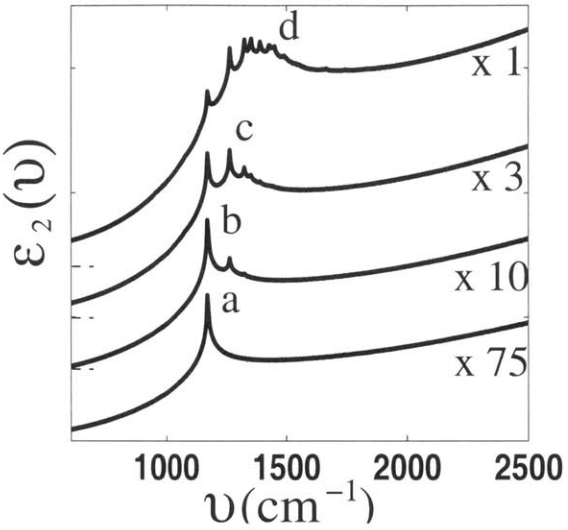

Figure 5-26: The calculated $\epsilon_2(\nu)$ resulting from electronic transitions from pocket A at the L-point to the T-point, assuming a phonon absorption process. The matrix elements, $M_e(n,m)$ are scaled by Eq. 5.12 with s set to 1, 0.5, 0.25, and 0.1 for graphs a, b, c, and d respectively. The curves b, c, and d are offset with respect to the dotted lines and are multiplied by 75, 10, and 3, respectively.

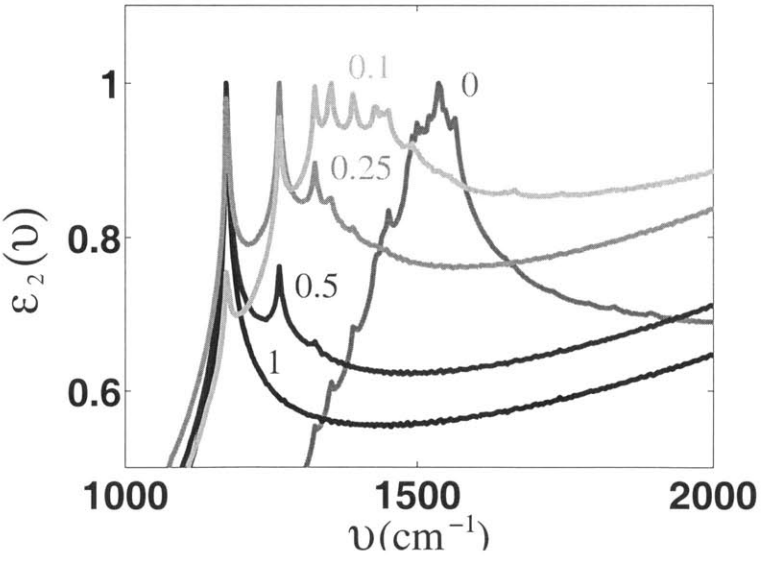

Figure 5-27: The calculated $\epsilon_2(\nu)$ resulting from electronic transitions from pocket A at the L-point to the T-point, assuming a phonon absorption process. The matrix elements, $M_e(n,m)$ are scaled by Eq. 5.12 with s set to 1, 0.5, 0.25, 0.1, and 0. The curves are normalized to their absorption peak intensity.

where s is a fitting coefficient. The curves a, b, c, and d in Fig. 5-26 show the calculated $\epsilon_2(\nu)$ with s chosen to be equal to 1, 0.5, 0.25, and 0.1 respectively. The spectra show contributions to the absorption, and hence ϵ_2, resulting from electrons only in pocket A, see Fig.2-1 (a), and are only for the phonon absorption process (simulations of the phonon emission process would result in similarly shaped absorption spectra at an energy 160 cm^{-1} higher) as discussed below. The larger the value of s, the more the lower order subbands dominate the absorption spectra. When the lower order subbands dominate the absorption spectra, the peak in ϵ_2 is narrower and occurs at a lower energy (1174 cm^{-1} for $s = 1$ vs. 1380 cm^{-1} for $s = 0.1$ and 1540 cm^{-1} for $s = 0$) than when higher order subbands also contribute significantly to the spectra. The dependence of the peak width and the energy of the peak in ϵ_2 are best observed in Fig.5-27, which shows the simulated $\epsilon_2(\nu)$ for various values of s, where $\epsilon_2(\nu)$ is normalized to the ϵ_2 peak intensity. In this thesis, for all the spectra that are presented, except those in Figs. 5-26 and 5-27, the approximation $s = 0$ was taken, in order to minimize the number of fitting parameters and simplify the data analysis. Therefore, the lower order subbands are not favored in the present calculation.

Unlike the case of intersubband transitions [83] even with $s = 0$, see section 5.3.2, the higher-order subband states do not contribute significantly to the absorption coefficient. For example, in a 35nm diameter wire, the 20^{th} T-point valence band is more than 60 meV below the Fermi energy. Since an empty state near the T-point is required for the indirect absorption, and since the higher level subbands are mostly filled, only the first 20 subbands at the T-point are considered in the calculation. Since higher level subbands at the L-point couple only weakly to the first 20 subbands at the T-point, only the first 20 subbands at the L-point are considered. In addition, surface conditions and possibly limitations to the 2-band model, likely, limit the number of well defined subbands. The contribution to the optical absorption from electronic transitions between the first 15 T-point and the first 15 L-point subbands of pocket A in 35 nm diameter bismuth wires at $293K$ is shown in Fig. 5-28 (a). Only those transitions with significant coupling strength are shown. The figure shows that after the first 9 subband transitions, the intensity of the absorption peaks sharply

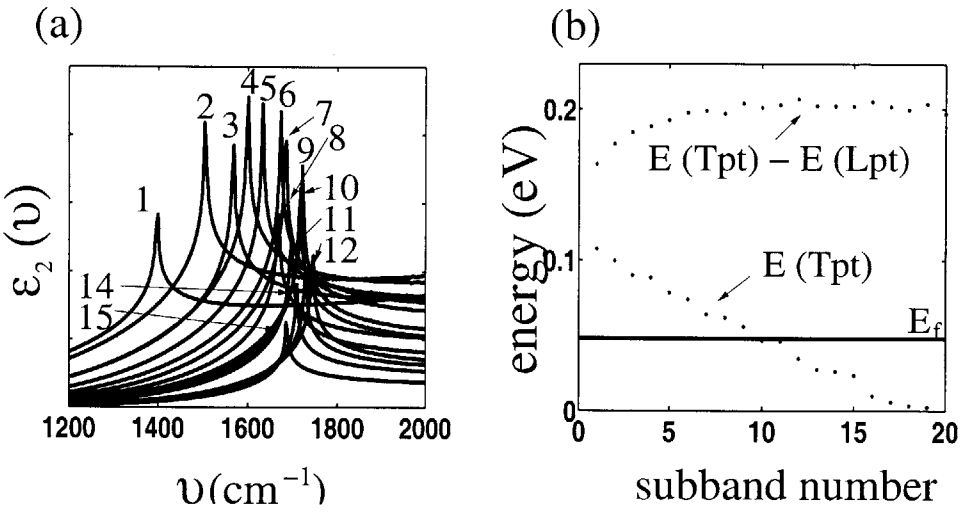

Figure 5-28: (a) The simulated optical absorption from transitions from the first 15 T-point subbands to their corresponding L-point subbands for one pocket of an undoped, $35\,nm$ diameter bismuth nanowire at $293K$. As the T-point subband index is increased, the absorption intensity decreases, since the higher subbands at the T-point have fewer empty states to which an electron from the L-point can be excited. The energy of the absorption peak increases rapidly with increasing subband number until about the 10^{th} state, at which point it levels off and eventually slowly decreases. (b) The energy difference between the band edges of the L and T point valence bands as a function of state number, the Fermi energy, and the energy of the T-point band edge as a function of state number.

decreases.

Fig. 5-28 (b) shows the energy difference of the band edges as a function of subband number for pocket A. Since the L-point and T-point masses are different, the energy difference between the L and T-point band edges also varies as the subband number is varied. Each transition therefore has a slightly different absorption peak wavenumber, thereby contributing to the line-width of the peak. Since the L-point effective mass increases with energy due to non-parabolic effects, the effective masses (in the confined direction) of the L-point subbands also increase with increasing subband index. When the effective mass (in the confined directions) of the L-point equals the effective mass of the T-point, the two bands decrease in energy at the same rate as the subband number is increased. Therefore, at this point, many transitions have the same energy difference between them, thus resulting in a large absorption peak. From Fig. 5-28 (b) we see that for states 8 - 20, the energy difference between the subbands is fairly constant, and thus the absorption peaks from these subbands all contribute to the observed optical absorption at nearly the same energy. The transitions from subbands where the effective masses of the L and T-points are different contribute to the line width of the absorption spectra. Hence, the energy of the absorption peak is near to the energy difference of the L and T point subbands with the same band edge effective mass.

The contributions to the absorption spectra associated with the indirect transition from the three L-point pockets (one A pocket and two B pockets) to the T-point hole pocket are shown in Fig. 5-29. For $\langle 012 \rangle$ aligned Bi wires (such as our wires), two of the three electron pockets are degenerate. The two degenerate pockets are labeled "pocket B" in Fig. 5-29, and the third non-degenerate electron pocket is labeled "pocket A". For each pocket, the absorption spectra has two distinctive absorption peaks, one (at higher energy) for the emission of a phonon and one (at lower energy) for the absorption of a phonon. The peaks for each process are shown separately as well as the total contribution to the absorption from both processes. Pocket A has a larger intensity absorption peak than pocket B, since the effective mass components in the confined directions of this pocket are better matched to those at the T-point. The

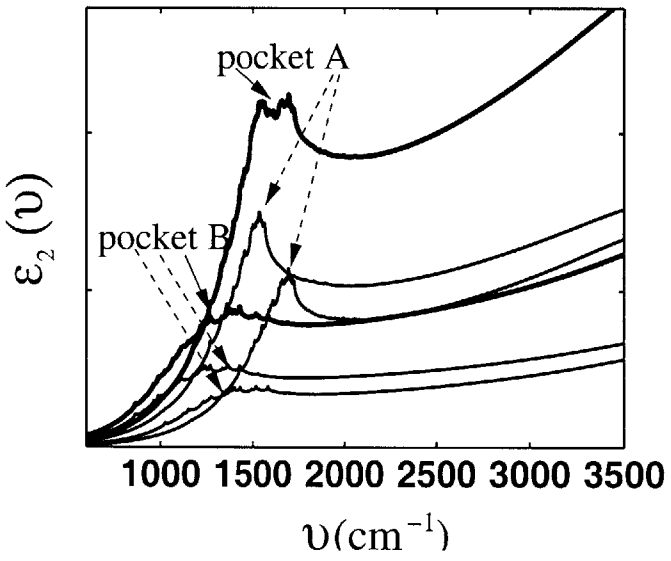

Figure 5-29: The calculated absorption spectra from the non-degenerate hole pocket A and the doubly degenerate hole pocket B at the L-point, see Fig. 2-1, to the T point valence band of a 45 nm diameter ⟨012⟩ aligned bismuth nanowire at room temperature. The absorption is plotted in terms of the wavenumber dependence of the dielectric function $\epsilon_2(\nu)$, and the wavenumber on the x-axis is expressed in terms of the reciprocal wavelength. Each pocket has two absorption peaks, one when a phonon is emitted (at higher ν) and one when a phonon is absorbed (at lower ν). The total absorption (solid arrows) as well as the absorption assuming just phonon emission or just phonon absorption (dotted line arrows) are shown.

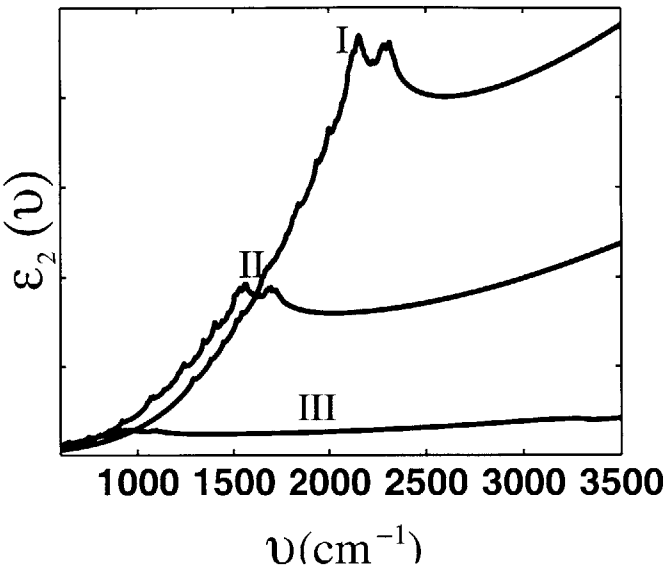

Figure 5-30: The simulated absorption spectra including all three pockets of the indirect L-T-point transition in 30 nm diameter bismuth nanowires at room temperature shown for three values of the band overlap energies for bulk bismuth, at 300K. Curves I, II, and III are for L-T band overlap energies of 172 (1387), 98 (790), and 24(194) $meV(\mathrm{cm}^{-1})$, respectively. The reported band overlap energy in bismuth at room temperature is $98meV$ (790 cm^{-1}) [2].

more closely the effective mass components in the confined directions of the initial and final states are matched, the greater the number of subbands that contribute to the absorption at the same energy, and hence the absorption peak is enhanced.

Since the electronic band parameters at room temperature are not accurately known, we considered the sensitivity of our model to variations of the band parameters. First we consider variation of the band overlap and then variation of the effective mass components. Figure 5-30 shows the calculated absorption spectra with varying values of the bulk bismuth band overlap energy of the L and T-points used in the simulations. Curve II is for the measured band overlap of $98meV$ (790 cm^{-1}) for bulk bismuth [2], and curves I and III are for a band overlap of $98 + 74meV$ (1387 cm^{-1}) and $98 - 74meV$ (194 cm^{-1}) respectively. Values of the band overlap were chosen so that the change in the absorption spectra was significant, and so that the lower band overlap energy of $24meV$ resulted in an absorption peak near the energy of the

observed absorption peak, as discussed below. An increase (decrease) in the band overlap energy results in an up-shifted (down-shifted) absorption peak energy by the same amount.

The energy of the absorption peak is not only sensitive to the energy overlap of the L and T-point bands, but is also sensitive to the ratio of the effective masses of the L and T-point pockets. When the T-point hole mass is decreased, the energy at which the L-point mass equals the T-point mass also decreases. Therefore, when the T-point mass decreases, the energy of the absorption peak downshifts. The simulations show that a decrease in the T-point hole effective mass by 10% results in a down shift of the absorption spectra by ~ 75 cm^{-1}. Likewise, when the hole mass at the L-point band edge decreases, the energy at with the L-point mass equals the T-point mass increases, and the absorption peak occurs at a higher photon energy. A decrease in the L-point hole mass by 10% results in an up-shift of the absorption spectra by ~ 90 cm^{-1}. When both the electron (T-point) and hole (L-point) masses are increased, the effects cancel out and the absorption peak remains relatively constant.

Comparison between model calculations and experimental results

Figure 5-31 (a) shows the measured and Fig. 5-31 (b) the simulated optical transmission as a function of wavenumber of bismuth nanowires. The simulated absorption includes the absorption from all three L-point carrier pockets and is for a 45 nm diameter wire. The measured absorption is from a ~ 45 nm diameter, undoped, wire, as also shown in Fig. 5-6. The transmission profiles for the measured and simulated curves are very similar. As the light's frequency is increased, the experimental / simulated transmission drops sharply and reaches a local minimum at around $1100\,cm^{-1}$ / $1500\,cm^{-1}$. The transmission then slightly increases, and finally steadily decays for the rest of the measured wavenumber range. At $4000\,cm^{-1}$, the transmission is less than 10% of the transmission at $650\,cm^{-1}$. The measured transmission drops slightly faster and has slightly sharper features than the simulated curve. The differences in the magnitude of the transmission likely result from the fact that only optical absorption from an indirect transition is simulated in (b), while in the experimental measurements, (a),

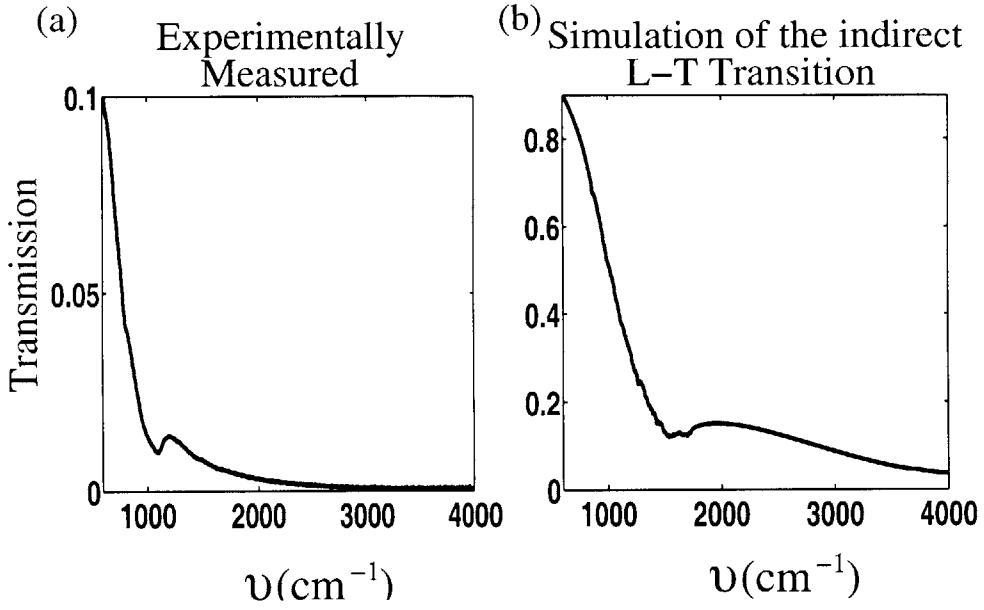

Figure 5-31: (a) The measured optical transmission as a function of wavenumber of free-standing bismuth nanowires. (b) The simulated optical transmission as a function of wavenumber resulting from an indirect L-T transition in bismuth nanowires with a diameter of $45nm$. Note that the minimum transmission in the experimental spectra is at ~ 1100 cm^{-1}, and in the simulated spectra is at ~ 1500 cm^{-1}. The differences in the magnitude of the transmission likely result from the fact that only optical absorption from an indirect transition is simulated in (b), while in the experimental measurements, (a), many absorption and scattering mechanisms are likely to be present.

likely many absorption and scattering mechanisms are present.

Although the simulated and measured spectra are similar, the local minimum in the transmission, which corresponds to a peak in the optical absorption, occurs at a higher photon energy in the simulated spectra than in the experimentally measured spectra. The transmission minimum in the simulated spectra occurs at $\sim 1520 cm^{-1}$ and in the measured spectra at $1100 cm^{-1}$. This difference may result from approximations used in this calculation, inaccurate values of either the L or T point effective masses, or inaccurate value of the band overlap energy of bulk bismuth at room temperature. If the L-point effective mass tensor is taken to be larger or the T-point hole mass tensor slightly smaller than the literature values, the wavenumber of the simulated absorption peak will decrease. The wavenumber of the simulated absorption peak will also decrease if the band overlap used in the simulations is decreased, see Fig. 5-30. In order for the band overlap alone to explain the discrepancies between the simulated and experimental spectra, the band overlap would need to be $24meV$ compared to the measured value of $98meV$ at room temperature and $33meV$ at 80 K [2]. Another possible explanation for the discrepancy is that the Lax 2-band model may not completely hold for the energies contributing to the absorption spectra (up to 0.25 eV below the L-point mid-gap), because of possible contributions from bands outside of the 2-band model for the L-point valence band.

In addition, the discrepancy between the energy of the simulated and measured absorption peaks may result from taking $s = 0$ in Eq. 5.12. As shown in Fig.5-26, when the lower order subbands dominate the absorption spectra, the energy of the absorption peak decreases, yielding better agreement with experiment. When the lower order subbands dominate the absorption spectra, not only does the energy of the absorption peak decrease, but the spectral width decreases as well, as shown in Figs. 5-26 and 5-27. Both the decrease in energy and the smaller spectral width of the absorption peak are in better agreement with experimental results when a non-zero value of s is used. The spectral width of the simulated absorption spectra results from contributions to the optical absorption from phonon emission and phonon absorption processes, the two types of L-point carrier pockets (A and B), wires with varying

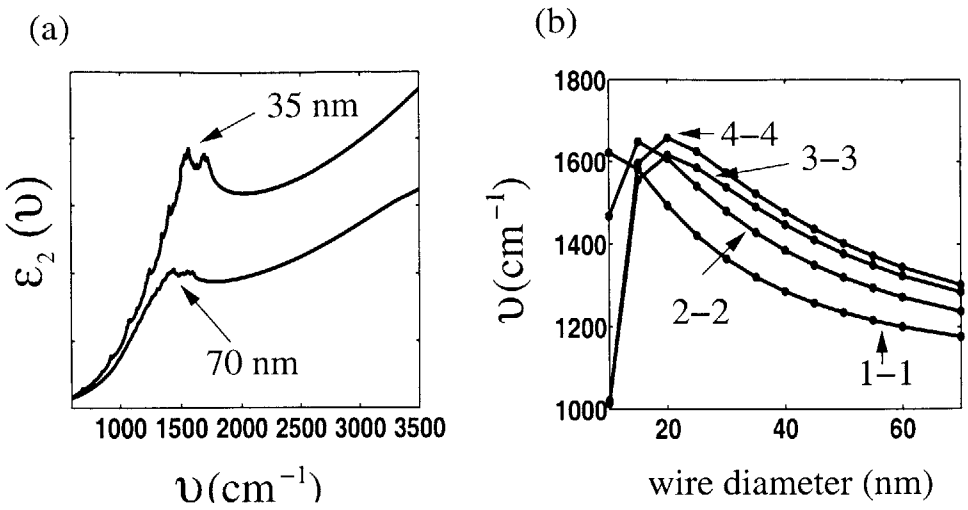

Figure 5-32: (a) The simulated wavenumber dependence of $\epsilon_2(\nu)$ resulting from an indirect L-T transition in bismuth nanowires with a diameter of 70 and 35nm for the wavenumber range of $600 - 4000 cm^{-1}$. The absorption peak in (a) moves from 1420 for the 70 nm wires to $1520 cm^{-1}$ for the 35 nm wires. This shift of $\sim 100\, cm^{-1}$ is to be compared with the experimentally observed shift of $65 cm^{-1}$. (b) The calculated energy difference between the first, second, third, and fourth subbands at the L-point valence band to the first, second, third, and fourth subbands at the T-point valence band.

diameters, and contributions from different subbands. All four of these contributions increase the spectral broadening. Only considering the spectral peak broadening resulting from different subbands, a lower bound of the s value in Eq. 5.12 can be estimated to be 0.35. The rise in ϵ_2 with increasing ν, as measured by the difference between the energy of the peak's maximum ϵ_2 intensity and the energy at which ϵ_2 is half its maximum value, is $\sim 250 cm^{-1}$ for $s < 0.1$ (see Fig.5-27), close to the experimental value of $\sim 300 cm^{-1}$ (see Sec. 5.2.4).

In order to identify the reason for the energy difference in the simulated and measured optical absorption peaks, I recommend more work on the dependencies of the optical absorption on wire diameter and on doping.

Figure 5-32 shows the simulated absorption spectra resulting from an indirect L-T transition in bismuth nanowires with wire diameters of 70 and 35 nm. The energy of the simulated absorption peak shifts from 1420 to $1520\, cm^{-1}$, because of the increased quantum confinement in the smaller diameter nanowires. The magnitude and sign of the shift ($100\, cm^{-1}$) in the simulation agree well with the experimentally

measured shift ($65\,cm^{-1}$) when the wire diameter is varied from 35 nm to 60-80 nm [70]. The energy of the peak in the absorption spectra is approximated by smoothing the simulated absorption spectrum. Fig. 5-32 (b) shows the calculated energy of the first, second, third, and fourth T-point subband edges to the first, second, third, and fourth L-point valence subband edges, respectively. The energy of these transitions increase with decreasing wire diameter, until a wire diameter of around 20nm at which point the energies decrease. For wires smaller than 20nm, the effective mass at the L-point is larger than the effective mass at the T-point, and so the energy of the T-L point transition decreases with decreasing wire diameter.

Interesting, for the wires with the smallest diameter ($\sim 10nm$) measured in this thesis, the energy of absorption peak occurred at an energy lower than that of larger diameter wires (35 and $45nm$). The small diameter wires were anodized at 20V. They had a wire diameter of $\sim 20nm$ inside the alumina template, and therefore a wire diameter estimated to be $6 - 10nm$ when etched from the alumina template. The optical absorption peak of these small diameter free-standing wires occurred at $1000cm^{-1}$, see Fig. 5-14 compared to that of the free-standing $\sim 45nm$ wires at $1100cm^{-1}$, see Fig. 5-6. Possibly, in the $\sim 10nm$ diameter wires, the confined energy of the free electrons at L-point is large enough to result in the L-point effective mass being larger than the T-point effective mass. Therefore, as the wire diameter decreased from $45nm$ to $10nm$, the energy between the L-point valence band and T-point valence band decreased.

In order to further test the identification of the absorption mechanism near $1000cm^{-1}$, the change in the simulated absorption with doping level is compared to Te doped samples, see Fig. 5-9 and section 5-9. As the amount of Te dopant was increased, the absorption intensity decreased. The simulated results also show a decrease in absorption as the doping concentration increases. We can explain this decreased absorption by the predicted increased filling of the T-point valence band as the doping concentration increases, and hence the decrease in the number of final states to which electrons can be excited.

The energy of the absorption peak is slightly sensitive to the Fermi energy at room

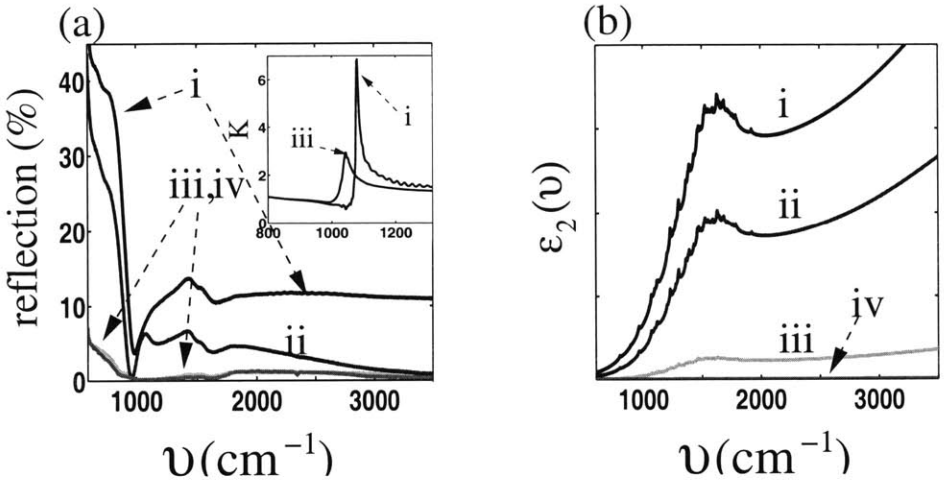

Figure 5-33: (a) The measured wavenumber dependence of the reflection of (i) non-doped, (ii) lightly n-type doped, (iii) medium n-type doped, and (iv) heavily n-type doped bismuth nanowires. The insert shows the calculated wavenumber dependent absorption spectra of the (iii) medium and (i) undoped samples. (b) The simulated wavenumber dependence of $\epsilon_2(\nu)$ resulting from an indirect L-T transition in 40nm diameter bismuth nanowires with (i) no doping, (ii) low n-type doping, (iii) medium n-type doping, and (iv) heavy n-type doping. Arbitrary units are used. In experimental spectra, the reflection is decreased with the addition of n-type dopants, resulting from a decrease in the absorption coefficient. The simulated spectra also show a decrease in the $\epsilon_2(\nu)$ with increasing n-type dopant concentration.

temperature. Since the peaks due to various subbands are separated by much less than the thermal energy, increasing the Fermi energy decreases the hole population in not just one, but in many of the T-point subbands. When the number of holes in a T-point subband is decreased, fewer electrons can be excited from the L-point to that T point subband, and hence the absorption intensity resulting from this subband is quenched. From Fig. 5-28 (b), we see that as the Fermi energy is increased, the T-point subbands contributing to the higher wavenumber absorption are below the Fermi energy and those contributing to the lower wavenumber absorption remain above the Fermi energy. Therefore, when the Fermi energy is slightly increased, the highest energy of the absorption peak downshifts slightly. When the Fermi energy is increased further, so that all the T-point hole subbands are completely submerged below the Fermi energy, no available states for the transition exist, and this absorption mechanism is quenched. The down-shift in the absorption peak energy with an increasing concentration of n-type dopants, as explained above, is not significant in the simulated spectra, since the energy shift is smaller than the spectral width of the simulated absorption peak.

Using Kramers–Kronig relations and a reverse effective medium theory [83], the imaginary part of the index of refraction, K, and of the dielectric function, ϵ_2 as a function of wavenumber for the doped nanowires are calculated from the reflection spectra. Since the transmission of the mediumly and heavily doped samples is significant, this method only gives an approximate measure of the absorption spectra for these samples. The deduced results of $K(\nu)$ are shown for the mediumly and undoped samples in the insert of Fig. 5-33 (a) and the insert of Fig. 5-9. The deduced results for $\epsilon_2(\nu)$ for the undoped, lightly doped, mediumly doped, and heavily doped samples are shown in Fig. 5-10. Compared to the undoped sample, the doped samples have a decreased absorption intensity as expected for an indirect L-point valence band to T-point valence band transition. In addition, increasing the doping levels from undoped to lightly and then to mediumly doped levels slightly decreases ($\sim 40cm^{-1}$) the energy of the peak in the optical absorption spectrum (as seen by either $\epsilon_2(\nu)$ or $K(\nu)$). This trend is qualitatively expected for absorption resulting from an indi-

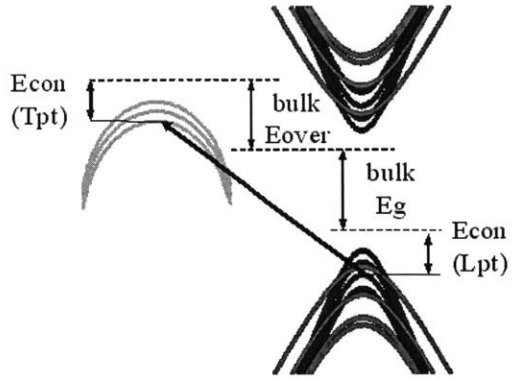

Figure 5-34: A schematic of the energy bands in bismuth nanowires. The energy of a give L-point valence subband to T-point valence subband transition is equal to the bulk band overlap (E_{over}) of the T-point valence band with the L-point conduction band plus the band gap (E_g) of the L-point plus the confinement energy of the L-point (Econ L-pt) subband minus the confinement energy of the T-point subband (Econ T-pt).

rect interband transition as described above, although it is not significant enough to observe in the simulated spectra at room temperature.

Although the shape of the absorption spectra and the polarization, wire diameter, and doping dependencies all are explained by absorption resulting from the L-T-point indirect transition, the temperature dependence of this absorption peak is not well explained. In bismuth, the absorption from many mechanisms (e.g., free carriers, phonons, inter-subband, indirect interband, and direct interband) are all expected to change drastically with temperature. This results from the large temperature dependence of the effective mass, L-point band gap, T-point to L-point band overlap, and the free carrier concentration [1, 2, 13]. However, preliminary results show only slight changes in the optical absorption when the temperature is varied between 400K to 150K. The small observed temperature dependence of the optical absorption is not explained by either intersubband absorption or indirect optical absorption processes.

Two aspects of the weak temperature dependence are unexpected. First, since the band parameters all change with temperature, one would expect that the *energy* of the transition would also change with temperature. Although the absence of a change in energy of the absorption peak is unexpected, it is not necessarily contradictory with

the previously measured temperature dependent band parameters. The measured energy of the absorption peak resulting from an indirect L-point valence band to T-point valence band transition is a function of the bandgap, the band overlap, and the effective mass tensors of both the L and T-points. The simulated absorption peak from a particular subband to subband transition occurs at an energy equal to the bulk band overlap (E_{over}) of the T-point valence band with the L-point conduction band plus the band gap (E_g) of the L-point plus the confinement energy of the L-point subband minus the confinement energy of the T-point subband, see Fig.5-34. In addition, since each subband transition contributes to the absorption spectra at a different energy, the absorption will be more intense at an energy at which many subband to subband transitions occur near the same energy, see Fig. 5-28 (b). This energy is a function of the effective mass components in the confined directions at both the L and T-points and is also a strong function of the non-parabolicity of the bands. The energy of the absorption peak is therefore not a simple function of band parameters and it is possible that the temperature dependencies of the different band parameters counteract each other and result in the energy of the absorption peak being relatively insensitive to temperature.

The second aspect of the weak temperature dependence that is unexpected, is the small change in the *intensity* of the optical absorption as the temperature is decreased. If the absorption mechanism requires a phonon, one would expect that the intensity would decrease with decreasing temperature. Although the intensity does decrease slightly, as seen by the decrease in reflection with decreasing temperature in Fig. 5-14 (a) and (b), the decrease is smaller than expected for a phonon assisted process where the Debye temperature is $\sim 100K$. One explanation for the weak temperature dependence that is observed in the optical absorption is that phonons may not be required for this indirect electronic transition. Instead, a localized defect might be relaxing the momentum requirements. For example, since a surface defect is localized in real space, it is delocalized in momentum space, and therefore if the initial and final states are coupled through a localized surface defect, a phonon might not be required to conserve momentum in this transition. The theory that the indirect

L-T point transition in bismuth nanowires is not phonon assisted is consistent with the fact that the experimental absorption spectra show a single absorption peak as opposed to the simulated spectra, which have a double absorption peak structure; one resulting from phonon absorption, and one resulting from phonon emission. Thus the relaxation of the momentum requirement through a defect mechanism would result in a reduction in the line width of the absorption feature, consistent with the experimental observations.

Momentum Exchange

An issue arose in the course of this research as to how momentum exchange occurs for the L-T point transition under discussion. Early on, it was thought that phonon exchange was required for this electronic transition, since in other materials weak indirect transitions are brought about through phonon exchange. However, the weak temperature dependence of the absorption spectra, the lack of a double peak resulting from the phonon absorption and emission processes, and the intensity of the absorption peak, led us to the conclusion that the momentum exchange occurs as a consequence of modifications of the atomic orbitals near the surface (due to, for example, dangling bonds, surface defects, and discontinuities in the material composition). If the L-point and the T-point valence bands are coupled through a state localized at the surface, the indirect excitation of an electron at the L-point to an empty state at the T-point can be thought of as two direct transitions. The first transition is from the L-point to an intermediate state, which can be either a localized surface defect or a state where the coupling from the initial state was previously not allowed, but because of the lower symmetry at the surface of the wire, the transition can now occur near the wire boundary. The second transition is from this intermediate state to the T-point. Since both transitions are direct, phonon exchange is not required.

Nevertheless, let us consider briefly estimates of how much phonon exchange might be expected. Due to the experience of one of our collaborators, we have some insight as to how the phonon exchange works in this kind of problem. We recognize two primary mechanisms through which phonon exchange can occur. One is recoil due

to the initial photon momentum - such a mechanism is known to be very important at short wavelengths. The other mechanisms is a change in the force constant due to an electron being promoted to a different state. These two mechanisms are nearly independent of one another and we can make progress by analyzing them separately.

Recoil can be analyzed by following the approach used in Mössbauer studies. The Mössbauer fraction, f_{mb}, tells us the fraction of absorbed photons that do not create a phonon, where f_{mb} can be estimated by the equation

$$f_{mb} = exp[-3E_{photon}^2(T/\theta_d)/(M_n c^2 k_B \theta_d)] \tag{5.13}$$

in which E_{photon} is the energy of the photon ($\sim 0.124eV = 1000cm^{-1}$), M_n is the mass of the nucleus ($209 \times 1.6710^{-27}kg$), c is the speed of light, k_B is the Boltzmann constant, and θ_d is the Debye temperature ($\sim 100K$). Using these values, f_{mb} is estimated to be $1 - 8 \times 10^{-11}$. Thus only 8×10^{-11} of the absorbed photons create a phonon. Likewise, the spectral line-width resulting from the Mössbauer effect is related to the recoil energy, R, which is found by the following equation

$$R = \frac{(E_{photon}/c)^2}{2M_n} = 3.910^{-14}eV. \tag{5.14}$$

In other words, for the absorption peaks discussed in this thesis, all cases of phonon exchange due to recoil can be neglected.

The change in force constants is more interesting and we outline a simple argument for the associated magnitude of the vibrational energy. The energy exchange on average would be due to the change in force constants associated with electron excitation. If the electron were localized on a diatomic molecule, the difference in force constants between the initial and final states would lead to a shift in the equilibrium position, which would in turn generate a vibrational energy on the order of an eV or so. In molecular physics this is known as the Duschusky effect, and is taken account through the use of Frank-Condon factors in the molecular calculations. These arguments can be extended to Bi nanowires.

The electron, in this case, is delocalized over N atoms, and hence we expect a

modification of the force constant where the force constant is multiplied by $1/N$. The associated energy exchange per site is smaller by a factor of $1/N^2$. Thus, the total energy exchange, ΔE, should be on the order of

$$\Delta E \rightarrow \Delta E_2 \frac{1}{N^2} N \rightarrow \frac{\Delta E_2}{N} \tag{5.15}$$

where ΔE_2 is the energy exchange in a diatomic molecule.

As relatively high momentum phonons are required for the L-T point transition in bismuth, we would expect the fraction of transitions in which a phonon is exchanged due to the change in the force constants, f_{fc}, to be on the order of

$$f_{fc} \sim \frac{\Delta E}{N\hbar\omega} \tag{5.16}$$

where $\hbar\omega$ is the energy of the photon.

The difference in electronic orbitals at the L and T points is likely to be small, so that the equivalent ΔE_2 is likely to be less than a tenth of an eV. The number of atoms involved would be on the order of those included within a volume of the electron coherence length, about 150^3 atoms. Hence the probability of phonon exchange is on the order of 10^{-8}. Thus, like recoil, phonon exchange due to changes in the force constants between the initial and final states can also be neglected. We, therefore, conclude that an indirect process requiring phonon exchange in bismuth in the mid-IR should be weak.

(This section written in collaboration with Millie Dresselhaus and Peter Hagelstein.)

Enhanced matrix element

One implication of identifying the large optical absorption peak in bismuth nanowires as an indirect interband transition, is the conclusion that such a transition is enhanced because of the large surface area to volume ratio, and that this enhancement is localized at the interface. The dielectric contrast between the bismuth and bismuth-oxide, air, or alumina is proposed as one explanation for this enhancement. Regardless of

the reason for this enhancement, other materials will likely also exhibit an enhanced (indirect) interband transitions when placed into a nanostructure form. More work needs to be done to identify the situations under which an electronic transition is enhanced, what determines the matrix element penetration depth, and for which nanostructured materials an interband transition is enhanced.

Conclusions for the indirect L-T point interband transition

Section 5.3.4 presents a numerical simulation of the optical absorption resulting from an electron excitation between the L and T-point valence bands. Experimentally measured transmission spectra are compared to the simulated transmission spectra. The similarity between these spectra strongly indicate that the measured absorption is dominated by this indirect electronic transition. Furthermore, the polarization dependence, the energy increase with decreasing wire size, the decrease in absorption intensity with increasing n-type doping levels, and the location of the absorption peak of the experimental curve are all consistent with the simulated spectra. The $400\,cm^{-1}$ energy difference between the experimental and simulated peak is not yet understood and needs further investigation. One explanation for the small observed temperature dependence is proposed.

5.4 CONCLUSIONS FOR IDENTIFYING THE ABSORPTION MECHANISMS

The optical absorption of bismuth nanowires in the wavenumber range 650 to $4000cm^{-1}$ is presented from an experimental and theoretical viewpoint. The polarization, wire diameter, doping, and temperature dependence were experimentally determined. In order to identify the absorption mechanism dominant in this energy range, simulations of an indirect interband, direct interband, free-carrier, and intersubband transitions were preformed.

A sharp and intense absorption peak in bismuth nanowires is observed experimen-

tally at $\sim 1000cm^{-1}$ which is not observed in bulk bismuth. Since this absorption peak is present in wires which are too large to be quantum confined, the mechanism is not the result of quantum confinement alone. The strong absorption peak has a unique asymmetric line shape as a function of energy. In addition, this absorption peak is observed to have a strong polarization dependence, whereby it is present when the optical electric field of the incident light is perpendicular to the wire axis but not when the optical electric field is parallel to the wire axis. The energy of the absorption peak increases with decreasing wire diameter. The intensity of the absorption decreases when the amount of n-type dopants is increased. The absorption peak is only weakly dependent on temperature for the temperature range of $\sim 125 - 300K$.

Based on simulations of L-point interband, L-point intersubband, and L-T point indirect band transitions, the absorption peak at $\sim 1000cm^{-1}$ is identified as resulting from an indirect L-point valence band to T-point valence band transition. The unusual shape of the absorption peak, the direction and magnitude of the change in the energy of the absorption peak with a change in wire diameter, and the doping dependencies all agree well with simulations of this indirect transition. The peak in the absorption for this transition is simulated to be at an energy $\sim 400cm^{-1}$ ($\sim 50meV$) larger than the observed peak. This may be a result of somewhat inaccurate values for the band parameters of bismuth nanowires at room temperature.

The polarization dependence as well as the absence of this peak in bulk bismuth are both explained by a coupling coefficient which is only present when the dielectric function of a material varies spatially. This enhancement in the coupling coefficient is not present in bulk materials since the dielectric constant is uniform, but it is present in bismuth nanowires since the dielectric contrasts between bismuth and bismuth-oxide, air, and alumina are all large. Furthermore, this enhancement is only present when the electric field of the incident light crosses a boundary, and therefore it only affects the absorption when the light is perpendicular to the wire axis.

Smaller absorption peaks in the energy range of $600 - 1200cm^{-1}$ are measured in free-standing bismuth nanowires. The energies (wavenumbers ν) of these peaks vary with wire diameter. The energies of these absorption peaks are compared to

the simulated optical absorption peaks resulting from L-point interband, L-point intersubband, and L-T point indirect band transitions. The energies of the smaller absorption peaks agree with the energies of the absorption peaks predicted to result from intersubband electronic transitions at the L-point.

Chapter 6

CONCLUSION AND FUTURE WORK

6.1 CONCLUSION

This thesis measures and analyzes the optical absorption of bismuth nanowires formed inside an anodic alumina template in the energy range of $600-4000$ cm^{-1}. In order to separate the roles of surface and quantum effects in the optical absorption, nanowires were fabricated which have a diameter too large to exhibit quantum effects at room temperature, but small enough to have a large surface area to volume ratio. In order to fabricate nanowires of this diameter, the anodization method was modified and an ultra-cool process of anodization was implemented.

The reflection and transmission of both bismuth nanowires inside an alumina template and those with the template etched away were measured. The absorption spectra of the bismuth nanowires inside an alumina template were deduced by first using the Kramers–Kronig relations, or by solving Maxwell's equations and using the dielectric constant as a fitting parameter, and then by applying an effective medium theory in reverse. The absorption spectra of free-standing wires was found by taking the negative log of the transmission spectra.

The energy, wire diameter, temperature, doping, and polarization dependence of the absorption were experimentally determined. The absorption spectra exhibit a

large asymmetric absorption peak near 1000 cm^{-1}, and several smaller peaks between 600 and 1200 cm^{-1}. The energy (wavenumber) of the large peak decreases relatively slowly with increasing wire diameter. The smaller peaks are also dependent on the wire diameter. The absorption intensity for the $600 - 4000\,cm^{-1}$ wavenumber range decreases with increasing n-type dopant and is observed for incident light with its electric field perpendicular to the wire axis, but not for light with its electric field parallel to the wire axis. The absorption changes little with temperature.

The optical absorption spectra of bismuth nanowires resulting from interband, intersubband, and indirect interband transitions are simulated. The results are compared with the experiments. The energy of the smaller intensity peaks agree with the predicted energies of those resulting from intersubband transitions. The sharper, larger intensity peak is identified as resulting from an indirect T-point valence band to L-point valence band transition. The shape of the absorption peak as well as the wire diameter and doping dependencies agree well with the simulated results. The simulated absorption from an indirect transition predicts an absorption peak at an energy larger than that measured. One explanation for this difference is the use of somewhat inaccurate values in the model for the band parameters of bismuth at room temperature, since the room temperature band parameters for bulk bismuth are not accurately known at the present time. The presence of the strong absorption peak in non-quantum confined bismuth nanowires, as well as the polarization dependence of this absorption peak in the nanowires, are explained by a surface component to the coupling strength which is present when the dielectric function varies spatially, such as occurs in bismuth nanowires.

6.2 FUTURE WORK

There are many different directions that this work can branch towards. Here are some of the directions that I feel are interesting and could lead to important results.

6.2.1 SECONDARY ION MASS SPECTROMETRY (SIMS)

In all the doping studies completed so far, the doping concentration and distribution are unknown. For the antimony and the tellurium-doped experiments, a predetermined percentage of dopants is incorporated into the molten bismuth during the fabrication of the nanowires. However, since we do not know if crystallization of the bismuth nanowires begins at the aluminum or the bulk bismuth side of the template and we don't know the segregation coefficient of antimony and tellurium inside a bismuth host, the percent of impurities inside the nanowires as a function of distance along the wire axis cannot be calculated. Therefore, the stoichiometry must be determined experimentally. Furthermore, the effect of the surrounding alumina on the diffusion process is as yet undetermined. The moving crystalline/liquid boundary during the cooling process can push out dopants into the liquid increasing the concentration in the melt, or it can absorb dopants from the liquid depleting the concentration of dopants in the melt. This has an effect of increasing or decreasing the doping concentration along the wire axis. In addition, the alumina template may cause a changing dopant distribution radially inside each wire.

Huber [88] reports that the melting temperature of bismuth inside the pores of alumina is slightly lower than the melting temperature of bulk bismuth. This decrease in melting temperature for nanocrystals is also predicted theoretically [89]. Therefore as the bismuth/bismuth nanowire system cools at the end of the liquid pressure injection process (see section 3.3), the bulk bismuth solidifies before the bismuth nanowires. Huber et. al. therefore conclude that since bismuth prefers to have Sb dopants, the doping concentration in the melt decreases as the bismuth solidifies. Hence, since the nanowires crystallize last, they have a lower Sb doping concentration than in bulk material. In addition, EDX measurements of our wires clearly show that the Sb dopants concentrate around the copper wire, which is used to secure the alumina template during the filling process, probably because this area cools first. Only low levels of Sb doping were detected on the surface of the nanowires. However, preliminary SIMS measurements for the antimony distribution of antimony-doped

bismuth wires, performed with Prof. Shimizu from the Wood's Hole Oceanographic Institute, showed a steady SIMS profile of the antimony doping throughout a length of $30\mu m$, along the length of the wire.

The concentration profile of Te in Te-doped bismuth nanowires also seems to vary along the wire axis. EDX measurements of Te-doped nanowires show that the side of the sample nearest the bulk bismuth has more doping than the side nearest the aluminum. Furthermore, preliminary SIMS measurements showed that tellurium dopants are only present on the bismuth side of the sample and not on the aluminum side. This agrees with the experimental FTIR data where the reflectivity on the aluminum side looks like that for the undoped samples, while the reflectivity of the bismuth side depends on the doping.

For all these reasons, it is necessary to quantify the doping profile inside the nanowires. The only method I know of that might be able to measure doping profiles along the wire axis is SIMS. Unfortunately, SIMS measurements of bismuth proved to be much more time consuming and expensive than I had originally expected. Since SIMS of bismuth is uncommon, the SIMS sensitivity of bismuth, tellurium, and antimony has to be calibrated. In order to do this, SIMS of bulk bismuth with varying levels of doping need to be measured. This is both a time consuming and expensive endeavor, but is critical to qualitatively determining the doping levels in bismuth nanowires. All of my SIMS measurements are very preliminary and need to be reproduced.

6.2.2 FURTHER DOPING STUDIES

So far we have made only a handful of doped samples for each doping type at a handful of wire sizes. For each doping and wire diameter combination, a new sample must be fabricated, and currently this fabrication takes about two weeks per sample. I see several ways to overcome this time limitation. Firstly, soon we will be able to electro-chemically deposit bismuth into the alumina templates in our own lab. This will allow any group member, that wishes, to make bismuth nanowires (right now, only one student from our group can be qualified to fill alumina templates with

bismuth at a time), thus allowing more samples with different diameters and doping levels to be fabricated.

Another possible way to get more doping levels is to electro-chemically dope the bismuth nanowires while measuring their optical properties. Similar to the measurements on nanotubes, [90] nanowires can be measured inside the solution as the Fermi energy is modified by an external voltage. This technique would allow for measurements of nanowires with a continuously varying Fermi energy. I would expect that as the Fermi energy is raised above the T-point valence band, the absorption peak at ~ 1000 cm^{-1} would be quenched because of the decreased availability of empty final states.

Although very powerful, this measurement will be difficult with our experimental setup. Since the nanowire arrays are small, a microscope stage must be used. Therefore, an electro-chemical cell that fits in the working area of the microscope has to be hand made. In addition, since the cell will be close to the optics of the microscope, an inert solution has be used. If an inert solution which allows for electro-chemical doping doesn't exist, a KBr window can be placed over the cell to protect the optics. However, obtaining a measurable signal by focusing through the window and through the solution will be difficult. Lastly, this method will only work for samples with a significant band gap relative to k_BT so that few free carriers remain in the sample, and hence there is significant band bending at the nanowire surface. This means, for bismuth nanowires, small wire diameters and low temperatures are required. However, the working area in the cold stage is only a few millimeters. I don't expect that this measurement would be feasible for bismuth nanowires, but it may prove more appropriate for larger bandgap semiconductor nanowires.

6.2.3 BISMUTH-ANTIMONY NANOWIRES

The T-point valence band in bismuth-antimony alloys is at a lower energy than in pure bismuth. In bulk bismuth, as the percentage of antimony is increased from 0 to 10%, the T-point moves from -18.5 to 14meV relative to L-point conduction band edge [91]. In other words, the alloy transitions from a semi-metal with a band overlap

of 18.5meV to a semi-conductor with an indirect band gap of 14meV as the percentage of antimony is increased from 0% (pure bismuth) to 10%.

In bismuth nanowires, when the T-point valence band is lower than the Fermi energy, the indirect L-point to T-point valence band transition will be quenched (as observed in the tellurium-doped samples). Therefore, optical measurements of the absorption intensity of the $\sim$ 1000 cm^{-1} absorption peak can serve as a measure of the amount of antimony inside the bismuth nanowires.

Opposite to electrical measurements, optical measurements of bismuth-antimony wires are dominated by the section of the sample that has the lowest concentration of antimony, since the higher the antimony concentration, the lower the optical absorption. Incident light will be absorbed if it passes through a section of the nanowire array where the Fermi energy is below the T-point valence band (low concentrations of antimony). Therefore, if a nanowire has a non-uniform concentration of antimony, the minimum concentration along the wire axis will dominate in the optical absorption spectra. Likewise, if uniformly doped antimony nanowires are separated by less than the optical wavelength ($\sim 10\mu m$), and these wires have different concentrations of antimony, then the nanowires with the lowest concentration of antimony will be measured. Preliminary measurements of bismuth-antimony nanowires were measured, but the expected decrease in absorption intensity was not observed. More work needs to be done to understand the doping distribution inside the nanowire array and in optically characterizing bismuth-antimony nanowires.

6.2.4 PHOTOLUMINESCENCE

Photoluminescence (PL) is a powerful tool to measure electronic properties such as the bandgap. Ideally, the excitation laser in a PL setup should be a high power laser with an energy slightly larger than the band gap of the material being measured. For bismuth, a CO_2 laser is probably the best choice. I expect the luminescence of bismuth nanowires to be in the far IR, so a far IR detector is needed. Previously, with the help of Jurgen Mitchel in Prof. Kimerling's lab, we measured PL of bismuth nanowires using a high power, but visible (too high energy for bismuth) laser at low

temperatures. I was only able to measure the luminescence in the visible, and I did not observe luminescence in this energy range as it is not the appropriate energy range for bandgap luminescence in bismuth. In addition, I tried to measure luminescence in the far IR at room temperatures with a He-Ne laser (lower energy but also lower power). In this experiment, the bismuth nanowires again did not luminescence.

The ability to measure PL in the far IR would open up the possibilities of many new experiments. I would expect a very large non-linear optical absorption from bleaching near 1000 cm^{-1}. This can be measured by measuring the PL vs. the intensity of the excitation source. Furthermore, there are other non-linear effects that could be investigated with a good PL setup. For example, I would expect that light with an energy of the L-point band gap ($\sim$ 650 cm^{-1}) could control the absorption intensity from the L-T point transitions ($\sim$ 1000 cm^{-1}).

6.2.5 ONE-DIMENSIONAL DIODE

By diffusing tin (p-type dopant) into a tellurium-doped bismuth nanowire array (n-type), a p-n junction can be made. A p-n junction in bismuth nanowires would be interesting for several reasons. First, I did some initial calculations that showed that at 2-4K, the I-V curves might have interesting features (wiggles) that result from quantum confinement. This has to do with the Fermi energy not moving smoothly as the doping is increased. If these wiggles are observed, they can be used as another measurement of the band parameters of Bi nanowires. In addition to I-V measurements, these p-n junctions will, likely, show cathodo-luminescence (CL). CL measurements could be performed on our FTIR setup. Since bismuth nanowires have singularities in their density of states, if the coupling is allowed, these one-dimensional diodes should make excellent light emitting diodes.

I attempted to make a p-n junction in bismuth nanowires. However, without the ability to measure doping profiles, and since the diffusion rate of tin in bismuth nanowires is not known, making a junction is extremely difficult. I recommend developing SIMS measurements of bismuth nanowires before pursuing the fabrication of a p-n junction.

Appendix A

EMT LITERATURE REVIEW

When a sample consists of more than one material and is non-homogeneous, the optical properties are modified in a non-trivial manner. For example, nanoparticles of metals are no longer shiny but take on a black appearance. Normally, the free electrons in a metal move in response to the electric field of the light causing the light to be reflected, but in a nanoparticle the electrons can no longer move unobstructed, and so the reflection decreases and the sample looks black. Photonic band gap materials are another example of how a heterogeneous material has an optical response significantly different from either of the two materials inside it.

One approach to approximate the optical response of a heterogeneous material in terms of its microstructure is by using an effective medium theory (EMT). EMTs relate the dielectric function of a composite material with the dielectric function of the constituents materials, where the complex dielectric function, $\epsilon_1 + i\epsilon_2$, is that used in Maxwell's equations and is defined as

$$D = \epsilon E = E + 4\pi P. \tag{A.1}$$

Many different versions of effective medium theories have been developed each of which are applicable for different types of samples.

In two situations, the dielectric function of a composite material can be easily solved for. If all the internal boundaries are parallel to the applied electric field, the

situation is analogous to capacitors in parallel, and the effective dielectric function is related to the dielectric function of the composites by the following equation:

$$\epsilon_{composite} = \sum_j f_j \epsilon_j \tag{A.2}$$

where ϵ_j and f_j are the complex dielectric function and volume fraction of each constituent material, j.

In the opposite limit, all the boundaries are perpendicular to the applied electric field, and this situation is analogous to capacitors in series. In this case the composite's dielectric function is the following:

$$\epsilon^{-1}_{composite} = \sum_j f_j \epsilon_j^{-1}. \tag{A.3}$$

These two cases define the Weiner absolute bounds to ϵ. The dielectric function of all composite materials lie on or within the region defined in the complex plane of ϵ by Eqs. A.2 and A.3.

Although the dielectric function can be solved for exactly in these two cases, in most cases, a composite material has many boundaries in many different directions, and so the dielectric function can not be solved for exactly. For these samples an effective medium approximation is useful.

Most EMTs are based on the Clausius-Mossotti equation for a sample made up of two materials.

$$\frac{\epsilon_{\text{composite}} - \epsilon_{\text{host}}}{\epsilon_{\text{composite}} + K\epsilon_{\text{host}}} = f_{\text{a}} \frac{\epsilon_{\text{a}} - \epsilon_{\text{host}}}{\epsilon_{\text{a}} + K\epsilon_{\text{host}}} + f_{\text{b}} \frac{\epsilon_{\text{b}} - \epsilon_{\text{host}}}{\epsilon_{\text{b}} + K\epsilon_{\text{host}}}. \tag{A.4}$$

In this equation ϵ_{a}, ϵ_{b}, and $\epsilon_{\text{composite}}$ are the complex dielectric functions of material a, material b, and the composite material. ϵ_{host} is the dielectric function that is experienced by the particles at the microscopic level. K is the screening parameter of the particles and depends on the particle shape by the relation

$$K = \frac{1-q}{q} \tag{A.5}$$

where q is the Lorentz depolarization factor. q can be calculated for a single particle based on the asymmetry of the shape of the particle. If this particle is an ellipsoid with axes of revolution, a parallel and b perpendicular to the direction of light, q can be solved for by the relation.

$$q = \frac{1/b}{1/a + 2/b}. \tag{A.6}$$

Using Eq. A.5 and Eq. A.6, the limiting case of light propagating along a wire axis, a becomes very large, and so q approaches $1/2$ and K approaches 1.

The Clausius-Mossotti equation is formally valid only for static electric fields. However, when the particle dimensions are much smaller than the wavelength of light, scattering effects can be ignored and the Clausius-Mossotti relation is then valid. This approximation is referred to as the "quasi-static limit".

The two most widely used EMTs are the Maxwell-Garnett (MG-EMT) and the Bruggeman (B-EMT). These two theories differ only in how ϵ_{host} is defined in the Clausius-Mossotti relation. In the MG-EMT, material b is assumed to be surrounded by material a, and hence ϵ_{host} is equal to ϵ_{a}. Equation A.4 then reduces to Eq. 4.5 or equivalently:

$$\frac{\epsilon_{\text{composite}} - \epsilon_{\text{a}}}{\epsilon_{\text{composite}} + K\epsilon_{\text{a}}} = f_{\text{b}} \frac{\epsilon_{\text{b}} - \epsilon_{\text{a}}}{\epsilon_{\text{b}} + K\epsilon_{\text{a}}}. \tag{A.7}$$

The B-EMT assumes that the composite contains a random mixture of material a and material b and so $\epsilon_{\text{host}} = \epsilon_{\text{composite}}$. Eq. A.4 then reduces to

$$0 = f_{\text{a}} \frac{\epsilon_{\text{a}} - \epsilon_{\text{host}}}{\epsilon_{\text{a}} + K\epsilon_{\text{host}}} + f_{\text{b}} \frac{\epsilon_{\text{b}} - \epsilon_{\text{host}}}{\epsilon_{\text{b}} + K\epsilon_{\text{host}}}. \tag{A.8}$$

MG-EMT can also be derived easily from first principles by defining an average electric field in the sample, E_{av}, and an average displacement field, D_{av}:

$$E_{av} = f_a E_a + f_b E_b \tag{A.9}$$

$$D_{av} = f_a \epsilon_a E_a + f_b \epsilon_2 E_b. \tag{A.10}$$

By applying Eq. A.1, we obtain

$$\epsilon_{eff} = D_{av}/(\epsilon_0 E_{av}) \tag{A.11}$$

In the case that $f_a << f_b$, then E_b is only slightly disturbed, and E_a can be described by Laplace's equation:

$$E_a = \frac{\epsilon_2}{\epsilon_2 + K(\epsilon_1 - \epsilon_2)} E_b \tag{A.12}$$

Substituting Eq. A.12 into Eq. A.11 and Eq. A.10, the MG-EMT is obtained. Similarly, the B-EMT can be derived by assuming that each particle only sees an infinite medium with a uniform dielectric function, ϵ_{eff}. In this case Laplace's equations for the electric field can be written as

$$E_a = \frac{\epsilon_{eff}}{\epsilon_{eff} + K(\epsilon_a - \epsilon_{eff})} E_{av} \tag{A.13}$$

and

$$E_b = \frac{\epsilon_{eff}}{\epsilon_{eff} + K(\epsilon_b - \epsilon_{eff})} E_{av}. \tag{A.14}$$

Substituting these values for E_a and E_b into Eq. A.9 leads to the B-EMT, Eq. A.8.

MG-EMT is accurate for materials where particles of material b do not touch each other and the particles are small, while B-EMT is accurate for when the concentrations of the two materials are similar and so each material forms semi-connected regions inside the composite. In the case of bismuth nanowires inside alumina, the approximation used to derive the MG-EMT is more accurate. Cherkas solved for the dielectric function of a material with cylindrical pores, such as in anodic alumina, and obtained an equation that is equivalent to that of MG-EMT for the limit of $K = 1$ [28].

Another EMT is the Mie EMT. The Mie EMT is a more complicated, but is a more

rigorous approximation. It is useful for composites where the inter-particle distance is much larger than the wavelength of the incident light, or the particles are too large for MG-EMT or B-EMT. Unlike B-EMT and MG-EMT, Mie EMT does not assume any particular the size for the particles inside the host, but it does assume that the particles are spherical. Opposite to B-EMT and MG-EMT, Mie EMT assumes that the particles are separated by large distances (relative to the wavelength of light). Other EMTs include Newton, Beer, Lorenz-Lorentz, Ganx-Happel, and Wiener. In addition, many modifications exist to the more common effective medium theories. For example, MG-EMT has been modified for wire arrays to include eddy currents induced by magnetic fields [92]. In addition, MG-EMT has been modified for porous materials and then applied to porous silicon carbide [27].

Several studies have investigated the use of EMTs in predicting the dielectric function of anodic alumina. For example, Wackelgard applies MG-EMT to anodic alumina in the mid-IR and finds that the predicted frequency dependent dielectric function and measured dielectric function agree well [93]. In another study, Foss, Tierney, and Martin [94] compare the dielectric function of gold inside anodic alumina with that predicted by MG-EMT and B-EMT. They find qualitative agreement between MG-EMT and the measured dielectric function. However, the transmission of the measured spectra decreases faster with increasing energy than the predicted spectra. This additional decrease could be the result of surface scattering. The dielectric function predicted by B-EMT had similar inconsistencies with the measured data. The authors explain that both the MG-EMT and B-EMT assume that the particles are close together. However, if the particles are not close together, a time lag exists between the incident and induced fields. This results in a retarded potential. When this retarded potential is taken into account, the predicted dielectric function is consistent with the measured dielectric function [94]. Their resulting modified EMT is in between the Mie EMT and the MG-EMT and uses an effective screening parameter that takes into account the size and the shape of the particles [72].

In addition, effective medium theories can be used in reverse to obtain the dielectric function of one of the constituents, if the dielectric function of the composite

and that of the other constituent is known. Reverse effective medium theory is applied to find the dielectric function of anodic alumina by both our group [95] and the Martin [58] group. In addition, the work presented in this thesis uses reverse effective medium theory to deduce the dielectric function of bismuth nanowires inside an anodic alumina template.

Note: It is important to note that the dielectric function ϵ described in this appendix is different from the unitless (dimensionless) ϵ used in the rest of the thesis. For the rest of the thesis, ϵ is just the full ϵ divided by ϵ_0.

Bibliography

[1] M. P. Vecchi and M. S. Dresselhaus, Phys. Rev. B **10**, 771 (1974).

[2] C. F. Gallo, B. S. Chandrasekhar, and P. H. Sutter, J. Appl. Phys. **34**, 144–152 (1963).

[3] J. P. Sullivan and G. C. Wood, Proc. Roy Soc. Lond. A. **317**, 511–543 (1970).

[4] M. R. Black, K. R. Masklay, O. Rabin, Y.-M. Lin, S. B. Cronin, M. Padi, Y. Fink, and M. S. Dresselhaus. In *Nanophase and Nanocomposite Materials IV: MRS Symposium Proceedings, Boston, December 2001*, edited by S. Komarneni, R. A. Vaia, G. Q. Lu, J.-I. Matsushita, and J. C. Parker, page AA8.9, Materials Research Society Press, Pittsburgh, PA, 2002.

[5] N. Kouklin, S. Bandyopadhyay, S. Tereshin, A. Varfolomeev, and D. Zaretsky, Applied Physics Letters **76**, 460–519 (2000).

[6] D. E. Aspnes, A. Heller, and J. D. Porter, J. Appl. Phys. **60**, 3028–3034 (1986).

[7] M. S. Dresselhaus, T. Koga, X. Sun, S. B. Cronin, K. L. Wang, and G. Chen. In *Sixteenth International Conference on Thermoelectrics: Proceedings, ICT'97; Dresden, Germany*, edited by Armin Heinrich and Joachim Schumann, pages 12–20, Institute of Electrical and Electronics Engineers, Inc., Piscataway, NJ 09955-1331, 1997. IEEE Catalog Number 97TH8291; ISSN 1094-2734; pdf.

[8] L. D. Hicks and M. S. Dresselhaus, Phys. Rev. B **47**, 12727–12731 (1993).

[9] O. Madelung, in *Landolt-Börnstein Numerical Data and Functional Relationships in Science and Technology, New Series*, pages 43–87, edited by K.-H. Hellwege (Springer-Verlag, Berlin, 1982), Vol. 17a.

[10] Zhibo B. Zhang. *Fabrication, characterization and transport properties of bismuth nanowire systems.* Ph. D. thesis, Massachusetts Institute of Technology, Department of Physics, February 1999.

[11] Yu-Ming Lin. Doping Bi nanowires. Master's thesis, Massachusetts Institute of Technology, January 2000. Department of Electrical Engineering and Computer Science.

[12] R. T. Isaacson and G. A. Williams, Phys. Rev. **185**, 682 (1969).

[13] V. Damodara Das and N. Soundararajan, Phys. Rev. B **35**, 5990–5996 (1987).

[14] Y.-M. Lin, X. Sun, and M. S. Dresselhaus, Phys. Rev. B **62**, 4610–4623 (2000).

[15] B. Lax and J. G. Mavroides, in *Advances in Solid State Physics*, (Academic Press, New York, 1960), Vol. 11.

[16] M. S. Dresselhaus. In *Proceedings of the Conference on the Physics of Semimetals and Narrow Gap Semiconductors*, edited by D. L. Carter and R. T. Bate, pages 3–33, Pergamon Press, New York, NY, 1970.

[17] M. H. Cohen, Phys. Rev. **121**, 387 (1961).

[18] M.S. Dresselhaus and G. Dresselhaus, *Applications of Group Theory to the Physics of Solids* (Academic Press, New York, NY, 2002). Class notes in preparation for publication.

[19] J. Heremans. PhD thesis, University of Louvain, December 1978. Department of Physics.

[20] R. D. Brown, R. L. Hartman, and S. H. Koenig, Phys. Rev. **172**, 598 (1968).

[21] G. E. Smith, G. A. Baraff, and J. M. Rowell, Phys. Rev. A **135**, 1118 (1964).

[22] P. N. Sen, C. Scala, and M. H. Cohen, Geophysics **46**, 781–795 (1981).

[23] U. Kreibig, A. Althoff, and H. Pressmann, Surface Science **106**, 308–317 (1991).

[24] Veronica M. Cepak and C. R. Martin, J. Phys. Chem. B. **102**, 9985–1966 (1998).

[25] J. C. Maxwell Garnett, Phil. Trans. A. **203**, 385–420 (1904).

[26] J. C. Maxwell Garnett, Phil. Trans. A. **205**, 237–288 (1906).

[27] Jonathan E. Spanier and Irving P. Herman, Phys. Rev. B **61**, 437–450 (2000).

[28] N. L. Cherkas, Opt. Spectrosc. **81**, 906–912 (1996).

[29] Feiyue Li, Robert M. Metzger, and W. D. Doyle, IEEE Trans. on Magn. **33**, 3715–3717 (1997).

[30] K. Nielsch, R. B. Wehrspohn, J. Barthel, J. Kirschner, and U. Gosele, Appl. Phys. Let. **79**, 1360–1362 (2001).

[31] G. Dresselhaus, M. S. Dresselhaus, Z. Zhang, X. Sun, J. Ying, and G. Chen. In *Seventeenth International Conference on Thermoelectrics: Proceedings, ICT'98; Nagoya, Japan*, edited by K. Koumoto, pages 43–46, Institute of Electrical and Electronics Engineers, Inc., Piscataway, NJ 09955-1331, 1998.

[32] Raman Venkatasubramanian, Edward Silvoia, Thomas Colpitts, and Broks O Quinn, Nature **413**, 597–602 (2001). 11.

[33] T. C. Harman, P. J. Taylor, M. P. Walsh, and B. E. LaForge, Science Magazine **297**, 2229–2232 (2002).

[34] V. Dneprovskii, E. Zhukov, V. Karavanskii, V. Poborchii, and I. Salamatini, Superlattices and Microstructures **23**(6), 1217–1221 (1998).

[35] M. H. Huang, S. Mao, H. Feick, H. Yan, Y. Wu, H. Kind, E. Weber, R. Russo, and P. Yang, Science **292**, 1897–1899 (2001).

[36] Justin C. Johnson, Haoquan Yan, Richard D. Schaller, Poul B. Petersen, Peidong Yang, and Richard J. Saykally, Nano Letters **2**, 279–283 (2002).

[37] H. Kind, H. Yan, B. Messer, M. Law, and P. Yang, Adv. Mat. **14**, 158–160 (2002).

[38] B. M. I. van der Zande, M. Bohmer, L. G. J. Fokkink, and C. Schoneberger, Langmuir **16**, 451–458 (2000).

[39] B. M. I. van der Zande, G. J. M. Koper, and H. N. W. Lekkerkerker, J. Phys. Chem. B **103**, 5754–5760 (1999).

[40] S. Nicewarner-Pena, R. Griffith Freeman, B. Reis, L. He, D. Pena, I. Walton, R. Cromer, C. Keating, and M. Natan, Science **294**, 137–141 (2001).

[41] W. Huynh, J. Dittmer, and A. P. Alivisatos, Science **295**, 2425–2427 (2002).

[42] Z. Zhang, J. Y. Ying, and M. S. Dresselhaus, J. Mater. Res. **13**, 1745–1748 (1998).

[43] Z. Zhang, X. Sun, M. S. Dresselhaus, J. Y. Ying, and J. Heremans, Appl. Phys. Lett. **73**, 1589–1591 (1998).

[44] T. E. Huber, M. J. Graf, and C. A. Foss. In *Thermoelectric Materials–The Next Generation Materials for Small-Scale Refrigeration and Power Generation Applications: MRS Symposium Proceedings, Boston, volume* **545**, edited by T. M. Tritt, H. B. Lyon, Jr., G. Mahan, and M. G. Kanatzidis, pages 227–231, Materials Research Society Press, Pittsburgh, PA, 1999.

[45] T. E. Huber, M. J. Graf, C. A. Foss Jr., and P. Constant, J. Mater Res. **15**, 1816–1821 (2000).

[46] J. W. Diggle, T. C. Downie, and C. W. Goulding, Chem. Rev. **69**, 365–405 (1969).

[47] O. Jessensky, F. Müller, and U. Gösele, Appl. Phys. Lett. **72**(10), 1173 (1998).

[48] Feiyue Li, Lan Zhang, and Robert M. Metzger, Chem. Mater. **10**, 2470–2480 (1998).

[49] A. P. Li, F. Muller, A. Birner, K. Nielsch, and U. Gosele, Journal of Applied Physics **84**, 6023–6026 (1998).

[50] H. Masuda and M. Satoh, Science **268**, 1466 (1995).

[51] A. Jagminas, D. Bigelience, I. Mikulskas, and R. Tomasiunas, Journal of Crystal Growth **223**, 591–598 (2001).

[52] K. Nielsch, J. Choi, K. Schwirn, R. Wehrspohn, and U. Gosele, Nanoletters **2**, 677–680 (2002).

[53] Hideki Masuda and Kenji Fukuda, Science **268**, 1466–1468 (1995).

[54] Y. Li, E. R. Holland, and P. R. Wilshaw, J. Vac. Sci. Technol. B. **18**, 994–996 (2000).

[55] D. Routkevitch, A. A. Tager, J. Haruyama, D. Almawlawi, M. Moskovits, and J. M. Xu, IEEE Trans. on Electron Devices **43**(10), 1646–1658 (1996).

[56] D. Routkevitch, T. Bigioni, M. Moskovits, and J. M. Xu, J. Phys. Chem. **100**, 14037 (1996).

[57] C. A. Foss, G. L. Hornyak Jr., J. A. Stockert, and C. R. Martin, J. Phys. Chem. **96**, 7497–7499 (1992).

[58] G. L. Hornyak, C. J. Patrissi, and C. R. Martin, J. Phys. Chem. B. **101**, 1548–1555 (1997).

[59] Wang Wei, Guo Hetong, and Zhange Jianzhong, ().

[60] J. Heremans, C. M. Thrush, Y. Lin, S. Cronin, Z. Zhang, M. S. Dresselhaus, and J. F. Mansfield, Phys. Rev. B **61**, 2921–2930 (2000).

[61] M. S. Dresselhaus, Y.-M. Lin, O. Rabin, M. R. Black, and G. Dresselhaus, in *Nanotechnology Handbook*, page xxx, edited by Bharat Bhushan (Springer-Verlag, Heidelberg, Germany, 2004). Nanowires.

[62] Stephen B. Cronin. *Electronic Properties of Bi Nanowires.* Ph. D. thesis, Massachusetts Institute of Technology, Department of Physics, June 2002.

[63] L. Leontie, M. Caraman, M. Alexe, and C. Harnagea, Surface Science pages 480–485 (2002).

[64] Z. Zhang, D. Gekhtman, M. S. Dresselhaus, and J. Y. Ying, Chem. Mater. **11**, 1659–1665 (1999).

[65] Y.-M. Lin, S. B. Cronin, J. Y. Ying, M. S. Dresselhaus, and J. P. Heremans, Appl. Phys. Lett. **76**, 3944–3946 (2000).

[66] D. L. Demske, J. L. Price, N. A. Guardala, N. Lindsey, J. H. Barkyoumb, J. Sharma, H. H. Kang, and L. Salamanca-Riba. In *Thermoelectric Materials–The Next Generation Materials for Small-Scale Refrigeration and Power Generation Applications: MRS Symposium Proceedings, Boston, volume* **545**, edited by T. M. Tritt, H. B. Lyon, Jr., G. Mahan, and M. G. Kanatzidis, page 209, Materials Research Society Press, Pittsburgh, PA, 1999.

[67] Y. Peng, D-H Qin, R-J Zhou, and H-L Li, Materials Science and Engineering B] **B77**, 246–249 (2000).

[68] S. B. Cronin, Y.-M. Lin, O. Rabin, M. R. Black, G. Dresselhaus, M. S. Dresselhaus, and P. L. Gai, Microscopy and Microanalysis **8**, 58–63 (2002).

[69] S. B. Cronin, Y.-M. Lin, O. Rabin, M. R. Black, J. Y. Ying, M. S. Dresselhaus, P. L. Gai, J.-P. Minet, and J.-P. Issi, Nanotechnology Journal **13**, 653–658 (2002).

[70] M. R. Black, M. Padi, S. B. Cronin, Y.-M. Lin, O. Rabin, T. McClure, G. Dresselhaus, P. L. Hagelstein, and M. S. Dresselhaus, Appl. Phys. Lett. **77**, 4142–4144 (2000).

[71] D. E. Aspnes, Thin Solid Films **89**, 249–262 (1982).

[72] C. A. Foss, Jr. G. L. Hornyak, J. A. Stockert, and C. R. Martin, J. Phys. Chem. B. **98**, 2963–2971 (1994).

[73] A. Anderson, O. Hunderi, and C. G. Granqvist, J. Appl. Phys. **51**, 754–764 (1980).

[74] V. V. Poborchii, Jpn. J. Appl. Phys. **34**, 271–274 (1995).

[75] U. Kreibig and L. Genzel, Surface Science **156**, 678–700 (1985).

[76] S. Link, M. B. Mohamed, and M.A. El-Sayed, J. Phys. Chem. B. **103**, 3073–3077 (1999).

[77] C. G. Granqvist and O. Hunderi, Phys. Rev. B. **18**, 2897–2906 (1978).

[78] S. B. Cronin, Y.-M. Lin, P. L. Gai, O. Rabin, M. R. Black, G. Dresselhaus, and M. S. Dresselhaus. In *Anisotropic Nanoparticles: Synthesis, Characterization and Applications: MRS Symposium Proceedings, Boston, December 2000*, edited by S. Stranick, P. C. Searson, L. A. Lyon, and C. Keating, pages C571–C576, Materials Research Society Press, Pittsburgh, PA, 2001.

[79] H. R. Verdun and H. D. Drew, Phys. Rev. Lett. **33**, 1608 (1974).

[80] V.D. Kulakovskii and V. D. Egorov, Physics and Technics of Semiconductors:Fizica tverd. Tela **15**, 2053–2059 (1972).

[81] B. Lax, J. G. Mavroides, H. J. Zeiger, and R. J. Keyes, Phys. Rev. Lett. **5**, 241 (1960).

[82] M. Zaluzny, Phys. Rev. B **43**, 4511–4514 (1991).

[83] M. R. Black, Y.-M. Lin, S. B. Cronin, O. Rabin, and M. S. Dresselhaus, Phys. Rev. B **65**, 195417(1–9) (2002).

[84] M. R. Black, Y. M. Lin, S. B. Cronin, O. Rabin, and M. S. Dresselhaus, unpublished (2002).

[85] T. Miller, E. D. Hansen, W. E. McMahon, and T. C. Chiang, Surface Science **376**, 32–42 (1997).

[86] B. Feuerbacher, B. Fitton, and R. F. Willis, in *Photoemission and the Electronic Properties of Surfaces*, (John Wiley and Sons, 1978).

[87] P. Enders and R. Schuchardt, Phys. Stat. Sol. B. **135**, 207–216 (1986).

[88] T. E. Huber, O. Onakoya, and M. H. Ervin, J. of Applied Physics **92**, 1337–1343 (2002).

[89] Kesav N. Shrivastava, Nano Letters **2**, 519–523 (2002).

[90] P. Corio, P. S. Santos, V. W. Brar, Ge. G. Samsonidze, S. G. Chou, and M. S. Dresselhaus, Chem. Phys. Lett. **370**, 675–682 (2003).

[91] A. L. Jain, Physical Review **114**, 1518–1528 (1959).

[92] T. E. Huber, F. Boccuzzi, and L. Silber, Phys. Rev. B **59**, 7446–7450 (1999).

[93] Ewa Wackelgard, J. Phys.: Condens. Matter **8**, 4289–4299 (1998).

[94] C. A. Foss, M. J. Tierney, and C. R. Martin, J. Phys. Chem. **96**, 9001–9007 (1992).

[95] M. R. Black, Y.-M. Lin, M. S. Dresselhaus, M. Tachibama, S. Fang, O. Rabin, F. Ragot, P. C. Eklund, and Bruce Dunn. In *Nanophase and Nanocomposite Materials III: MRS Symposium Proceedings, Boston, December 1999*, edited by S. Komareni, J. C. Parker, and H. Hahn, pages 623–628, Materials Research Society Press, Pittsburgh, PA, 2000.